Comparison of relative biological effectiveness in passive scattering- and pencil beam scanning proton therapy of pediatric cancer

Lars Sandnes

Supervisors:

Ph.D. Kristian Smeland Ytre-Hauge

Ph.D. Camilla Hanquist Stokkevåg

Ph.D. candidate Lars Fredrik Fjæra

Master thesis in medical physics and technology

Department of Physics and Technology

University of Bergen

June 2020

Acknowledgements

First of all, I would like to thank my supervisors, Ph.D. Kristian Smeland Ytre-Hauge, Ph.D. Camilla Hanquist Stokkevåg and Ph.D. candidate Lars Fredrik Fjæra, for all their great guidance. It showed me an exciting new world and I have enjoyed the work immensely.

Thank you, Camilla, for the impassioned lecture which made me want to study medical physics, and for suggesting this project to me.

Thank you, Kristian, for providing me with a deeply interesting project and a very helpful Monte Carlo curriculum (and for lending me your copy of «Proton Therapy Physics» for the better part of a year).

Thank you, Lars Fredrik, for all of the incredibly helpful and engaging conversations in your office (and for accepting that «literally a couple of minutes to spare» was generally spoken in a highly figurative manner).

Thank you to all my friends, both within and without the university. These have been five truly great years.

Thank you, Heine Olsson Aabø, for making exam reading in a poorly ventilated library a genuine high point of my studies.

Thank you, Henrik Drægni Stolpnes and Mathias Wilhelmsen, for your friendship, and for helping me pick up the pieces whenever my mind breaks. I could not have done this without you.

Lastly and crucially, I would like to thank my parents, Brit Sandnes and Roar Tiller, for their constant love and support, even after 25 years of me not picking up the phone first.

Bergen, June 2020
Lars Sandnes

Abstract

Background and purpose

In proton radiation therapy, the vast majority of patients have been treated using the passive scattering (PS) beam delivery technique. Increasingly, new proton therapy centers apply the pencil beam scanning (PBS) delivery technique instead of PS. PBS is generally considered to provide an increased sparing of surrounding healthy tissue and organs at risk (OARs). While a lot of clinical data is available for the PS modality, the original treatment plans does not take the linear energy transfer (LET) into account when calculating the relative biological effectiveness (RBE). Although the physical dose distributions for PBS and PS proton plans may be similar, the LET and RBE distributions could differ leading to potential different outcome from PBS compared to predictions based on clinical data from PS. The aim of this project was therefore to investigate whether or not a variable RBE negates the dosimetric benefits of PBS over PS.

Materials and methods

The various dose distributions were obtained using Monte Carlo (MC) simulations, which are the most accurate way of simulating particle interactions and dose deposition. Pencil beam algorithms used by treatment planning systems (TPS) do not take individual particle interactions into account. Instead, a particle beam is viewed as a composite of several thin beams, the dose distributions of which are based on measured data. In MC, accuracy is increased as every interaction is tracked for every particle. In this project, the MC code FLUKA was used. PBS treatment plans were created for three pediatric tumor patients previously treated with PS using the single-field uniform dose (SFUD) technique. This was done using the Eclipse TPS. Both the PS and the PBS treatment plans were stored in DICOM files, which is the standard format for storing medical imaging information and data in medicine. Relevant clinical data was extracted from these files and imported into FLUKA. A script which automated the creation of the PS input was developed using the Python programming language, while an inhouse script was used for PBS. The patients were imported into FLUKA using CT images stored in DICOMs, with an inhouse calibration curve being used to convert the grey-scale images into material and density information.

Dose distributions were calculated using both a fixed and a variable RBE, the latter of which required dose-averaged LET-distributions to be calculated. The resulting data were exported into DICOM files. The results were used to compare the biological dose distributions of PS and PBS, as well as the distributions calculated by MC and the TPS. The RBE-weighted dose delivered to both the target volume and the OARs were compared.

Results

The dose estimates calculated using the Eclipse TPS and FLUKA RBE1.1 agree well for all modalities, with differences below 2%. This confirms the correctness of the implementation of PS recalculations in FLUKA. The mean variable RBE values exceeded the clinically used RBE of 1.1 for all structures and patients. The doses calculated using the variable RBEs lead to an increase in dose to all structures, independent of the modality considered. This caused the dose constraints prescribed to the brainstem core to be exceeded for all patients and modalities, with the same being true for the brainstem for 2 out of 3 patients. The LET_d values of PS were generally found to be greater than those of PBS, while the opposite was true for the RBE values. PBS exhibited a superior dose conformity for all dose calculation techniques, expressed through greater D05-D95 values and lower mean doses deposited to the OARs.

Conclusions

A variable RBE can lead to increased doses to OARs, especially at the distal ends of the treatment fields of both PS and PBS, where the LET_d and RBE values increase the most significantly. While the mean RBE within all structures were either similar or greater for PBS, it still exhibited a superior dose conformity compared to PS.

Contents

1. Introduction

The word “cancer” refers to a collection of diseases, all of which share a common trait: a few cells in the body start to divide uncontrollably and spread into nearby tissues. In contrast to healthy cells that die and divide according to the requirements of the human body, cancer cells can grow rampant and invasively, in addition to often having the ability of evading the immune system of the body. Although dependent on the type of cancer, these cells often accumulate into a cancerous tumor. Such tumors are considered malignant if they have the ability to spread to either nearby cells or organs, or to an entirely different area in the body [1].

Globally, every sixth death is caused by cancer, making it the second leading cause of death worldwide[2]. While there are a lot of ways to contract cancer, some of the most common include heavy tobacco or alcohol usage, an unhealthy diet and physical inactivity. Due to its high lethality, it is of utmost importance to both detect and treat the cancer as quickly and effectively as possible. Different types of cancer each requires a specific type of treatment, which could include surgery, chemotherapy or radiation therapy. The treatment could be palliative or curative [2].

1.1 Radiation Therapy

X-rays were discovered by Wilhelm Rontgen in 1895, and already two months later they were used by Emil Grubbe to treat a patient with breast cancer. At this point, the physical properties of X-rays were not understood nor was the biological consequences of radiation. In 1898, however, Marie and Pierre Curie discovered radioactivity and their research into the physiological effects of radiation brought with it an increased number of studies focusing on the use of radiation in medicine. During the first few decades of the 1900s, significant research was made in the area of radiation therapy and the technique became increasingly more common. In 1928, the International Commission for Radiological Protection (ICRP) was established, which exists to address the question of radioprotection. The following decades were marked by continuous scientific development within the field of radiation therapy. After surgery, radiotherapy is today the second most effective curative cancer treatment. An estimated two thirds of all cancer patients receive radiation therapy as part of their treatment [3, 4].

Using accelerated charged particles for radiation therapy was first proposed in 1946. While the first patient was treated with particle therapy in 1956, the first hospital-based facility started operation in 1990 [5]. By this time, the medical efficacy of proton beams as opposed to photon beams had been studied. While both beams deposit energy as they traverse a medium, the manner in which they do it is different. Heavy charged particles, such as protons, will deposit an increasing amount of energy as it penetrates the material in question. This energy deposition will increase until it reaches a maximum, at which point the particle comes to a halt. The depth at which the particle stops depends on its initial energy as well as the medium and particle in question [6]. Photons, on the other hand, cannot decrease in velocity. Instead, the intensity of the beam itself weakens as it penetrates a medium. This makes sparing of healthy tissue difficult when delivering a substantial dose to the target volume. How fast a photon beam is absorbed depends on the medium [7]. The depth-dose curves of photons, protons and carbon are illustrated in Figure 1.1.

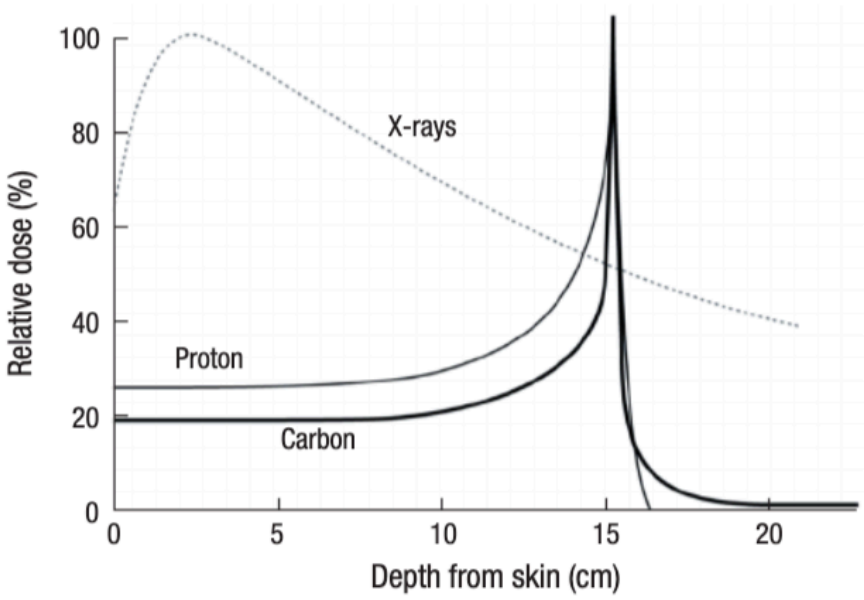

Figure 1.1: Photon and proton depth dose curves taken from [8].

Although the area of maximum dose deposition, i.e. the “Bragg peak”, is rather narrow for protons, it is possible to weight the particle fluences within the beam as desired. This makes it possible to deliver a homogeneous dose to the entire target with a single field. It is common, however, to use multiple fields, as this decreases the dose received by healthy tissues. Using

multiple beams is a necessity in photon therapy, as delivering a homogeneous dose to the target cannot be done with a single beam [9].

The relative biological effectiveness (RBE) is the ratio between the doses required by two different types of radiation in order to achieve the same biological effect. Prescription doses are defined as photon doses in order to maintain clinical consistency. The biological proton dose is found by multiplying the photon dose with the RBE of protons. Following a series of experiments in the 1960s, a constant RBE of 1.1 was assigned to protons. This is a conservative estimate made to avoid any underdosages. In reality, the RBE is variable and depends on several factors, one of which is the linear energy transfer (LET). The LET, itself a variable, is a measure of the energy deposited along the track of a charged particle which interacts electromagnetically [10].

There are two main modalities in proton therapy: passive scattering (PS) and pencil beam scanning (PBS). The former works by conforming the proton beam to the target volume within the beamline geometry, while the latter sequentially scans a thin beam across the target using magnets. Although PS has been in use the longest, PBS is becoming increasingly more common due to its superior flexibility and dose conformity [5].

1.2 Monte Carlo Simulations

The biological effect of radiation on human tissues is, for both ethical and practical reasons, challenging to investigate. While a treatment planning system (TPS) is used to create treatment plans, the dose distributions calculated by such systems tend to be somewhat inaccurate. The algorithm used by a TPS does not take individual particle interactions into account. Instead, a particle beam is divided into narrow beams. The dose contribution of each beam is calculated based on experimental beam data, making the results a compromise between accuracy and computation time [11].

Monte Carlo (MC) simulations are considered the most accurate way of calculating dose distributions in radiation therapy, as it is based on real physical models and experimental data. By tracking the physical interactions of each and every particle in the beam, a great amount of accuracy can be achieved with MC. The computation time required does, however, increase as the simulation environment becomes more complex. Uncertainties in MC calculations are

inversely proportional to the root of the number of particles simulated. While increasing the number of particles will increase the accuracy, it also brings with it an increase in computation time. This makes MC inefficient for use in the clinic [12].

The algorithms used by a TPS does not take the position of tissue inhomogeneities along the beam path into account. Instead, the dose is calculated along the beam axis using dose-to-water kernels, which are functions of water-equivalent depth. Ignoring the positions of heterogeneities relative to the Bragg peak can have a significant impact on the estimated beam range [13]. An MC code, on the other hand, takes specific material properties into account. Using real theoretical models and experimental cross-section data, particles are accurately tracked throughout the entire geometry, secondaries included. In addition to being able to calculate the dose-to-material for a range of particles, MC can calculate a variety of quantities, for instance an LET-distribution. While MC codes are very useful in radiotherapy, they are general tools used in a variety of fields [11, 13].

1.3 Project Objectives

Whereas the majority of patients so far have been treated using PS, many current and most future patients will be treated with PBS. The aim of this study was therefore to investigate differences between the techniques with respect to LET and RBE distributions. This is also necessary to enable knowledge transfer including biological dose from previously treated patients to future treatment techniques. Dose distributions were calculated for both treatment modalities using both a fixed and a variable RBE using the FLUKA MC code [14, 15]. Setting up the simulation environment required inhouse scripts which define the various beamline geometries, as well as the importation of patient specific data based on treatment plans for the PBS modality. A script was developed for the importation of PS data, from which the beamline could be defined. TPS dose distributions were also calculated in order to make comparisons with the FLUKA distributions.

Chapter 2 contains descriptions of how charged particles interact with matter. This chapter also contains some radiobiology, which includes dosimetry, the linear-quadratic model, linear energy transfer and relative biological effectiveness (fixed and variable).

Chapter 3 describes the treatment process, from imaging to treatment. This includes a description of CT, the delineation process, the various accelerators, the treatment room, as well as the two main proton therapy modalities. Additionally, a general description of MC is provided here.

Chapter 4 describes the methods used, more specifically how the MC simulations were created. This includes a basic introduction to FLUKA, along with the key components necessary for the simulations.

Chapter 5 presents the results as found through the methods described in chapter 4.

Chapter 6 contains a discussion and the conclusion, based on the aforementioned results.

2. Physics of Particle Therapy

2.1 Charged Particle Interactions in Matter

Understanding how heavy charged particles interact with matter is integral to the field of particle therapy. Protons, the primary particles considered in this project, moving through a material will interact through three distinct processes: electromagnetic interactions with the atomic electrons, electromagnetic interactions with the atomic nuclei and non-elastic collisions with nuclei. The former two processes are well understood, while the effects of the latter can be taken into account through simple approximations [16].

2.1.1 The Bethe-Bloch Equation

A heavy charged particle traversing a material will mainly lose energy through electromagnetic interactions with bound electrons, a process which ionizes and excites the material in question. This energy loss is typically referred to as the stopping power of the charged particles. The resulting ionized electrons may cause further ionizations in the medium, provided they receive enough kinetic energy from the collision with the traversing particle. Such electrons are referred to as δ-electrons. The energy loss per collision is often quite small, typically less than 100 eV, making δ-electrons with even modest energies rare. There is, however, typically a large amount of collisions per unit path length, making this an efficient mode of energy deposition in all but the thinnest layers of matter. The stopping power of a heavy charged particle is described by the Bethe-Bloch equation [6]:

$$-\left\langle\frac{dE}{dx}\right\rangle = Kz^2\frac{Z}{A}\frac{1}{\beta^2}\left[\frac{1}{2}\ln\frac{2m_ec^2\beta^2\gamma^2W_{max}}{I^2}-\beta^2-\frac{\delta(\beta\gamma)}{2}-\frac{C}{Z}\right] \tag{2.1}$$

where:

- $K = 4\pi N_A r_e^2 m_e c^2 \approx 0.307\text{MeVg}^{-1}\text{cm}^2$
- z = charge of the traversing particle in units of electron charge
- Z/A = ratio of the atomic number to the atomic mass of the traversed medium
- β = velocity of traversing particle in terms of c
- c = speed of light in a vacuum

- m_e = the electron mass
- γ = Lorentz factor
- I = mean excitation potential
- W_{max} = maximum energy transferred in a single collision
- $\delta(\beta\gamma)$ = density effect correction
- C = shell correction

The mean excitation potential is a variable which depends on the material in question and it cannot be calculated to sufficient accuracy using first principles. Instead, it is usually estimated from experimental measurements of stopping power and interpolation can be used for materials where such measurements do not exist. The mean excitation potential is approximately proportional to the atomic number of the absorbing material multiplied by 10 eV [6, 16]. Finding the maximum energy transferred in a single collision is, on the other hand, more straightforward. For a traversing particle of mass M, W_{max} is given by [6]:

$$W_{max} = \frac{2m_e c^2 \beta^2 \gamma^2}{1 + 2\gamma \frac{m_e}{M} + \left(\frac{m_e}{M}\right)^2} \tag{2.2}$$

For charged particles with relativistic energies, a divergence between the real energy loss and the stopping power calculated by Bethe-Bloch occurs. This divergence increases with higher energy and denser material. The density effect correction, $\delta(\beta\gamma)$, was added to the formula in order to account for this. This correction term becomes relevant at energies much higher than those used in particle therapy, typically at >1-2 GeV, while the energies used in proton therapy is in the 3-300 MeV range. The density correction is therefore typically ignored [16, 17].

In Bethe-Bloch, the velocity of the charged particle is required to be much larger than the velocity of the bound electrons. While this requirement is fulfilled for high particle energies, it could lead to an error of up to 6% in the 1-100 MeV range. This possible offset is corrected by the shell correction term [17].

The Bethe-Bloch equation is only valid as long as the traversing particle has an energy which is large compared to the energies of the bound electrons. While corrections can be added to the equation, making it possible to have an error below 1% down to 1 MeV, approximations

and phenomenological fitting formulas must be used to calculate the stopping power in these low energy regions [6].

2.1.2 Scattering of Particles

Charged particles moving through a material will not follow straight trajectories. Instead, they will undergo many small-angle deflections. These deflections are caused by the Coulombic interactions between the incoming particle and the nuclei of the material. This process is called multiple Coulomb scattering (MCS), and it leads to a lateral broadening of the beam. Because the scattering is the sum of many tiny stochastic deflections, the resulting angular distribution is very nearly Gaussian, with the deviation being the result of single large deflections which occur not quite infrequently enough. The Gaussian part of the distribution contains approximately 98% of the protons, which can be used for most radiotherapy purposes. There are several models available for calculating the MCS angular distribution, with Molière's theory being considered the most comprehensive and accurate for protons. Knowing the lateral broadening of the particle beam is of great importance in particle therapy, as it will affect the area of energy deposition [16].

2.1.3 Nuclear Interactions

The incoming particles will sometimes undergo inelastic collisions with nuclei in the absorbing medium. When this happens, the traversing particle will knock lose one or more proton, neutron or light nucleon cluster. The resulting nuclear fragments tend to have much lower energies and much larger angles than the incoming particle [16]. These particles will contribute to the total dose and their point of energy deposition might be outside the target volume. The latter point is of special importance when considering neutral nuclear fragments, as these do not interact electromagnetically and might therefore travel beyond the range of the primary particles [18].

2.1.4 Straggling and Range

Due to the statistical fluctuations associated with charged particle interactions in matter, determining the range of a particle beam in a given material brings with it some difficulties. A charged particle will lose energy in a series of discrete steps, leading to a variation in the particle range. This phenomenon is called straggling. Knowing the range of the particles used

in radiotherapy is of great importance, as uncertainties could lead to decreased target coverage and increased healthy tissue irradiation. The mean range of the particles can be found theoretically with the continuous slowing down approximation (CSDA). The CSDA range is obtained by integrating the reciprocal of the total stopping power from its maximum energy, E, to 0 [6, 16]. On the other hand, if one assumes that the energy-range relationship can be described by a power law, an analytical approximation can be calculated. Such approximations have been found to lead to deviations of maximum 5% when compared to measurements and numerical approaches [19].

2.1.5 The Bragg Curve

The inverse velocity dependency of the Bethe-Bloch equation means that the stopping power of a traversing particle will increase with decreasing energy. This will continue until a point of maximum energy deposition, where the particle will deposit the rest of its energy and come to a halt. The Bragg curve, which plots the stopping power of charged particles in matter as a function of depth, therefore has a characteristic peak. Beyond this peak, which is called the Bragg peak, the energy deposition of the particles should instantly fall to zero, which is indeed the case for a single particle. However, when multiple particles are considered, a small tail becomes present on the Bragg curve, due to straggling. At which depth the Bragg curve occurs, i.e. the range of the particles, depends on the incident particle energy [16]. An example of a Bragg curve is shown in Figure 2.1.

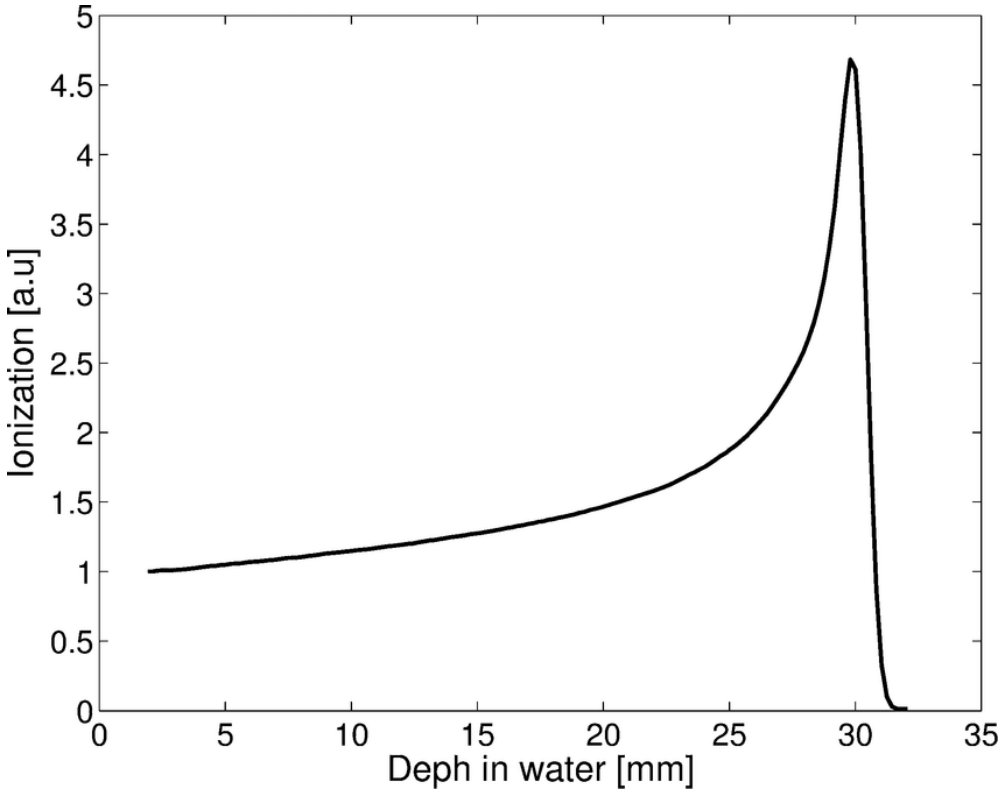

Figure 2.1: Example of a Bragg peak. Taken from [20].

As illustrated in Figure 2.1, the Bragg peak is rather narrow. However, by combining Bragg peaks of different ranges, and weighting them appropriately, one can create a spread-out Bragg peak (SOBP). SOBPs are useful in particle therapy, as their width can be chosen as desired. A particle beam can thus be conformed to the target volume in the longitudinal direction. An example of a SOBP can be seen in Figure 2.2.

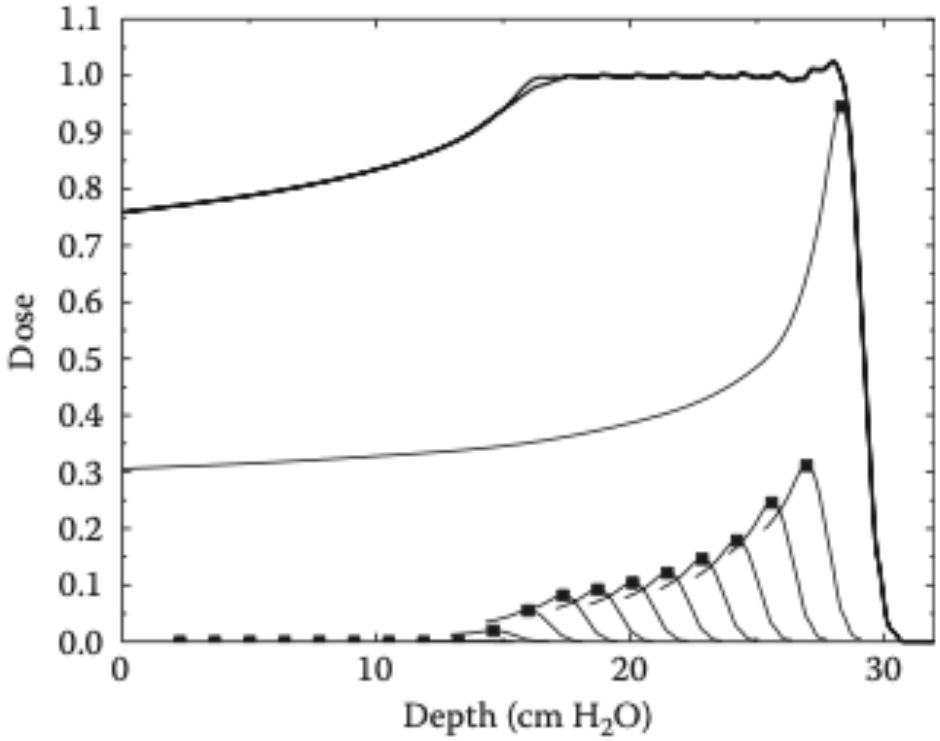

Figure 2.2: Example of a spread-out Bragg peak, taken from [16].

2.2 Dosimetry

Ionizing radiation passing through a material will deposit energy. In radiotherapy, it is of great importance to be able to determine exactly how much energy is received by a biological structure. This is quantified by the absorbed dose, which is defined as:

$$D = \frac{\Delta E}{\Delta m} \tag{2.3}$$

where ΔE is the mean energy deposited by ionizing radiation to a mass Δm. Absorbed dose is measured in Gray (Gy) in the SI system, with 1 Gy = 1 J/kg. Not all the energy lost by an ionizing particle will contribute to the dose, as some energy will be lost to secondary particles, such as neutrons and photons, which might deposit their energy outside the patient [16].

A unit dose deposited by one type of radiation might not have the same biological effect on a certain tissue as another type of radiation depositing the same dose. A weighting factor was

introduced in order to differentiate between different types of radiation, and the *equivalent dose* became defined as:

$$H_T = \sum_R w_R D_{T,R} \tag{2.4}$$

where w_R is the weighting factor for the type of radiation in question, and $D_{T,R}$ is the dose averaged over all types of tissue. The unit for equivalent dose is the Sievert (Sv), where 1 Sv equals 1 J/kg. The weighting factors for the various types of radiation are defined by the International Commission on Radiological Protection (ICRP) [21]. These are shown in Table 2.1.

Table 2.1: Radiation weighting factors as recommended by the ICRP [21].

Radiation type	**Radiation weighting factor, w_R**
Photons	1
Electrons and muons	1
Protons and charged pions	2
Alpha particles, fission fragments, heavy ions	20
Neutrons	$\begin{cases} 2.5 + 18.2e^{-\frac{[ln(E_n)^2]}{6}}, & E_n < 1MeV \\ 5.0 + 17.0e^{-\frac{[ln(2E_n)]^2}{6}}, & 1MeV \leq E_n \leq 50MeV \\ 2.5 + 3.25e^{-\frac{[ln(0.04E_n)]^2}{6}}, & E_n > 50MeV \end{cases}$

The equivalent dose does not take the type of irradiated tissue into consideration. The *effective dose* was introduced to include weighting factors for the various types of tissue. The effective dose is defined as:

$$E = \sum_T w_T H_T = \sum_T w_T \sum_R w_R D_{T,R} \tag{2.5}$$

where w_T is the weighting factor for the type of tissue in question. The unit for effective dose is also the Sievert [21]. The weighting factors are again determined by the ICRP and are shown in Table 2.2.

Table 2.2: Tissue weighting factors as recommended by the ICRP [21].

Tissue	w_T	$\sum w_T$
Bone-marrow (red), Colon, Lung, Stomach, Breast, Remainder tissues	0.12	0.74
Gonad	0.08	0.08
Bladder, Oesophagus, Liver, Thyroid	0.04	0.16
Bone surface, Brain, Salivary glands, Skin	0.01	0.04

2.3 Radiobiology

The goal of radiation therapy is to irradiate cancer cells using as much ionizing radiation as possible, while simultaneously minimizing the damage to healthy cells. It is therefore of great importance to know how radiation affects living tissue. Radiobiology combines the fields of physics and biology and studies the effects of ionizing radiation on biological cells. A cancer cell is considered killed when it loses its reproductive ability. A cell can become unable to proliferate if its DNA molecules gets damaged.

Charged particles are directly ionizing, which means that they are able to directly damage the DNA. Direct damage to the DNA, which is called “direct action”, would typically lead to either a single- or a double strand break (SSB and DSB, respectively). Although SSBs are easily repaired by the cell, they can cause a DSB if they happen in close proximity to each other. DSBs are much more difficult to repair than SSBs and will ideally make the cell unable to proliferate.

For protons in the energy range 0.5-100 MeV, ~70% of the energy lost will be transported away by the δ-electrons they produce. These electrons might then ionize further, as well as

cause further strand breaks. Charged particles can also cause indirect damage to the DNA-strands by creating free radicals through interactions with the water inside the cell. These free radicals can then damage nearby DNA. At low LET, most of the damage done to DNA is through indirect action. The effects of direct action becomes more pronounced with increasing LET [10]. Figure 2.3 illustrates both direct and indirect action.

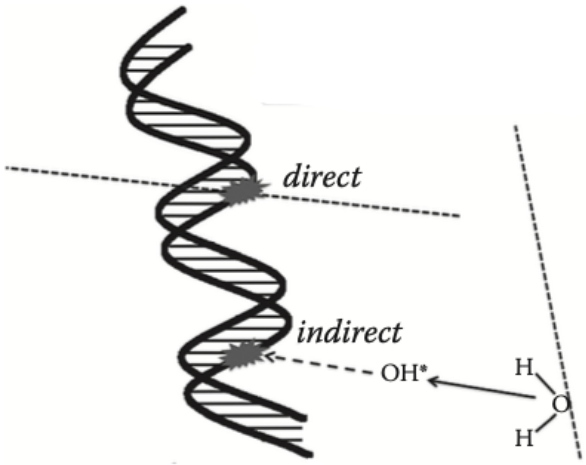

Figure 2.3: Direct and indirect action. Modified from [10].

2.3.1 The Linear-Quadratic Model

In the linear-quadratic model (LQ model), the survival probability of an irradiated cell is given by the following equation:

$$S = e^{-\alpha D - \beta D^2} \tag{2.6}$$

where D is the exposure dose, and α and β are the linear and quadratic parameters, respectively, which describe the radiosensitivity of the cells in question. Plotting cell survival on a log scale yields a dose-response curve, as illustrated in Figure 2.4. The α/β-ratio, which is given in Gy, is defined as the dose where both components of equation 2.6 contribute equally to the cell killing. The ratio describes the curvature of the cell survival curve, with a lower ratio corresponding to a greater curvature. The α/β-ratio depends on the type of irradiated tissue [22].

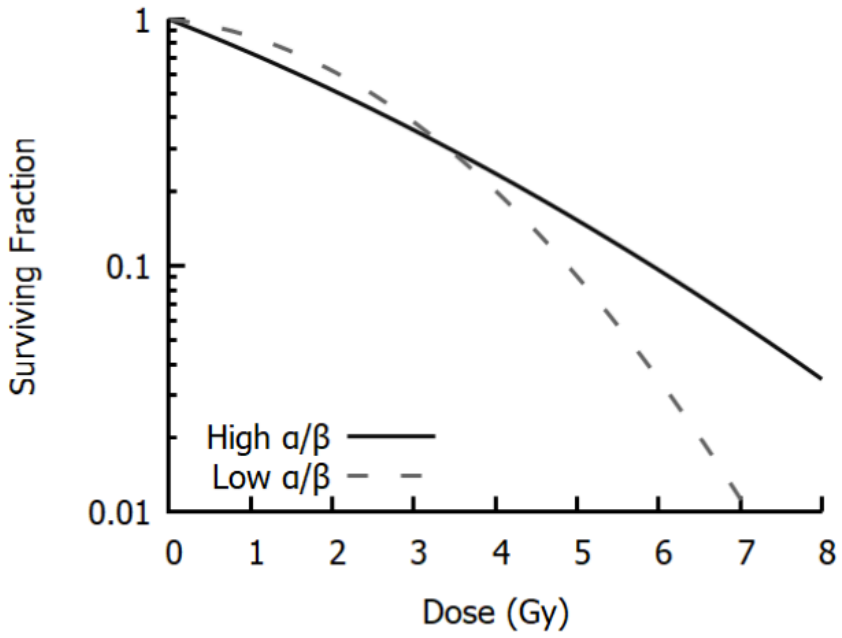

Figure 2.4: Example of dose-response curve. Taken from [22].

A high α/β-ratio (7-10 Gy) typically characterizes early responding tissue, while a low α/β-ratio (3-5 Gy) corresponds to late responding tissue. The cell survival curve of an early responding tissue is less curved than for late responding tissue. This means that while the former sees a relatively constant rate of cell killing with increasing treatment fractions, the latter does not. Rather, the surviving fraction of late responding tissue decreases more significantly as the dose increases. Malignant tumors tend to have a high α/β-ratio, which means the rate of cell killing will be relatively constant. Splitting the dose into several smaller fractions can therefore increase the sparing of healthy tissue with a lower α/β, such as lungs, the brainstem and the heart [22, 23].

2.3.2 Linear Energy Transfer

Linear energy transfer (LET) is a measure of the energy deposited to a medium along the track of a charged particle interacting electromagnetically. It is defined as:

$$LET = \frac{dE}{dl} \tag{2.7}$$

LET is the amount of energy deposited per unit length, with a greater value corresponding to a greater ionization density along the particle trajectory. Its unit is $keV\mu m^{-1}$ [7]. For heavy charged particles, the LET value increases greatly with decreasing energy, which is to be expected from Figure 2.1.

Equation 2.7 describes what is called the *unrestricted* LET (LET_∞), which is the total electronic stopping power. This quantity can be used to calculate the absorbed dose, which at a given point is the product of the electronic stopping power and the particle fluence. Because the LET varies over the particle track, it is beneficial to use averaged LET values. The dose averaged LET (LET_d) is the most commonly applied LET in radiation therapy, as it takes both the unrestricted LET and the dose into account. It is found through the following formula [24]:

$$LET_d(z) = \frac{\int_0^\infty S_{el}(E)D(E,z)dE}{\int_0^\infty D(E,z)dE} = \frac{\int_0^\infty S_{el}^2(E)\Phi(E,z)dE}{\int_0^\infty S_{el}(E)\Phi(E,z)dE} \tag{2.8}$$

where E is the energy of the primary charged particles, $S_{el}(E)$ is the electronic stopping power, i.e. the unrestricted LET, D(E, z) is the absorbed dose deposited at point z, and Φ(E, z) is the fluence of the particles at a point z. Figure 2.5 illustrates how the LET increases with depth.

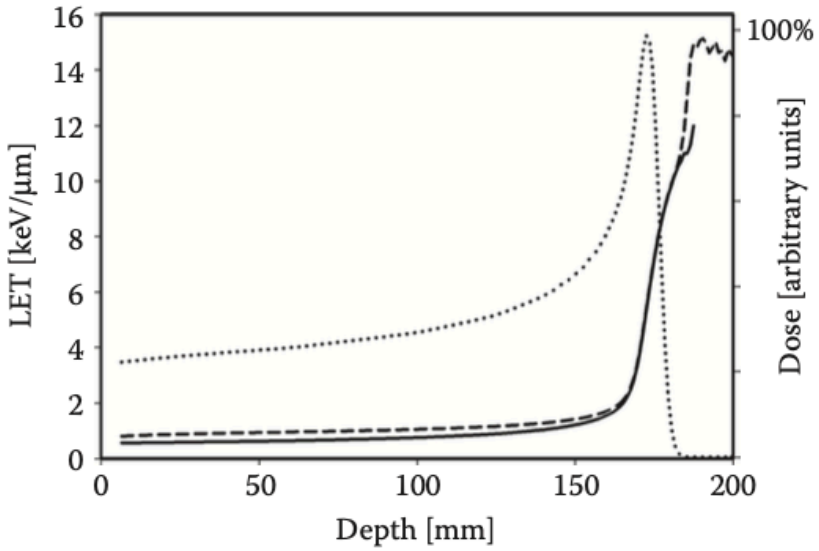

Figure 2.5: Dose-averaged LET for primary particles (solid line) and for all particles (dashed line). The dotted line represents dose. Taken from [10].

2.3.3 Relative Biological Effectiveness

When assessing the biological effects in radiation therapy, the ICRP does not recommend using the radiation and tissue weighting factors described in chapter 2.2, as these were primarily intended to be used for radiation protection [21]. Instead, the biological effectiveness of a given type of radiation can be calculated using the relative biological effectiveness (RBE) and the absorbed dose. RBE is defined as the ratio between a reference dose D_x and a dose D, with both doses producing the same biological effect. This is expressed in equation 2.9 [10]:

$$RBE = \frac{D_x}{D} \tag{2.9}$$

Due to a large amount of clinical data, and to maintain clinical consistency, 250 kV x-rays are typically used as the reference radiation type. The RBE is used to convert physical dose to biological dose, i.e. RBE-weighted dose [7]. In proton therapy, a constant RBE of 1.1 has been used. However, it has been shown that this value might not be entirely correct [23, 25]. While an RBE of 1.1 seems reasonable for low LET-values, an increase in LET leads to an increase in RBE as well. This relationship is illustrated in Figure 2.6. As the figure shows, at around 100 keVμm^{-1} the RBE reaches a maximum, a point beyond which the RBE declines due to an increasingly inefficient ionization density [7].

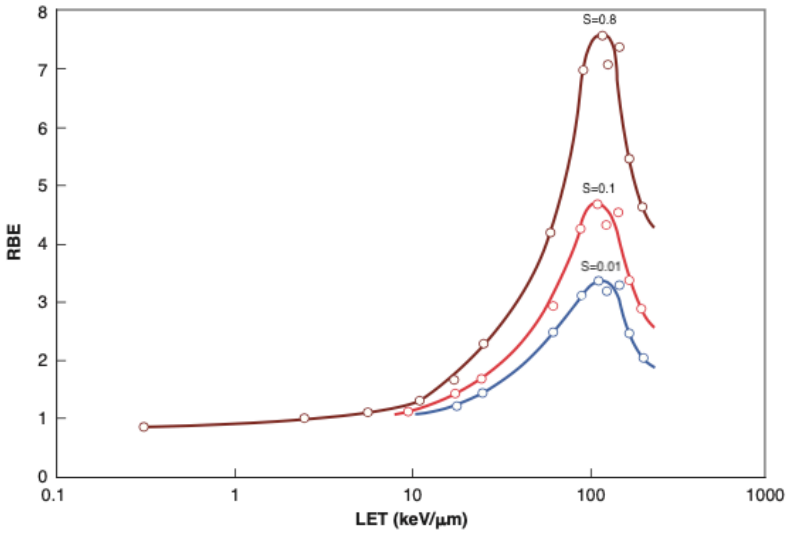

Figure 2.6: The relationship between RBE and LET in mammalian cells for different cell survivals (S). Taken from [7].

There are several proposed models which give a varying RBE-value by taking values such as LET_d and tissue type into account [25]. Using the LQ model, one can obtain a general expression for RBE:

$$RBE = \frac{D_x}{D} = -\frac{1}{2D}\left(\frac{\alpha_x}{\beta_x}\right) + \frac{1}{D}\sqrt{\frac{1}{4}\left(\frac{\alpha_x}{\beta_x}\right)^2 + \frac{\alpha_p}{\alpha_x}\left(\frac{\alpha_x}{\beta_x}\right)D + \frac{\beta_p}{\beta_x}D^2} \tag{2.10}$$

where α_x and β_x are the LQ parameters which describe the reference radiation, and α_p and β_p describe the proton radiation. The reference parameters are obtained using clinical data, while the manner in which the proton parameters are obtained depends on the RBE model used.

Using a variable RBE, as opposed to a fixed RBE, is predicted to not only affect the dose received by the target volumes, but by any potential nearby OARs as well. This might especially be the case for any OARs located close to the end of the particle beam range, as the LET_d increases significantly here. Additionally, a variable RBE might introduce hot and cold spots in the target area, which could negatively affect the prescribed target coverage [23, 25].

The variable RBE model used in this project was the McNamara model, in which the proton LQ parameters are found through the following equations [26]:

$$\frac{\alpha_p}{\alpha_x} = 0.99064 + \frac{0.35605}{\frac{\alpha_x}{\beta_x}}LET_d \tag{2.11}$$

$$\frac{\beta_p}{\beta_x} = \left(1.1012 - 0.0038703\sqrt{\frac{\alpha_x}{\beta_x}}LET_d\right)^2 \tag{2.12}$$

3. Treatment Planning and Delivery

The treatment planning process is one of the most important elements of radiation therapy and consists of several multidisciplinary steps, where clear and ongoing communication is necessary. Treatment planning requires not only clinical information, anatomical data and dose prescriptions, but also an understanding of the limits and possibilities of the various treatment modalities [27].

The aim of the planning process is to design a plan which delivers as high a dose as possible to the target volume, while simultaneously minimizing healthy tissue complications. Meeting the dose prescriptions and constraints given to the target volume and the OARs might not be possible at the same time, however. This makes the treatment planning process one of compromise. During treatment planning, two dose-response curves are of great importance: the tumor control probability (TCP) and the normal tissue complication probability (NTCP) [27]. These curves, illustrated in Figure 3.1, plot their respective probabilities as a function of dose. The area between the two curves is known as the therapeutic window. A critical objective in radiotherapy is to increase the size of this window, thus reducing potential healthy tissue complications.

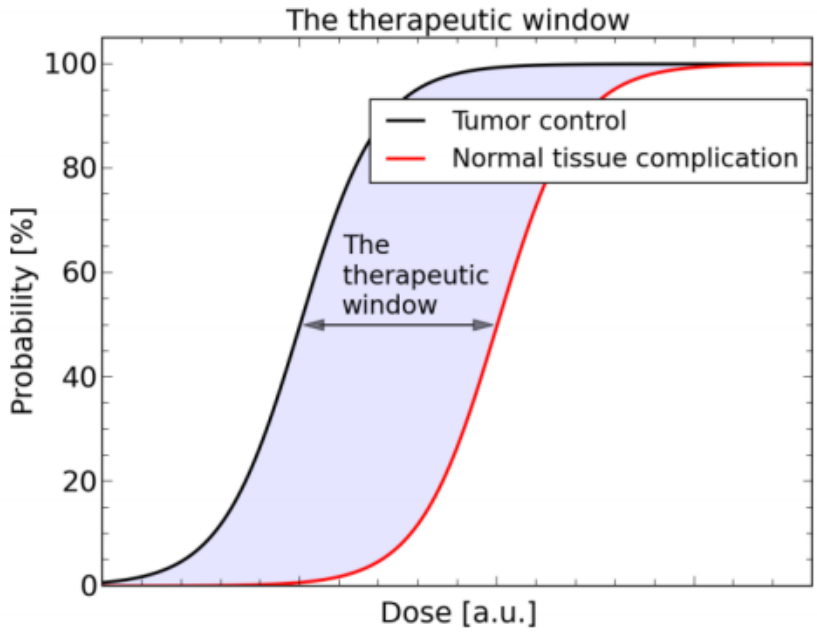

Figure 3.1: TCP, NTCP and the therapeutic window. Taken from [18].

3.1 Treatment Planning

3.1.1 Image Acquisition

The first part of the treatment planning process is to obtain anatomical images of the patient. The images are needed in order to accurately assess the size and position of the target volume, as well as any potential organs at risk [27].

The imaging gold standard in radiotherapy is computed tomography (CT), as this modality allows for the acquisition of tissue density information. CT is an X-ray imaging procedure in which a beam of X-rays is continuously scanned around the patient in a helical fashion, producing a series of cross-sectional images of the patient. The continuous scanning leads to fewer motion artefacts, in addition to shorter scanning time. The image-slices, an example of which is shown in Figure 3.2, are digitally stacked together, yielding a three-dimensional image of the patient [28].

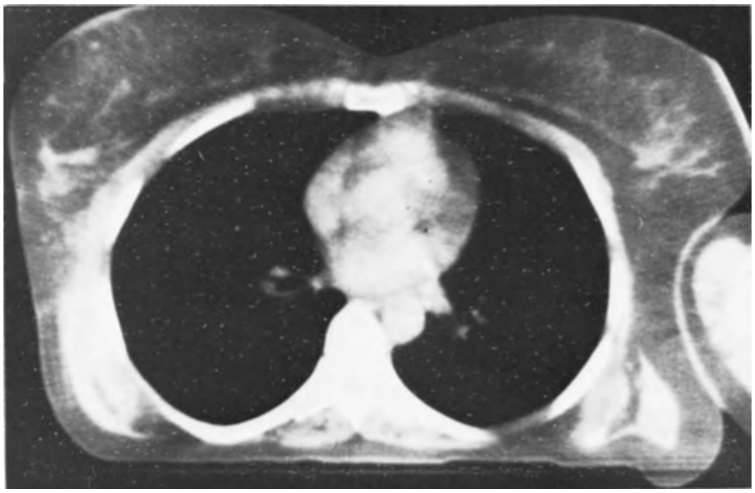

Figure 3.2: Example of a CT image showing the heart and lungs. Darker areas correspond to low density tissue (such as the lungs) and lighter areas correspond to high density tissues (such as the heart). Taken from [28].

Electromagnetic radiation moving through a medium will decrease in intensity. The degree of attenuation depends on the medium in question and is expressed through the linear attenuation coefficient, μ, associated with the given material. This is expressed through equation 3.1.

$$I(x) = I_0 e^{-\mu x} \tag{3.1}$$

where I_o is the initial beam intensity, I(x) is the final intensity, x is the absorber thickness and μ is the linear attenuation coefficient. The differently attenuated X-ray images are stacked together into a gray scale CT image, in which darker areas correspond to low density tissues and vice versa [28].

3.1.2 The Hounsfield Unit

Gray-scale CT images are generated by assigning a Hounsfield Unit (HU) to areas of different attenuation, i.e. tissue density. The HUs, which are dimensionless, are calculated and assigned a voxel by linearly transforming the linear attenuation coefficients using equation 3.2:

$$HU = 1000 \times \frac{\mu_{tissue} - \mu_{water}}{\mu_{water}} \tag{3.2}$$

As can be seen from the equation, water is defined to have HU=0. Additionally, air is defined to have HU=-1000. The HUs are assigned a gray-scale intensity, with greater numbers corresponding to brighter areas, from which a gray-scale image can be formed. HUs can be transformed into relative stopping power values needed for range calculations in proton therapy [28, 29]. This is done by using a CT calibration curve, which like the HUs are machine specific. The most common way of acquiring such a curve is the stoichiometric method, which makes use of a phantom comprised of tissue surrogates of known elemental compositions. These surrogates are then scanned and the resulting HUs are used to obtain a calibration curve through linear regression [30].

3.1.3 Regions of Interest

After scanning the patient, the acquired images are given over to a radiation oncologist. They will locate and mark the positions of the various volumes of interest, such as the target volume and potential organs at risk (OARs). The various targets and volumes which are used in radiation therapy are defined in ICRU Report 50 [3].

The gross target volume (GTV) is the volume which most closely encompasses the macroscopic target tumor volume. The position, extent and shape of the GTV is typically determined by studying images acquired through medical imaging, but these properties might

also be found through clinical examination. The GTV should receive a high dose to its entire volume, as it will have a large tumor cell density [27, 28].

The clinical target volume (CTV) includes the GTV with an added error margin. Not all malignancies are detectable in the clinic, and tumor cells might extend beyond the borders of the GTV. The CTV encompasses the area where proliferative tumor cells are expected to be. This entire volume must be adequately irradiated in order to cure the malignancy [3].

The GTV and the CTV are both delineated without any regard for patient movement, range inaccuracies or other errors in the setup. The planning target volume (PTV) takes such potential problems into account by adding an extra margin of error around the CTV. This minimizes the discrepancies between the planned and delivered dose received by the CTV [3]. The different target volumes are shown in Figure 3.3.

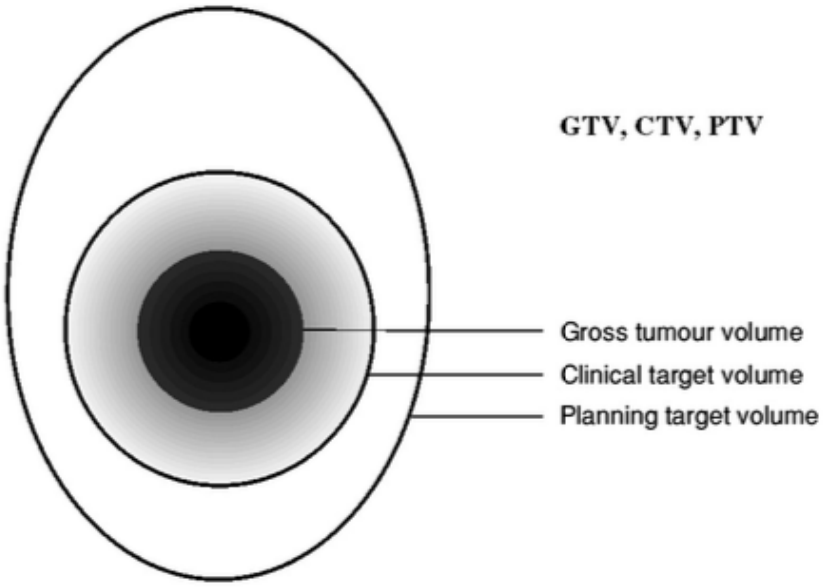

Figure 3.3: The different target volumes. Taken from [3].

In addition to delineating the target volume, it is of high importance that the various OARs are marked as well. OARs include nearby healthy tissues and organs with high radiosensitivity that needs to be spared. In order to achieve maximum sparing, the OARs are delineated with an extra margin, like the CTV and the PTV [28].

Once the relevant structures have been delineated, the dose planning process can begin. In addition to delineating the various regions of interest (ROIs), the physician also provides a dose prescription to be delivered, as well as dose constraints for the OARs. These are then entered into the treatment planning system (TPS) [27].

3.1.4 The Treatment Planning System

Once the relevant structures have been delineated and assigned a dose prescription and constraints, a treatment plan can be created. This can be done using a TPS, with which it is possible to determine a three-dimensional dose distribution to be delivered to the patient. Using the clinical information, which is imported into the TPS, a virtual representation of the patient can be created, delineated structures included. The aim of the treatment plan is to satisfy the prescription to the target volume as accurately as possible, while delivering as little dose as possible to the OARs and healthy tissues. The dose constraints prescribed for the OARs are upper limits, and the goal is to minimize the dose to these volumes. It is often difficult to meet all these criteria exactly, however, due to the constraints stemming from the size of the therapeutic window. This is especially true when there is more than one OAR to consider. Additionally, certain OARs might be assigned dose constraints which are not to be exceeded under any circumstances [27].

While a proton beam is able to deliver the entire dose prescription homogeneously to the target volume from only one direction, it is common to use multiple fields. This way, increased sparing of healthy tissue is achieved. How the treatment fields are optimized depends on which proton therapy modality is chosen, i.e. passive scattering (PS) or pencil-beam scanning (PBS). Both of these modalities are explained in more detail in section 3.3, but in short: PS irradiates the entire target at once after conforming the beam in the beamline, while PBS sequentially scans over the target with a thin beam. The former is less flexible than the latter, as PBS has the ability to deliver a much more heterogeneous dose distribution. This makes it possible to increase healthy tissue sparing, in addition to allowing for intensity modulated proton therapy (IMPT) [27].

In IMPT planning, multiple fields are optimized simultaneously using the prescribed dose constraints. When using such multi-field optimization (MFO), the fluence of each pencil beam is optimized at the same time. This means that while the total dose delivered to the target will

be homogeneous, the contribution from each field might not be. Inverse optimization is a gradient-based, iterative process, in which a series of plans is generated based on the given dose objectives and constraints. These plans are automatically assessed, and the best one is chosen. This plan will still require an assessment by the treatment planner [31, 32].

A PS plan is not made using inverse treatment planning. Instead, treatment plans are created using the single-field uniform dose (SFUD) technique, in which each field delivers a homogeneous dose to the target. These fields are designed individually before being linearly added together. SFUD can be used for both PS and PBS, with the latter achieving a better dose conformity to the target, as well as increased sparing of healthy tissue. This is because PBS can weigh the individual pencil-beams as required [27].

Clinical planning systems calculate dose distributions using analytical pencil beam algorithms, which treat proton beams as composites of a set of narrow pencil beams. The dose deposition is calculated along the axis of each pencil beam, using experimentally measured depth-dose curves and lateral beam profiles. The contributions of each pencil beam are then added together, resulting in a complete dose calculation for the patient [13, 31].

3.1.5 Treatment Plan Assessment

Before being used for treatment, every treatment plan needs to be assessed by the radiation therapist. This can be done directly in the TPS. The dose distribution can be visually inspected using an isodose distribution or a color wash overlaid on the CT images with a well-defined color bar, in which warmer colors typically represent areas of higher dose and vice versa. The dose conformity can be found using isodose curves, which are contours marking regions to which a particular dose percentage is delivered [28]. Such visual displays, while helpful, are not enough to properly evaluate a treatment plan, as it provides no information about the dose received by the various structures. This information can be acquired by using a dose volume histogram (DVH), which shows how much dose is received by a given percentage of a structure of interest. DVHs do not, however, contain any information about the dose conformity [33].

3.2 Particle Accelerators

The energies used in particle therapy is of such a magnitude that a particle accelerator is necessary. There are two main types of ion accelerators: cyclotrons and synchrotrons [34]. Cyclotrons, an example of which is illustrated in Figure 3.4, are circular and the particles that are to be accelerated start out at the center. Using magnetic fields and a rapidly varying electric field, the particles are accelerated in an outward spiral until they reach the maximum energy allowed by the cyclotron, at which point they are extracted. The advantage of a cyclotron is the ability to deliver a continuous beam of particles, which a synchrotron is unable to do. A disadvantage of cyclotrons is that they can only accelerate the particles to a fixed energy due to the nature of their design. Additionally, they are poorly suited for ions heavier than protons. Cyclotrons typically accelerate protons up to the energy range of 230-250 MeV, which is at the upper end of the energies typically used in proton therapy. Lower energies can be achieved through energy modulation, which for cyclotrons has to happen after the extraction of the particle beam. This way of modulating the energy beam is called *passive modulation* and works by putting a degrader in front of the beam. This can be done immediately after extraction or within the treatment nozzle itself [34].

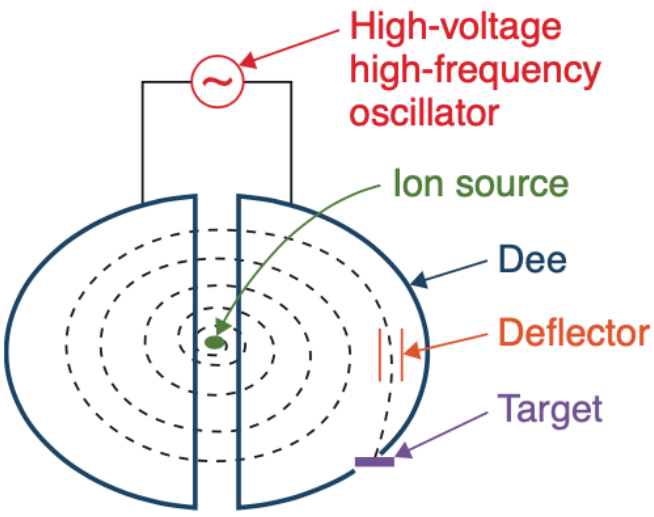

Figure 3.4: Illustration showing how cyclotrons work. Taken from [28].

Synchrotron accelerators, an example of which is illustrated in Figure 3.5, are much larger than cyclotrons, and they have the ability to achieve much higher energies. One or more linear accelerators must be part of the particle injection system, as the particles need to be accelerated to a few MeV before being inserted into the synchrotron. The synchrotron itself is circular, or close to circular, and consists of a large evacuated tube and strong magnets used for bending the particle trajectories as well as for beam focusing. By adjusting the magnetic field strength in a synchrotron, it is possible to vary the energies to which particles are accelerated within the accelerator itself, which is called *active modulation*. A disadvantage of synchrotrons is its inability to quickly extract the particle beam [34].

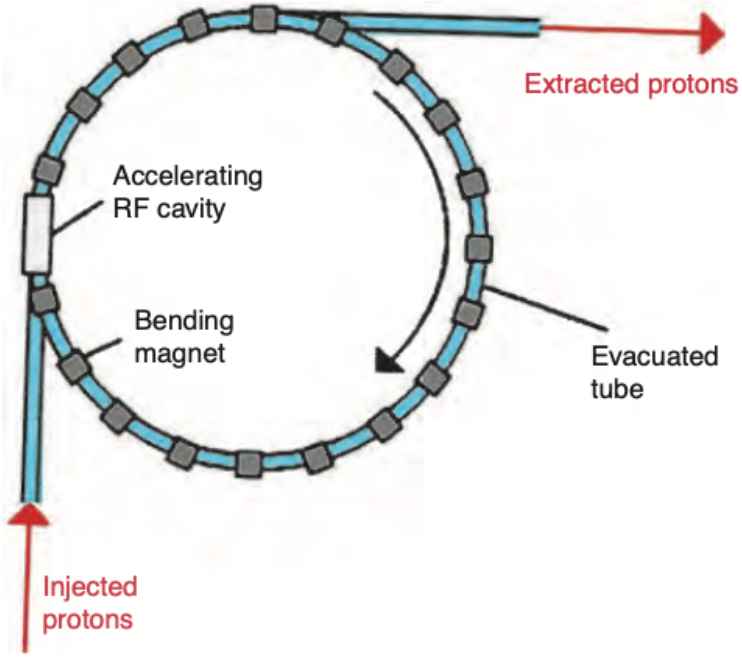

Figure 3.5: Illustration showing how synchrotrons work. Taken from [28].

3.3 Particle Therapy Modalities

Once the particle beam has been accelerated it needs to be conformed to the target volume. As mentioned above, the two major delivery techniques in particle therapy are called passive scattering (PS) and pencil beam scanning (PBS) The former modality is the oldest and is historically the most widespread, although the latter is becoming more common. While these modalities may have some commonalities, such as ionization chambers used for beam monitoring [29], their geometry is quite different.

3.3.1 Passive Scattering

PS works by first spreading the beam in both the lateral and longitudinal direction. In the lateral direction, this is commonly done using one or two scatterers (referred to as the first and second scatterer, respectively) of high-Z material, such as lead or brass. The first scatterer is typically thin and flat and is used for spreading the beam onto the second scatterer, provided it is not a single scatterer system. Second scatterers can have a variety of configurations, some of which are shown in Figure 3.5, and aim to spread the beam out as uniformly as possible. One example is the contoured scatterer, which is thicker at the center and thinner at the edges. A low-Z material is often applied to the second scatterer for energy compensation. This is done to make sure the energy, and thereby the range, is equal across the lateral beam distribution [35]. Additionally, variable collimators can be included in order to reduce the proton fluence in the beamline geometry, as this could lead to an increased neutron background [36].

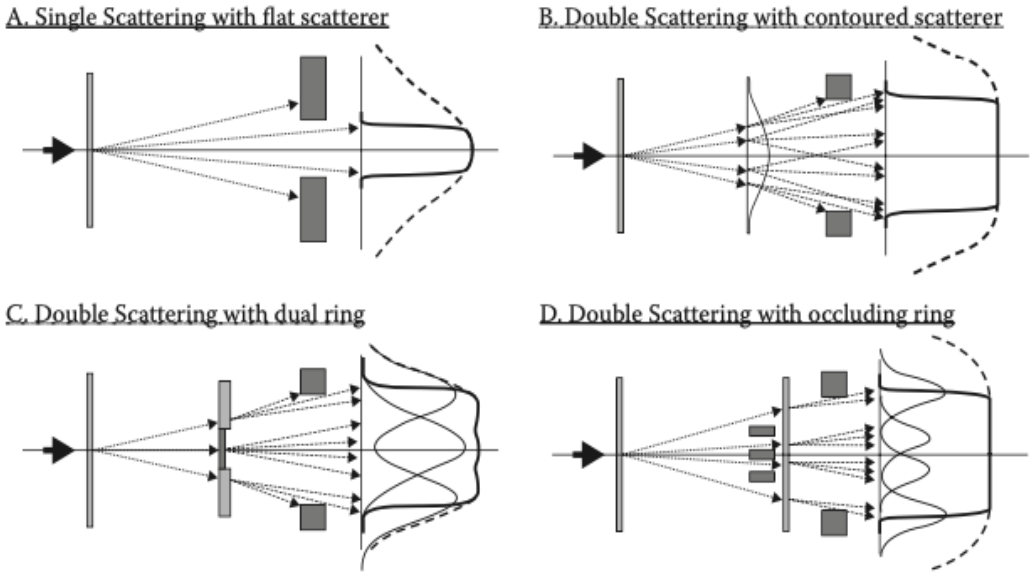

Figure 3.6: Various possible configurations of scatterers. Taken from [35].

Spreading the beam out longitudinally is done by creating a spread-out Bragg peak (SOBP). This is done by applying a range modulation technique, such as utilizing a ridge filter or a range modulation wheel (RM wheel), with the latter being the most commonly used. By having different parts of the beam move through low-Z material of different thickness one produces several Bragg peaks [36]. The individual Bragg peaks can be weighted as desired,

and together they create a SOBP. For an RM wheel this is achieved by rotating a wheel consisting of different steps in front of the particle beam, with each step having a certain thickness. The widths of the steps are chosen such that the SOBP is as flat as possible, making each RM wheel usable for a very small range of beam energies. If the desired modulation width is thinner than the widest one allowed by the RM wheel, only parts of the wheel needs to be irradiated. This can be achieved by either turning the beam on and off, synchronized with the wheel rotation, or by covering parts of the wheel so that particles are unable to pass through. This makes it possible to use the same RM wheel for several modulation widths. Additionally, by using beam current modulation (BCM), a complex feedback technique, one can alter the beam current and achieve a flat SOBP for an even wider range of energies per RM wheel [37].

Once the beam has been spread out both laterally and longitudinally it needs to be conformed to the target volume. An aperture is used to conform the beam in the lateral direction. The shape of the aperture is defined by the back projected shape of the target volume, using extra margins which account for uncertainties in penumbra and setup. The aperture is made from a high-Z material, such as brass, due to the large stopping power required [35].

Conforming the dose to the target volume in the longitudinal direction requires a range compensator. Such compensators are designed to remove the depth variation by adding more absorbing material in areas of smaller depth and less material in areas of greater depth. A low-Z material is used to ensure low scattering. Like the aperture, the compensators have to be unique for each treatment field [35, 36]. The complicated setup illustrates one of the drawbacks of PS. Each field requires a unique aperture and compensator, in addition to a specific configuration of scatterers and range modulators. Another drawback is that protons will interact with the scattering and range modulation materials, which leads to energy loss, the creation of secondary particles and angular diffusion, which increases the lateral penumbra of the beam. PS is, however, quite robust and requires less sophisticated systems than PBS. Additionally, the whole target is irradiated semi-instantaneously, making PS less sensitive to organ motion [35]. Passive scattering is illustrated in Figure 3.7.

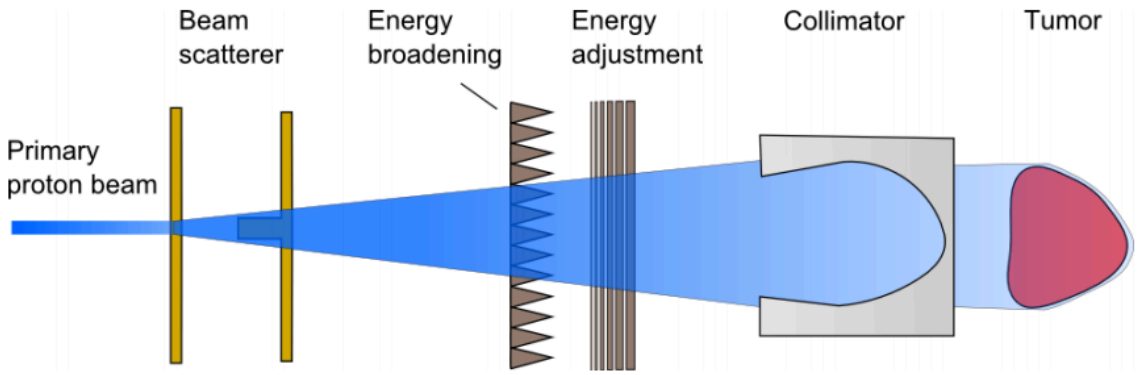

Figure 3.7: Illustration of the passive scattering technique. Taken from [18].

3.3.2 Pencil Beam Scanning

PBS requires fewer components than PS, as the beam is not passively spread out before delivery. Instead, a pair of dipole magnets are used to steer the beam in both the horizontal and vertical direction. The strengths of their respective fields are adjusted during treatment, making the sequential scanning possible in the lateral direction [38].

By varying the energy, different depths of dose deposition are achieved. The beam can thus be scanned over the target volume, slice by slice. The scanning can either happen discretely, meaning the beam is turned on and off between each voxel, or it can scan continuously over a layer. It is of great importance to know the various beam parameters during scanning, so feedback systems and precise beam control needs to be in place for this modality. Active scanning is more efficient than PS as it requires no patient-specific hardware. This also means that the beam interacts with less material before it reaches the target, creating fewer secondaries. A higher dose conformity to the target and increased sparing of healthy tissue is also achieved with PBS, as each beam can be weighted as required. Additionally, PBS is more susceptible to organ motion, as the dose is delivered sequentially [38]. PBS is illustrated in Figure 3.8.

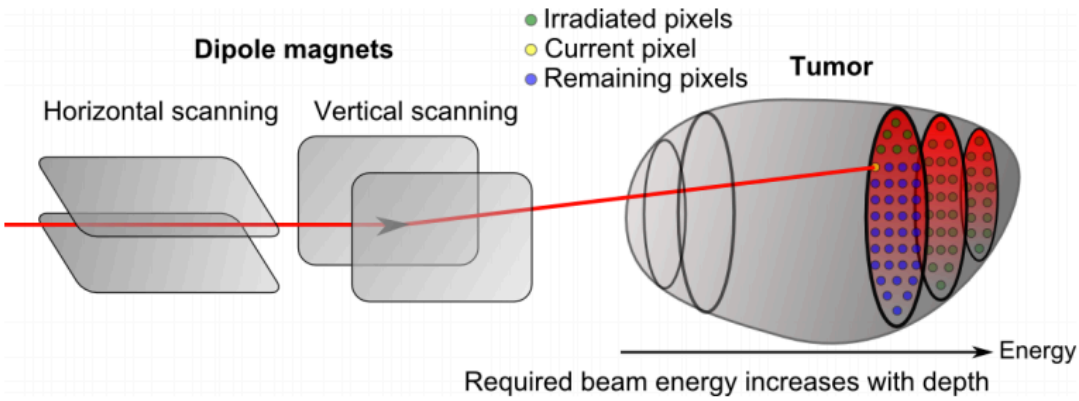

Figure 3.8: Illustration of pencil beam scanning. Taken from [18].

3.4 The Beam Profile

Regardless of the chosen treatment modality, an aim of proton therapy is to deliver as conformal a dose as possible to the target. One way to assess whether or not this is achieved is by looking at the dose distributions in the lateral and longitudinal direction. Both distributions can be described by specific parameters, also called “dosimetric indices”. Figure 3.9 illustrates various dosimetric indices used to describe the SOBP dose distribution, i.e. the depth-dose distribution, with the dose being normalized to 100% at the dose plateau.

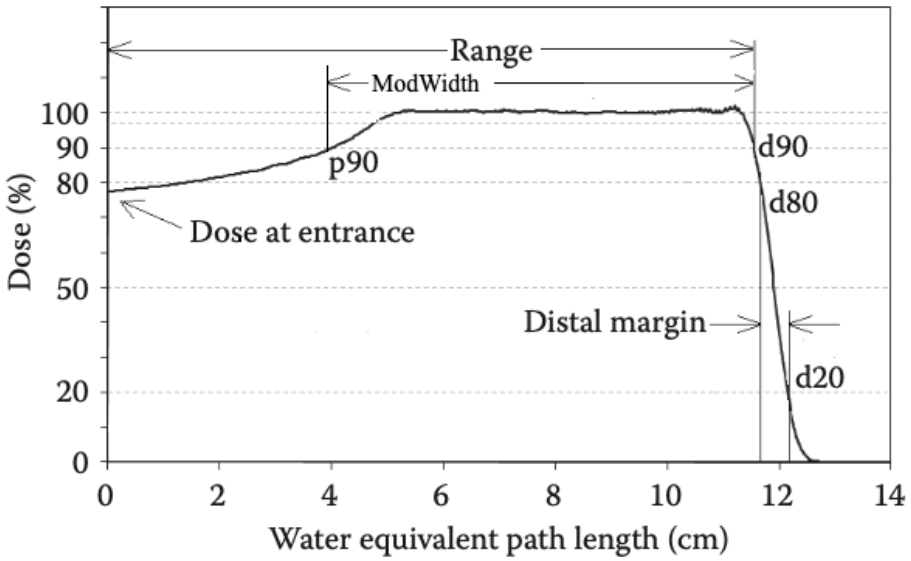

Figure 3.9: Depth-dose distribution. Modified from [9].

Here, the dosimetric indices define the depth at which specific dose levels are found, with the prefixes referring to the proximal and distal ends of the beam ("p" and "d", respectively). For example, the p90 parameter refers to the proximal depth at which 90% of the dose is delivered. The most clinically relevant parameters, i.e. the range and modulation width, are typically defined by d90 in the former case, and by the distance between p90 and d90 in the latter case. However, some radiotherapy clinics rather use d80 for range and/or define the distance between p98 and d90 as the modulation width. The distal margin, also called the distal dose falloff (DDF), is defined by the distance between d20 and d80 [9]. A compromise between a flat dose profile and a sharp DDF typically has to be made, as a sharper DDF can be achieved by increasing the weight of the distal peak and reducing the weight of the second peak. This would, however, lead to hot and cold spots in the dose distribution. Similarly, an improvement in the flatness of the dose distribution would also increase the DDF shoulder [35]. An example of a lateral dose distribution is shown in Figure 3.10.

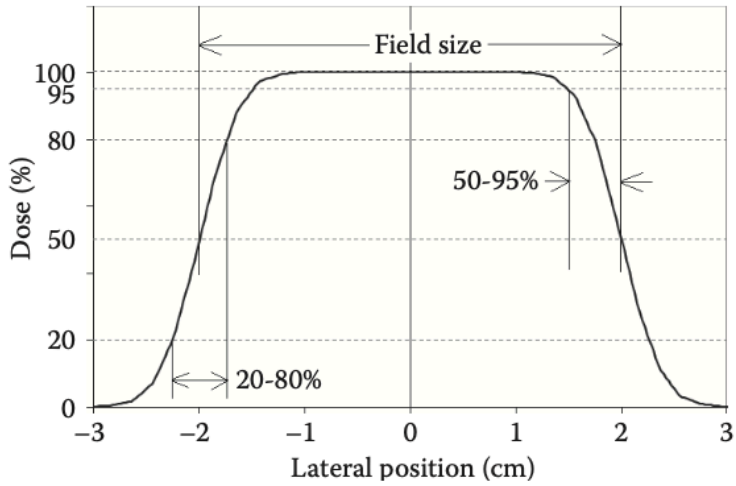

Figure 3.10: Illustration of a lateral dose distribution. Taken from [9].

The field size is defined at the 50% level, while the lateral penumbra can be specified by both 20%-80% and 50%-95%. The former is commonly used when describing the general quality of the penumbra, while the latter is needed for determining the margins of an aperture in the PS modality [9].

3.5 The Treatment Room

The treatment room consists of the gantry and the patient treatment table. The patient is placed on the table, with great care being put into reproducing the position they were in during imaging. One way to achieve this is through the use of wedges and accessories holding the patient in place. There are also techniques in place which minimizes the various errors associated with organ or respiratory motion [28].

3.5.1 Patient Orientation

The relative orientation of the patient and the beam is of great importance in particle therapy. Usually, the orientation of both the beam and the patient can be manipulated. This is done by rotating the gantry and the treatment table, which allows for a wide range of treatment angles.

How the patient is orientated on the table will depend on the location of the target volume, as this might affect the angles of irradiation. The most common patient orientation is Head First – Supine (HFS), where the patient lies on their back, facing towards the ceiling. This, as well as other common orientations, are shown in Figure 3.11.

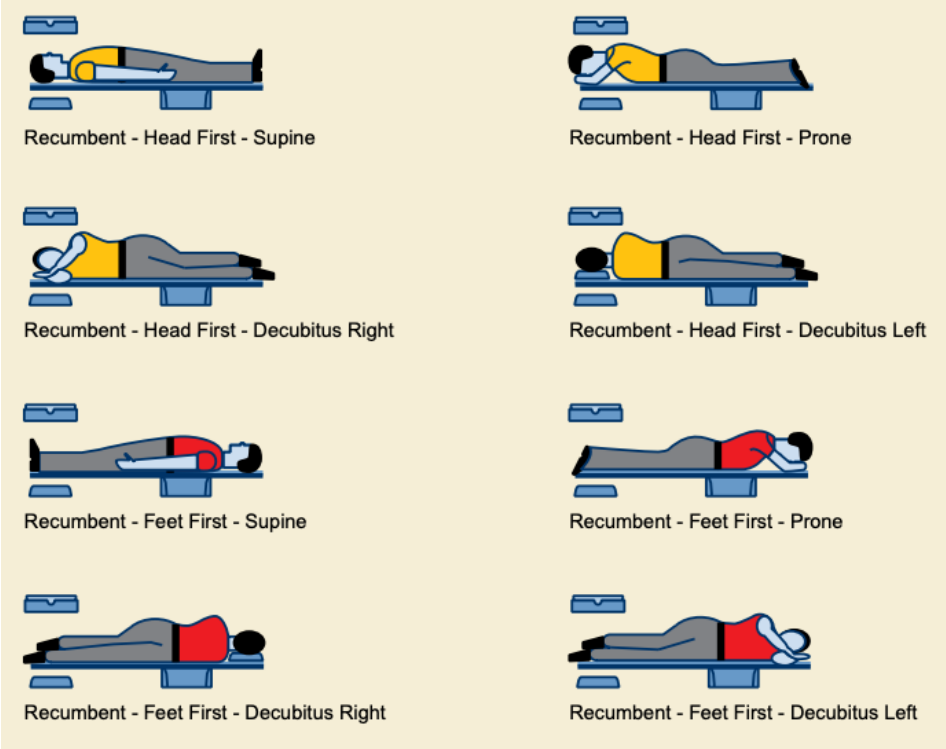

Figure 3.11: Various patient positions in radiation therapy. Taken from [39].

3.5.2 Coordinate Systems

The coordinate systems associated with the patient and the treatment room are defined by the International Electrotechnical Commission (IEC). The fixed and gantry systems are both coordinate systems within the treatment room. As the name would suggest, the former system is fixed within the room. The gantry system, however, is a daughter system of the fixed, and may rotate relative to it. Both systems share a common y-axis, pointing toward the virtual gantry bearing, around which the gantry system rotates. The z-axis of the fixed system points upward, and the x-axis is perpendicular to them both. When the gantry angle is equal to zero, the two systems overlap[39]. The treatment room systems are illustrated in Figure 3.12.

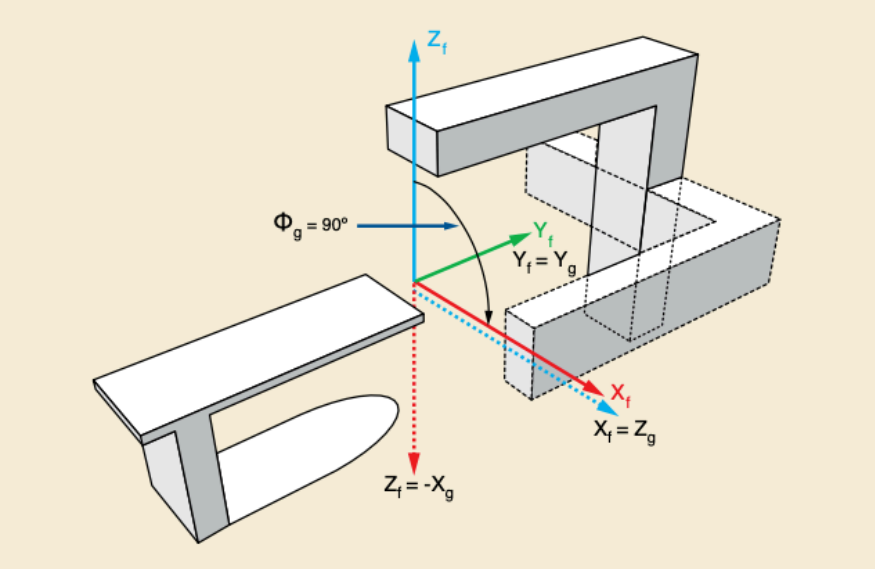

Figure 3.12: The fixed and gantry coordinate systems. Taken from [39].

The patient coordinate system is defined as having the positive x-axis toward the left arm of the patient, the positive y-axis toward the head and the positive z-axis pointing up out of the chest of the patient. This means the coordinate system will depend on the orientation of the patient. For an HFS patient, the patient coordinate system overlaps with the fixed system of the treatment room. The patient coordinate system is illustrated in Figure 3.13.

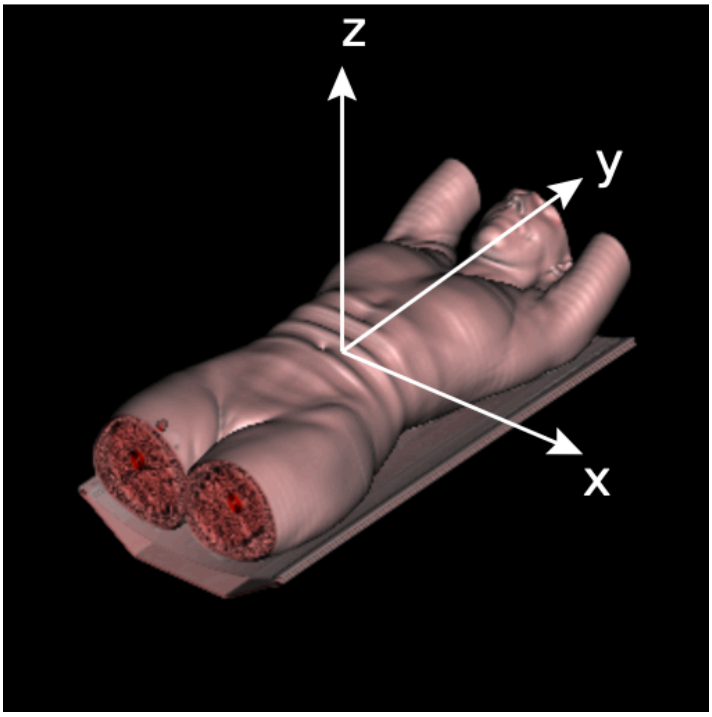

Figure 3.13: The patient coordinate system. Taken from [40].

3.6 DICOM

Particle therapy has a lot of steps, from imaging to delineation to planning to treatment, which need to be able to move information between them. The standard format for storing medical imaging information and data in medicine is the Digital Imaging and Communications in Medicine (DICOM) file format [39]. Such files allow for the storing of images, along with relevant information about the patient in question. There are different types of DICOM, some of which are being used to store information about structures delineated by a physician, while others can be used to store treatment plans. DICOM files can be an absolute necessity when setting up a simulation environment.

DICOM files use the DICOM standard coordinate system. This coordinate system is patient-based, with the positive x-axis defined as pointing toward the left arm, the positive y-axis pointing out of the back of the patient, and the positive z-axis pointing up through the head. Correctly transforming between this coordinate system and those explained in the previous section is of great importance when setting up a simulation.

DICOM files group information into data sets, similar to dictionaries in Python. A DICOM file consists of elements, such as the name of the patient or the energy of the beam, which are paired together with a unique tag. These tags are used to retrieve the DICOM elements.

The different types of DICOM files are identified by their unique ID tag. The scanned images of the patient are stored in RT Image files, with each file corresponding to a slice from the CT scan. Examples of what each file contains include information about the patient position and orientation, the dimensions of the image, as well as density information about the patient. The latter is retrieved from a two-dimensional array containing the various HU values of the image. While these types of DICOMs contain the actual images of the patient, the structures delineated by a physician are stored in a different type of DICOM.

The RT Structure Set is a type of DICOM in which the information about the various ROIs is stored. This includes the coordinates and borders of the various organs, the GTVs, CTVs and PTVs, as well as the body itself. These files are necessary when creating DVHs, in addition to being useful when plotting and evaluating the dose distribution. Only one such file is needed per patient.

The RT Dose files contain the dosimetric information. This includes the dose distribution as calculated by the TPS, with all relevant details. One RT Dose file is made for each field, although these can be combined into one file. The dose information is stored similarly to how the image files stores density information, except for being three-dimensional. The dose files also contain information about the scoring region and grid size. These DICOMs are useful for comparing delivered or recalculated dose distributions with those of the TPS.

The RT Plan file contains information about the treatment plan itself, as defined by the TPS. Only one file is needed per treatment plan, and it is from this file essential data needed for the beamline setup is retrieved. This includes information about the particle beam, the angles of the gantry and treatment table, the various fields used, isocenter of the target volume, and devices used to manipulate the beam [39].

3.7 Monte Carlo

Monte Carlo (MC) simulations are the most accurate methods of simulating particle interactions due to the way the underlying physics are modeled. In an MC simulation, the interactions of particles can be simulated on a particle-to-particle basis. MC makes use of theoretical models and parametrization, as well as experimental data for electromagnetic and nuclear interactions. The knowledge of the trajectory, interactions and energy deposition of one particle, including potential secondaries, is called the particle's *history*. The particles are simulated in a well-defined geometry, step-by-step, using cross-section data, which gives the probability of a given interaction, and sampling from a random number generator. The size of the steps between which the particles are measured should be small, as this minimizes the difference in the size of cross-sections at the beginning and the end of a step. Choosing a smaller step size does, however, increase the computation time [12].

Due to the stochastic nature of the processes involved, a great number of particles need to be simulated in order to minimize the uncertainty of the results. Uncertainty in MC depends on the amount of histories tracked (N), with the error being proportional to $1/\sqrt{\mathrm{N}}$. Increasing the number of histories will also increase the amount of computation time needed, which makes MC inefficient for use in the clinic [12].

Several different types of MC codes are used in proton therapy, such as Geant4 [41, 42], TOPAS [43] and FLUKA [14, 15] – the latter of which was used in this project. Setting up an MC simulation requires the entire environment to be defined, which includes the particles that are to be tracked, the entire tracking geometry, the physical processes governing the various interactions, the manner in which the particles are to be tracked and how the simulated data is to be handled and recorded. Setting up an MC simulation requires information about the particle beam and the geometry and composition of the treatment nozzle, as well as clinical information about the patient [12].

3.8 FLUKA

FLUKA is a highly accurate, general-purpose tool used for calculating how particles propagate and interact with matter. It can simulate about 60 different types of particles from 1 keV up to

several TeV, and even higher for certain particles. It supports complex geometries and comes with its own graphical user interface, called Flair [44]. While FLUKA requires little programming knowledge for most tasks, the user does need to create an input file in order to run a simulation. While such files can be made directly in Flair, it is not unusual to create them beforehand, for example using a script, and later importing them into Flair [14].

The information needed for the input file depends on the type of simulation desired. The input files themselves are ASCII text files consisting of a sequence of option lines ("cards"), which all follow the same structure by default. These cards contain information such as documentation in the form of comments and titles, beam characteristics, geometry and material definitions, which quantities are to be scored and how many histories are to be run.

Although there are strict rules as to the alignment and amount of characters allowed in a card, increased flexibility can be achieved as Flair comes bundled with a preprocessor. This makes it possible to add conditionals and parametric expressions to the input file. Cards which include such expressions do, however, still need to follow the FLUKA input format [14].

3.9 The IBA Universal Nozzle

The PS patients whose treatment plans were recalculated in this project were originally treated with the IBA Universal Nozzle system, so named as it allows for a variety of treatment modalities. The double-scattering mode of the system was used for treating the PS patients in this project. The first upstream component in the nozzle is an ionization chamber for monitoring the beam properties, followed by the first scatterer, which consists of a configuration of up to eight scattering foils made of lead or aluminium. These foils, which vary in thickness, are inserted independently depending on the required scattering compensation. The thickness of the first scatterer is chosen so as to reduce the change of scattering power in the downstream range modulator and second scatterer, which varies depending on the beam energy. Range modulation in the IBA nozzle is achieved using one of three RM wheels, each of which consists of three range modulator tracks, in conjunction with BCM. The steps of the RM wheels are scatter compensated in order to decrease the change in scattering power associated with a varying beam energy. Downstream of the RM wheel, using one of three contoured scatterers, the particle beam is spread out into a uniform field with a

diameter of up to 24 cm. Depending on the specific scatterer used, beam ranges from 4.6 to 28.4 g/cm^2 in water can be achieved. The scatterers are made from lead and Lexan, with the latter being added for energy compensation [35]. The range span is divided into eight options, each of which consists of a particular combination of first and second scatterers, as well as a specific RM wheel track. Each of these options are further divided into suboptions, for which a particular BCM is custom designed [29]. Downstream of the contoured scatterer a variable collimator blocks parts of the beam from entering the subsequent beamline components, followed by a second ionization chamber used for beam monitoring. Beyond this point, one of three retractable snouts are mounted, in which the aperture and compensator is located. The snout, the choice of which depends on the required field size, collimates the beam outside of the aperture [35].

4. Methods

The aim of this project was to simulate the two main treatment modalities in proton therapy, and see whether or not a variable RBE, which takes LET_d into account, will affect the dosimetric benefits of PBS over PS. In addition to comparing the two modalities to one another, it was also desirable to compare the dose distributions calculated by the Eclipse TPS and the MC code FLUKA [14, 15] (v2011.2x). This was done using anonymized treatment plans made for patients previously treated with PS, as well as newly created PBS treatment plans for the same patients. The PS patients were originally treated with the IBA Universal Nozzle at the University of Florida. While an inhouse script could be used to set up the PBS simulation environment, a script for the automated creation of PS input files in FLUKA had to be created by the author of this thesis. This was done using the Python (v2.7) programming language along with the Pydicom (v0.9.9) library. The manner in which the script uses data extracted from the DICOMs of a given patient to define the specific simulation is described in this chapter.

Once run, the results of the FLUKA simulations were extracted and converted to DICOMs using an inhouse script for the conversion. Results for both a constant and a variable RBE were obtained for both modalities. The dosimetric indices and dose distributions could then be compared, not only between the two modalities, but also between the TPS and FLUKA.

Dose distributions were recalculated for 3 pediatric posterior fossa tumor patients previously treated with PS. Due to the increased healthy tissue sparing provided by proton therapy compared to photon therapy, the former modality has been increasingly used to treat brain tumors in children. While this has been suggested to lead to a lower rate of both physical and cognitive secondary malignancies, brainstem necrosis has been reported as a potential consequence of using proton therapy to treat brain tumors [45]. All patients in this project were prescribed a dose of 54 Gy, as well as dose constraints of $D50 < 54$ Gy and $D1CC < 56.1$ Gy for the brainstem and brainstem core, respectively. All patients were treated using three treatment fields. The dose distributions were obtained using a fixed RBE of 1.1, as well as a variable RBE calculated using the McNamara model. LET_d- and variable RBE-distributions were also calculated, with the former being used to calculate the latter. Additionally, the recalculated dose distributions were compared with those calculated by the Eclipse TPS. As

can be seen from equation 2.10, the α- and β-values for both the reference radiation and the proton beam is required in order to obtain the variable RBE. The α_x /β_x-ratio used was 2 Gy, as this represents the late responding tissue found in the central nervous system [46]. This ratio was chosen as the dose delivered to various OARs, specifically the brainstem and the brainstem core, was of interest in this project. The α/β-values for the proton beam were found through equations 2.11 and 2.12, with the LET_d-values being those calculated by FLUKA.

4.1 Setting Up the Simulation

4.1.1 Standard Input File and Settings

The following is included in a standard input file, according to the FLUKA manual [14]:

- Title and comments for documentation purposes
- Definition of the problem geometry
- Definition of the materials and material assignments
- Definition of the particle source
- Definition of requested scoring quantity and method
- Definition of biasing schemes
- Definition of problem settings such as step size, energy cutoffs or physical settings not simulated by default.
- Initialization of the random number sequence
- Starting signal and number of requested histories.

FLUKA has several default physics settings, which can be accessed using the DEFAULTS card, which are suitable for various kinds of problems. The HADROTHErapy DEFAULTS card was used in this project, as it is optimized for hadron therapy.

The settings for this card are also outlined in the FLUKA manual, and include:

- Transport of electrons, positrons and photons is activated
- Inelastic form factor corrections to Compton scattering and Compton profiles activated

- Low-energy (including thermal) neutron transport is activated
- Fully analogue absorption for low-energy neutrons
- Particle transport threshold set at 100 keV, except for neutrons (1×10^{-5} eV)
- Multiple scattering threshold at minimum allowed energy, for both primary and secondary charged particles
- Delta ray production on with threshold 100 keV
- Restricted ionization fluctuations on, for both hadrons/muons and EM particles
- Tabulation ratio for hadron/muon dp/dx set at 1.03, fraction of the kinetic energy to be lost in a step set at 0.02

4.1.2 Importing the Patient

The patient geometry must be included in the simulation. In FLUKA, a convenient way to describe complex geometries is in terms of *voxels*, i.e. three-dimensional grids consisting of small, identical parallelepipeds. Each voxel contains density and material information, together forming a complete picture of the larger geometry. The voxels describing the patient geometry is stored in a voxel file (.vxl), which can be created in Flair. The CT DICOMs can be imported directly into Flair, and the HU numbers of the images can then be translated into material/density information using an algorithm defined by the user. An inhouse algorithm was used for this purpose in this project. Once created, the voxel file can be included in the VOXEL card of the input file, which also allows for the translation of the patient.

It was desirable to place the isocenter of the target volume at the origin of the FLUKA coordinate system. The origin of the DICOM coordinate system depends on the scanner used, meaning the origin and isocenter does not necessarily overlap, as was the case in this project.

The Image DICOMs contain the coordinates of the upper left-hand corner of the images (stored under the “Image Position” tag), while the Plan DICOMs contains the coordinates of the target isocenter (“Isocenter Position”). Using these values, the isocenter can be moved towards the origin. It will, however, still be a bit off. In FLUKA, coordinates mark the *corners* of the voxels, while in the DICOM system, coordinates mark the *center* of the voxels. This would result in an isocenter offset of half a voxel. The Image files contain the spacing between the voxels in the xy-plane (“Pixel Spacing”), as well as in the z-direction (“Slice Thickness”).

From these values, a correct translation of the patient was achieved using the following equations [40]:

$$x_{trans} = \frac{x_{image} - x_{iso} - \frac{x_{pixel}}{2}}{10}$$

$$y_{trans} = \frac{y_{image} - y_{iso} - \frac{y_{pixel}}{2}}{10} \tag{4.1}$$

$$z_{trans} = \frac{z_{image} - z_{iso} - \frac{z_{slice}}{2}}{10}$$

Where the subscript "trans" refers to the translation, "image" refers to the image position, "iso" refers to the isocenter position, "pixel" refers to the pixel spacing, and "slice" refers to the slice thickness. The division by 10 is due to the fact that FLUKAs standard unit of distance is centimeter, whereas DICOM uses millimeter.

4.1.3 The Particle Beam

The particle beam energy is located in the Plan DICOMs, specifically under the "Nominal Beam Energy" tag. The BEAM card holds information about the particle beam itself, such as the energy, the type of radiation (here "proton"), as well as the divergence of the beam in the x-, y- and z-direction. Before being added, the energy had to be transformed from MeV to GeV, as the former is the DICOM standard while the latter is the FLUKA standard. Additionally, for PS, the beam energy had to be calibrated somewhat, with a correction factor that depended on the IBA nozzle option chosen. The correction factor, found inhouse, was necessary because of an offset in the pristine Bragg peaks calculated by the TPS and FLUKA.

In the case of PBS, where the beam energy changes during treatment, a variety of beam energies are present, corresponding to the different spot positions used during treatment. These were extracted and added to the user-defined routine described in the next section. The maximum beam energy was, however, added to the BEAM card, as is recommended by the FLUKA manual.

For PS, a BEAMPOSit card was added below the BEAM card. This card defines the coordinates of the center of the beam spot, as well as its direction. The center was placed at the origin of the XY-plane, but far down the negative z-axis with the direction pointing in the positive z-direction. This places the beam upstream of all beamline geometry. The handling of the PBS beam direction is explained in section 4.1.5.

4.1.4 Source Routine

Complicated simulation environments, such as the ones described in this project, requires user-defined routines. Such routines are included in FLUKA by adding a SOURCE card. This card tells FLUKA that it is to use a user-defined source routine to sample the primary particles.

The source routine is written based on certain patient and treatment specific parameters, making them different for the two modalities. In the case of PS, creation of the source file requires information about the RM wheel used, as well as the BCM, both of which change during treatment. Both of these values can be obtained from the Plan DICOMs, found under the “Range Modulator ID” and the “Beam Current Modulation ID” tags, respectively. The latter does not give the BCM value directly, however, but rather a specific nozzle option, from which the required BCM could be obtained.

For PBS, the source file had to include information about the patient position and the energies used, the location of which is explained above, as well as the angle of irradiation, i.e. the gantry angle. Additionally, several parameters which describe the beam spots used in scanning were needed, all of which were obtained from the Plan DICOMs. The required beam spot parameters are described below:

- The x- and y-coordinates of the scanning spots, as projected onto the machine isocentric plane in the IEC Gantry system. The scan spot positions are found under the “Scan Spot Position Map” tag.
- A set of meterset weights corresponding to scan spot positions. The order of the weights matches the positions of the scanning spot positions. These weights are found under the “Scan Spot Meterset Weights” tag.
- The scanning spot size, specified by a numeric pair, as calculated using the Full Width Half Maximum (FWHM). The spot size is measured in air in the x- and y-direction at

the isocenter of the IEC Gantry system. This parameter is stored under the "Scanning Spot Size" tag.

In this project, inhouse source files, written in Fortran 77, were used for this purpose, after first being modified according to the chosen treatment modality and its specific parameters.

4.1.5 The Beam Direction

In radiation therapy, the various angles of irradiation are achieved by rotating the gantry system around the treatment table, which can also be rotated. Additionally, the orientation of the patient can be changed. The gantry angle is found in the Plan DICOMs under the "GantryAngle" tag. The three different parameters which describe the angles of the treatment turntable can also be obtained from this DICOM. These three angles, which make up the patient support coordinate system, are the patient support angle (stored under the "Patient Support Angle" tag), the tabletop pitch angle ("Table Top Pitch Angle") and the tabletop roll angle ("Table Top Roll Angle"). The patient support angle was the only one of these relevant for this project and it describes the table rotation about the z-axis in the IEC Fixed coordinate system. This is illustrated in Figure 4.1.

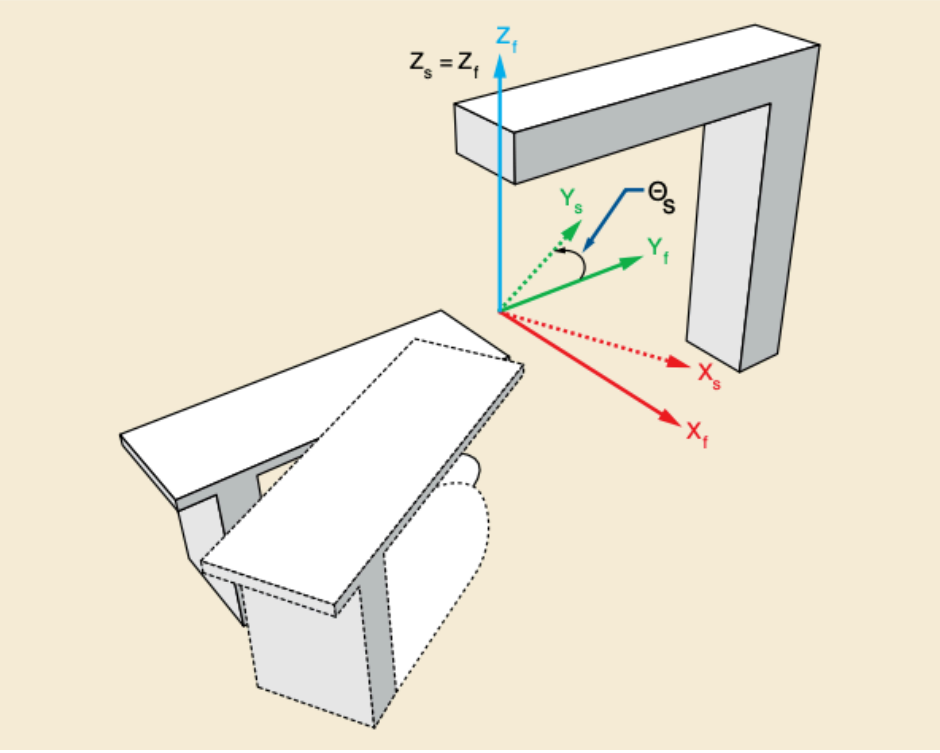

Figure 4.1: The patient support coordinate system. Taken from [39].

Simulating the angles of irradiation was handled differently for the two modalities. As mentioned in section 4.1.3, a BEAMPOS card was not used to define the origin or direction for the PBS modality. Instead, this was done by changing parameters within the SOURCE routine, specifically the TXFLK and TYFLK parameters[40]. These describe the direction cosines of the beam with respect to the x- and y-axis in the FLUKA coordinate system, respectively, and can be calculated using simple trigonometry and the necessary angles obtained from the DICOMs.

For PS, on the other hand, the beamline was kept stationary with the patient being rotated. This was done by extracting the gantry and patient angles and adding them to ROT-DEFIni cards. Such cards define the rotations and translations that are to be applied to geometry or *binnings* (see section 4.1.7). The ROT-DEFI cards needs to be assigned an axis of rotation, the translation in the x-, y- and z-directions (if so desired), as well as the polar and azimuthal angles of rotation. Complex transformations can be split up into several consecutive cards for simplicity. Before the patient could be rotated relative to the beamline, they had to be correctly aligned within the FLUKA coordinate system. With the target volume already placed at the isocenter, this was achieved with a ROT-DEFI card with an azimuthal and polar rotation of 180º and 270º, respectively. Both rotations were done with respect to the FLUKA x-axis, placing the patient in the HFS position relative to the beamline. Once this was achieved, the patient support and gantry angles were added as polar rotations with respect to the FLUKA z- and y-axis, respectively.

4.1.6 Geometry

The PBS beam does not move through any beam shaping elements. Instead, magnets are used to scan the beam across the target, with the energy of the beam being adjusted as required. As explained above, the SOURCE routine handles this during the simulation, changing the beam energy and direction as required. The steering magnets were therefore not included in the simulation environment, and the only geometric figure present for this modality was therefore the patient.

PS, on the other hand, required the entire beamline to be defined. In FLUKA, complex geometries can be created from simple geometric figures which must be assigned a specific material. The non-patient specific beamline components (i.e. everything except the aperture

and compensator) could be defined in their own files, provided they follow the FLUKA input format. The components required for the simulation could then be imported by the input file using the #include-directive in Flair. Inhouse geometric definitions based on the IBA Nozzle blueprints were used in this project. While some geometric structures were the same for all patient setups (i.e. the ionization chambers and a field mirror used for beam monitoring), some depended on patient specific information stored in the Plan DICOMs. The components that could be directly obtained from these were the RM wheel ("Range Modulator ID"), the snout ("Snout ID") and the second scatterer, which is stored under the "Lateral Spreading Device ID" tag. For range modulation, knowing which RM wheel is used is not enough. As explained in chapter 3, the entire wheel is not necessarily to be irradiated, depending on the desired modulation width. The stop angle of a given field, i.e. the angle beyond which the wheel is not to be irradiated, depends on both the modulation width and the nozzle option. The various stop angles were obtained using the following equations:

$$SA_1 = a_0 + Ma_1 + M^2a_2 + M^3a_3 + M^4a_4$$

$$SA_2 = \min(int(SA_1 * 0.71111 + 0.5), 255) \tag{4.2}$$

$$SA = SA_2/0.71111$$

where a_0-a_4 are option dependent coefficients, M is the modulation width, min() returns the lowest of the values contained within its parentheses and int() returns the numeric value within its parentheses as an integer. The tag under which the second scatterer is found is actually a daughter tag of the "Lateral Spreading Device Sequence" tag. This tag is split into several elements, each of which correspond to a specific scattering device. In this project, only the name of the second scatterer was stored in the DICOMs, meaning the first scatterer configuration had to be found another way. The theoretical thickness of the first scatterer was obtained using the following equation:

$$FS_T = a_0 + a_1R + a_2R \tag{4.3}$$

where a_0-a_2 are option dependent coefficients and R is the range of the proton beam. Once the theoretical thickness had been acquired, the first scatterer configuration could be found by iteratively.

Which variable collimator to be used is obtained indirectly from the Plan DICOMs, as it solely depends on the nozzle option. The aperture and the compensator had to be created for each individual treatment field. Information about both the aperture and the compensator is contained within the Plan DICOMs, specifically under the "Ion Block Sequence" and the "Ion Range Compensator Sequence" tags, respectively. A slightly modified inhouse script using the information stored under these tags, as well as the "Snout ID", was used to generate these structures.

4.1.7 Scoring

The scoring in FLUKA was done using USRBIN cards, which allow for the scoring of several different quantities using a *binning* detector. A binning is a regular spatial mesh, independent from the problem geometry and defined by the user. In addition to defining the dimensions of the scoring grid, the USRBIN card defines the type of particles which are to be tracked and which logical output unit is to be used. In order to make comparisons between the dose calculations, the dose should be scored over the same region for not only the two modalities, but also for the TPS and MC. The parameters describing the TPS grid are all found in the Dose DICOMs. Using these parameters, along with the Isocenter Position obtained from the Plan DICOMs, a scoring grid in FLUKA could be defined. The necessary Dose parameters are listed below:

- The x-, y- and z-coordinates of the upper left-hand corner (center of the first voxel transmitted) of the image, in mm. These coordinates are stored under the "Image Position (Patient)" tag.
- The physical distance in the patient between the center of each pixel in mm, specified by a numeric pair. Stored under the "Pixel Spacing" tag.
- The nominal slice thickness in mm. Stored under the "Slice Thickness" tag.
- The number of bins in the x-, y- and z-direction. Stored under the "Columns", "Rows" and "Number of Frames" tags, respectively.

Using these parameters, the scoring grid can in be defined through equations (4.4) [40]:

$$x_{min} = \frac{x_{image} - x_{iso} - \frac{x_{pixel}}{2}}{10}$$

$$y_{min} = \frac{y_{image} - y_{iso} - \frac{y_{pixel}}{2}}{10}$$

$$z_{min} = \frac{z_{image} - z - \frac{z_{slice}}{2}}{10} \tag{4.4}$$

$$x_{max} = x_{min} + \frac{x_{bins} \times x_{pixel}}{10}$$

$$y_{max} = y_{min} + \frac{y_{bins} \times y_{pixel}}{10}$$

$$z_{max} = z_{min} + \frac{z_{bins} \times z_{slice}}{10}$$

Where the subscript “image” refers to the image position, “pixel” refers to the pixel spacing, “slice” refers to the slice thickness and “bins” refers to the number of bins in the given direction. The division by 10 is again due to the fact that DICOM and FLUKA use different units for distance, while the pixel spacing/slice thickness division by 2 is because they refer to different parts of the voxel.

While the scoring grid now is both correctly placed and defined for the PBS modality, this is not the case for PS. This is due to the fact that when simulating PS, the patient is rotated instead of the beamline geometry. By adding ROT-DEFI cards with the same exact rotation as that used on the patient, the scoring grid gets placed correctly. The rotation is assigned to the scoring grids using a ROTPRBIN card.

Although the above description makes it possible to *place* the scoring grid correctly, it is important to make sure the quantities scored are the same as well, at least if one is to make comparisons between the TPS and FLUKA. While FLUKA allows for the scoring of dose to specific materials, a TPS generally does not. Instead, the algorithms used in such systems tend to score the dose to water. While the ability to score dose over heterogeneous tissue is a strength of MC codes, it makes comparing the two systems more difficult. In FLUKA, the scoring of dose to water can be achieved by adding a user-defined routine, which can be stored in a fluscw.f file. Such routines can be used for weighting particle fluences in a particular medium, from which the dose to water can be calculated. The dose to water is found by

multiplying the measured fluence of charged particles in the medium with the LET in water. This is expressed in equation (4.5) [40]:

$$D_w = \Phi_m \frac{LET_w}{\rho_w} \tag{4.5}$$

where D_w is the dose to water, Φ_m is the charged particle fluence in the given medium, LET_w is the linear energy transfer in water and ρ_w is the water density. External routines, such as fluscw.f, can be added to FLUKA using the USERWEIG card. Several scoring routines can be added to a single fluscw.f file. Which specific routine is chosen for a given USRBIN card will depend on its output unit, which is assigned to the card by the user. Several USRBIN cards can therefore be included in a single simulation. A fluscw.f file developed inhouse was used in this project.

4.1.8 Random Seed and Starting

Before the simulation could be run, a random seed had to be added to the input file. Such seeds, which are placed in a RANDOMIZe card, initialize different and independent random sequences for each input file. The seeds were obtained from the Random module in Python. Making the simulation run requires a START card, which also contains the number of primary histories which are to be simulated. The START card is mandatory and placed at the end of the input file.

4.2 Generating the Results

4.2.1 Scoring Cards

Using the methods described above, a simulation environment for both proton therapy modalities were defined. The simulations were run using 300 million particles per field, and each treatment plan was optimized using SFUD. The fixed- and variable RBE dose distributions of both modalities were scored, as well as the LET_d distributions. This was achieved by adding three USRBIN cards to the input files. The scored quantities are listed below:

- Unit 50: The dose to water deposited by all particles

- Unit 40: The dose to water deposited only by protons
- Unit 41: The dose to water deposited by protons, multiplied with the electronic stopping power of the protons, i.e. the unrestricted LET.

With the chosen output units corresponding to specific scoring routines in the fluscw.f file. From these quantities, the LET_d distribution could be calculated offline using equation (2.8), with unit 41 as the numerator and unit 40 as the denominator. The LET_d could then be further used to calculate the variable RBE weighted dose distribution using the McNamara model.

4.2.2 Data Handling

After the simulations had finished, and the desired quantities had been calculated, the distributions were exported into DICOMs using an inhouse script. Any dose deposited outside of the patient was removed, as the DICOMs generated by the TPS excludes this as well.

Once the results had been extracted, various dosimetric indices of interest were obtained. This was done using the 3D Slicer software (v4.6.2), which is an open-source software platform used for visualization and medical image computing [47-49]. In addition to dosimetric information, the values needed for creating DVHs could also be obtained from Slicer. DVHs were then made using a slightly modified inhouse script, a script which also allows for the plotting and side-by-side comparison of dose distributions found in Dose DICOMs. The dose distributions found using the Eclipse TPS and FLUKA were all plotted for both PS and PBS, in addition to the LET_d and the RBE distributions of each treatment modality.

The mean and maximum doses delivered to the PTV, the brainstem and the brainstem core were obtained through Slicer. The D05 and D95 values of the PTV were also obtained, as these can be used to assess the dose conformity of a given treatment modality. Additionally, the D50 values of the brainstem and the D1CC value of the brainstem core were obtained in order to assess whether or not the prescribed dose constraints had been met.

5. Results

While the primary aim of this project was to compare the biological dose delivered by the two main proton therapy modalities, achieving this required the creation of a script which sets up the simulation. This was done in conjunction with a larger project in which the aim was to develop a Monte Carlo model of the IBA Universal Nozzle system in FLUKA, which would allow for the recalculation of PS treatment plans.

The results presented in this chapter consists of figures illustrating calculated dose distributions, DVHs showing the dose delivered to various structures of interest as well as dosimetric parameters describing the dose delivery. Three structures are present in each dose plot presented in this chapter, which are the PTV, the brainstem and the brainstem core. Throughout the chapter, “TPS” refers to the Eclipse TPS, “RBE1.1” refers to the FLUKA calculated dose using a fixed RBE of 1.1 and “McNamara” refers to doses calculated using a variable RBE obtained from the McNamara model.

5.1 Comparison of the Dose Estimates by Eclipse and FLUKA

5.1.1 Passive Scattering

Figure 5.1 shows the TPS (left) and RBE1.1 (middle) dose distributions delivered by PS to patient 2. The dose difference distributions are shown in the right-hand panel.

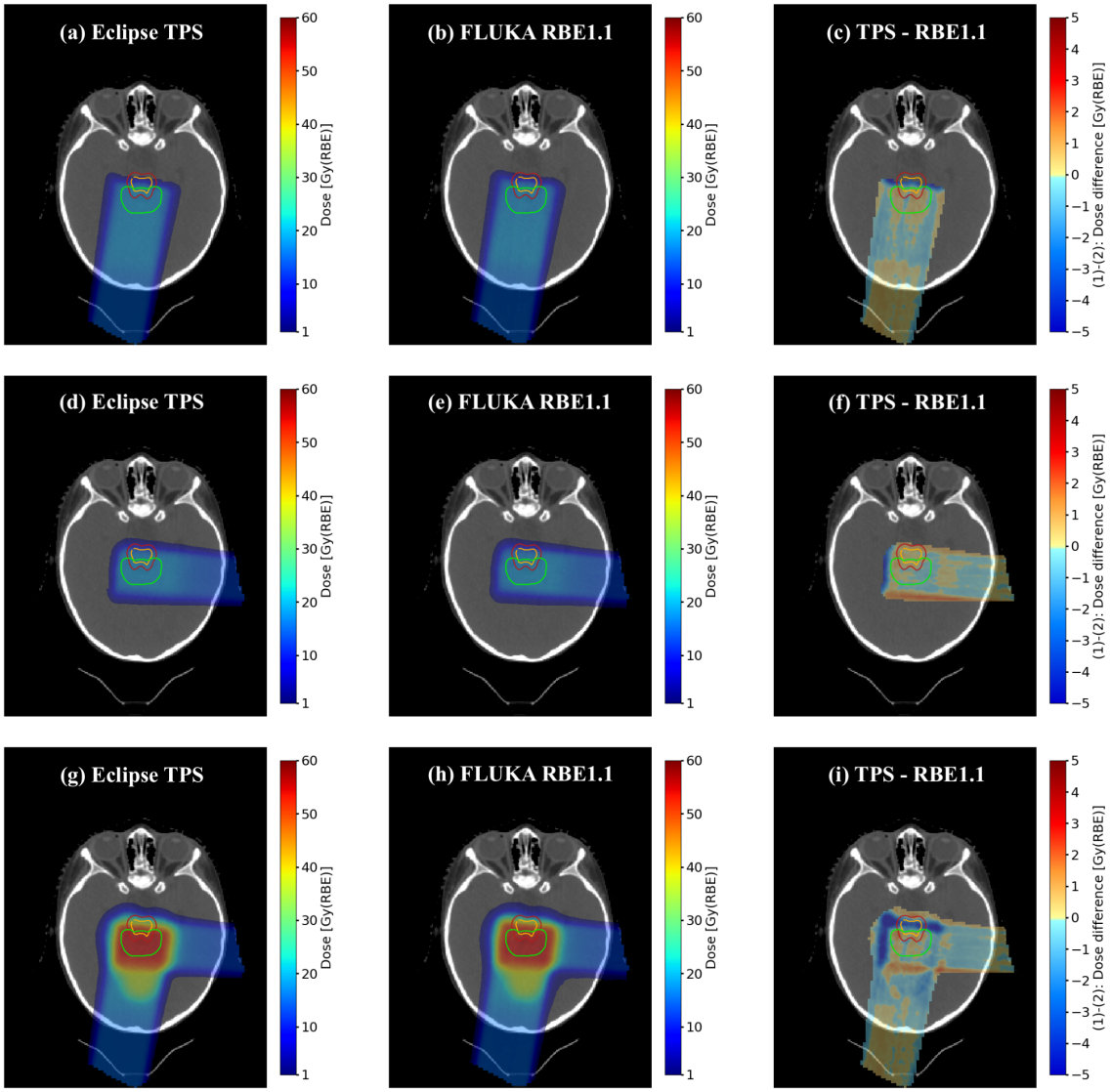

Figure 5.1: PS dose distributions calculated using the Eclipse TPS (left) and FLUKA RBE1.1 (middle) for two single fields, as well as the combined distributions of all three treatment fields. The difference distributions are shown on the right. The PTV is marked with green, the brainstem with red and the brainstem core with orange.

As the figure shows, the differently calculated dose distributions exhibit similar conformity around the target volume, although the difference plots show that there are some differences in dose deposition along the fields. Proximally and within the PTV, the TPS doses are either similar or slightly greater than those calculated by FLUKA. At the distal ends of the fields, however, the doses calculated by FLUKA exceed those calculated by the TPS. As both Figure 5.1c and 5.1i show, a greater dose is calculated within both OARs by FLUKA. The differences

in the dose distributions could indicate the presence of heterogeneous tissue, which would lead to deviations in the particle ranges between the two dose calculation techniques. The TPS and FLUKA RBE1.1 calculated PS doses received by the different structures in patient 2 are shown in the DVH in Figure 5.2.

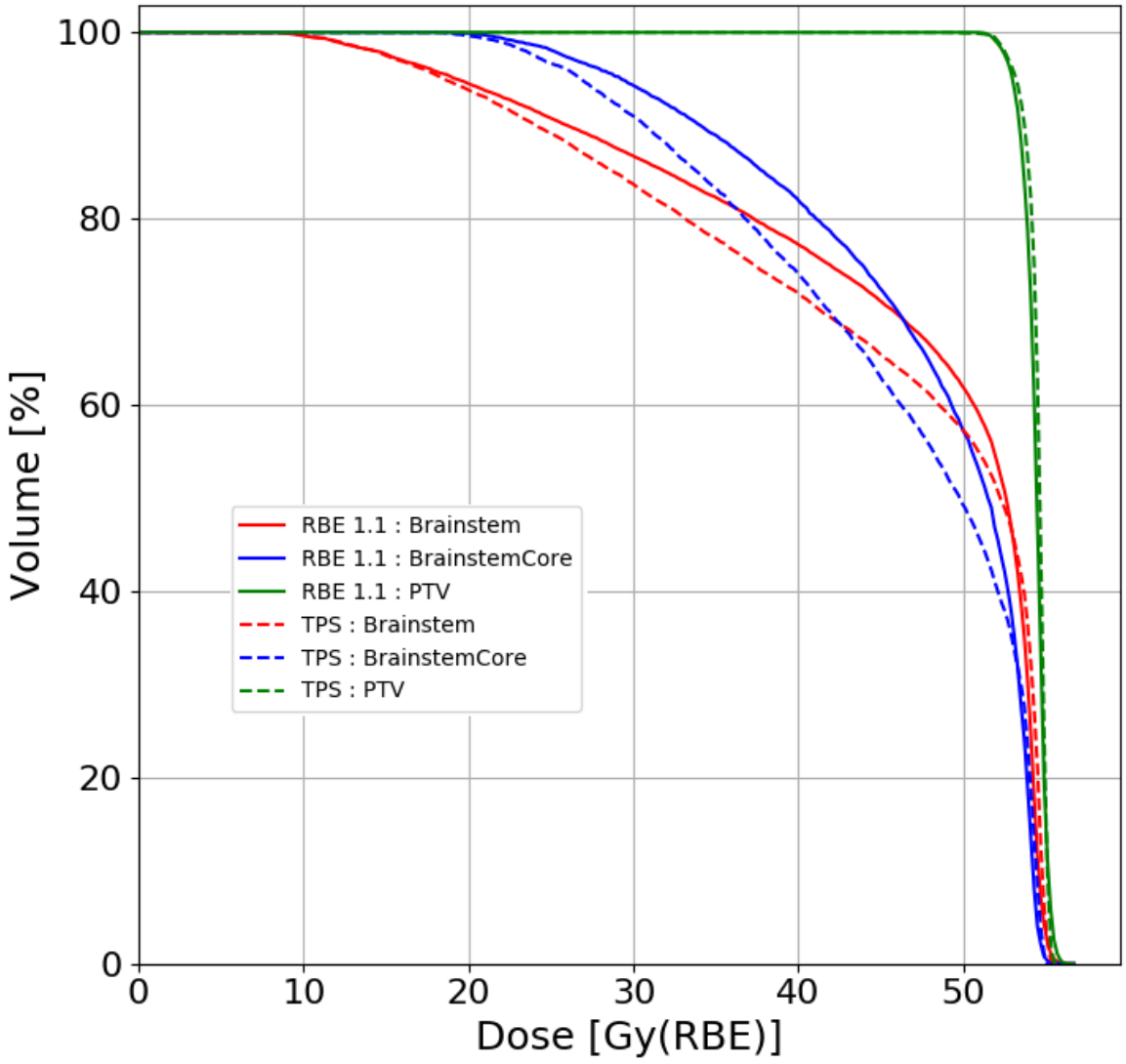

Figure 5.2: Comparison of the PS doses received by the different structures in patient 2 as calculated by the Eclipse TPS (dashed lines) and RBE1.1 (solid lines).

As the figure shows, the dose received by the PTV is very similar for the two dose calculation techniques. As is to be expected from Figure 5.1, the FLUKA curves describing the OARs deviate more than their TPS counterparts. While these curves converge for the doses received by less than 20% of the volumes, the FLUKA curves generally demonstrate a more gradual

decline, although these become steeper as the curves approach one another. The mean and maximum doses delivered to all structures of all patients by PS are shown in Figure 5.3.

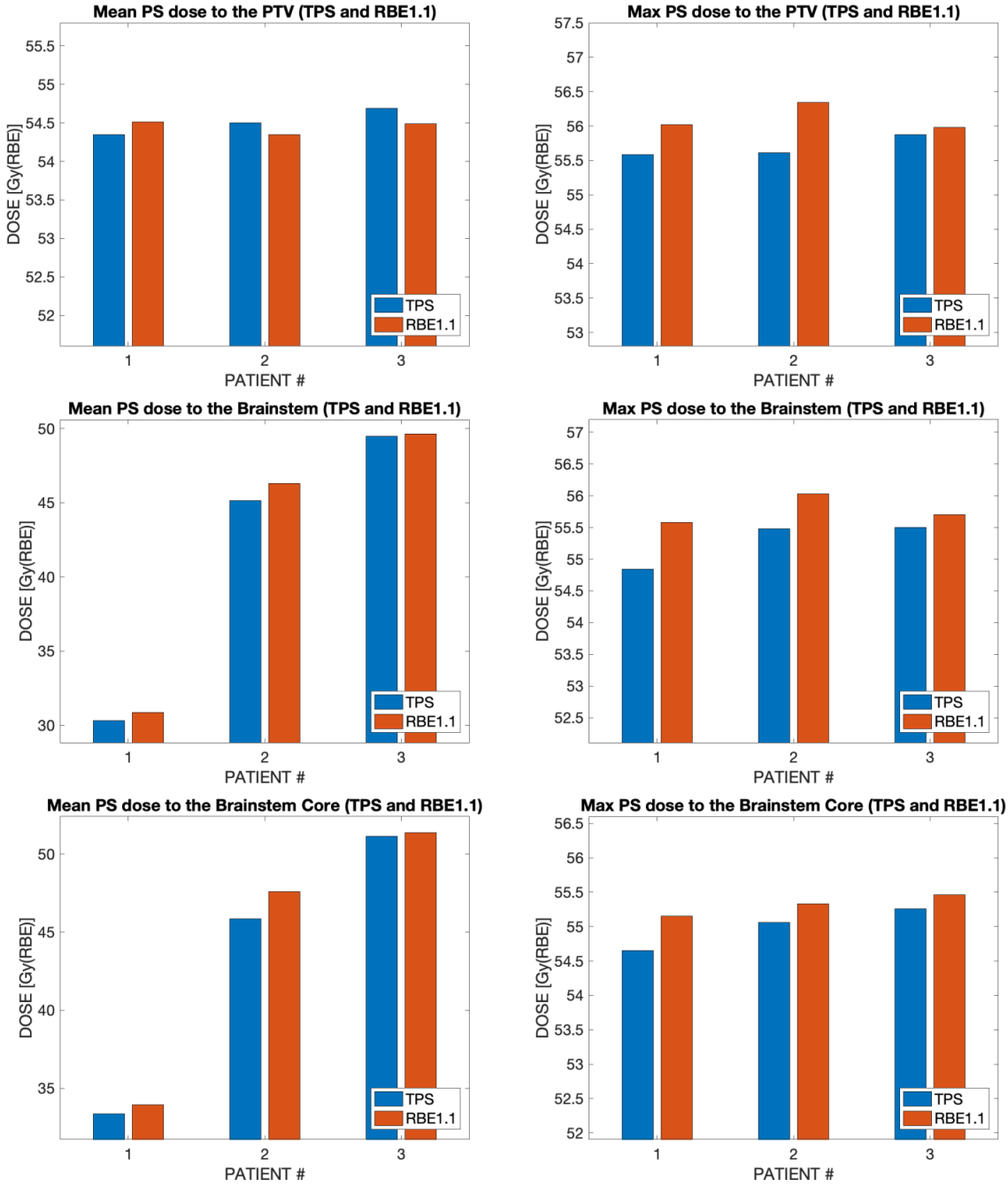

Figure 5.3: The mean and maximum PS doses delivered to the different ROIs calculated using TPS and RBE1.1.

The mean doses delivered to the PTV are similar for the two dose calculation techniques, as is to be expected from Figure 5.2. The FLUKA mean dose is slightly greater than the TPS

dose for patient 1, with the opposite being true for patient 2 and 3. The mean doses calculated by the two techniques are, however, in all cases within 0.5 Gy of each other. The mean doses delivered to the OARs by FLUKA are in all cases greater than the doses delivered by the TPS, although the doses seem similar. The deviation in mean dose to the OARs is greater for patient 2 than for the other patients. The maximum doses calculated by FLUKA are for all patients and structures greater than the doses calculated by the TPS. This deviation is still small, however, and never exceeds 1 Gy.

5.1.2 Pencil Beam Scanning

Figure 5.4 shows the TPS (left) and RBE1.1 (middle) dose distributions delivered by PBS to patient 2. The dose difference distributions are shown in the right-hand panel.

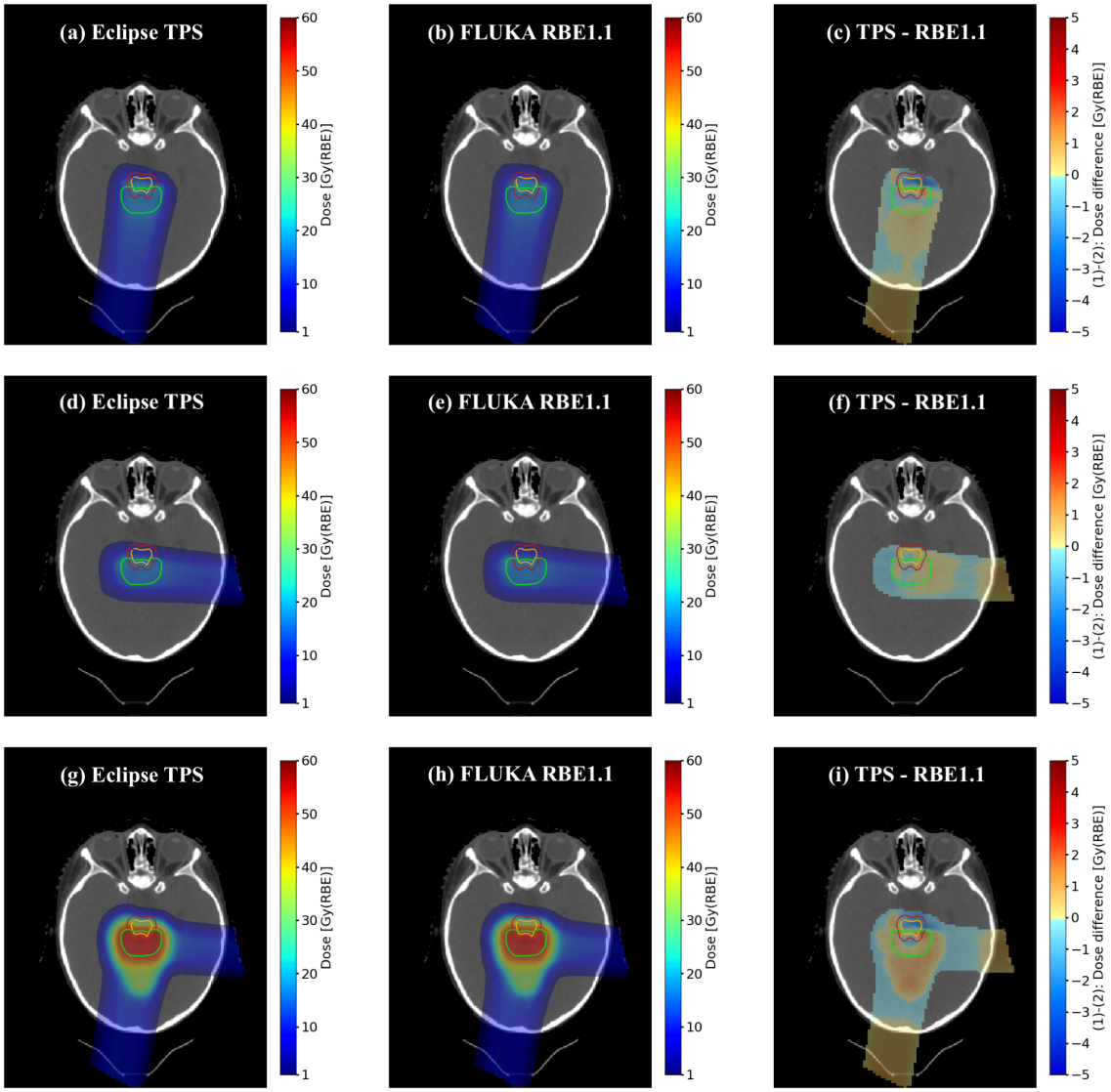

Figure 5.4: PBS dose distributions calculated using the Eclipse TPS (left) and RBE1.1 (middle) for two single fields, as well as the combined distributions of all three treatment fields. The difference distributions are shown on the right. The PTV is marked with green, the brainstem with red and the brainstem core with orange.

As was the case for PS, the differently calculated dose distributions exhibit a similar conformity around the target volume. The difference plots once more demonstrate a similar or greater proximal dose deposition by the TPS, which is also the case inside the target volume. Distally, however, the differences are smaller for this modality. While the difference plot in Figure 5.4f have similar distal dose depositions, an increase in dose delivered by FLUKA is observed distally in Figure 5.4c and 5.4i, a region in which both OARs are located. As with

PS, the differences in the dose distributions is indicative of heterogeneous tissue, affecting the range calculations of the respective dose calculations. The TPS and FLUKA RBE1.1 calculated PBS doses received by the different structures in patient 2 are shown in the DVH in Figure 5.5.

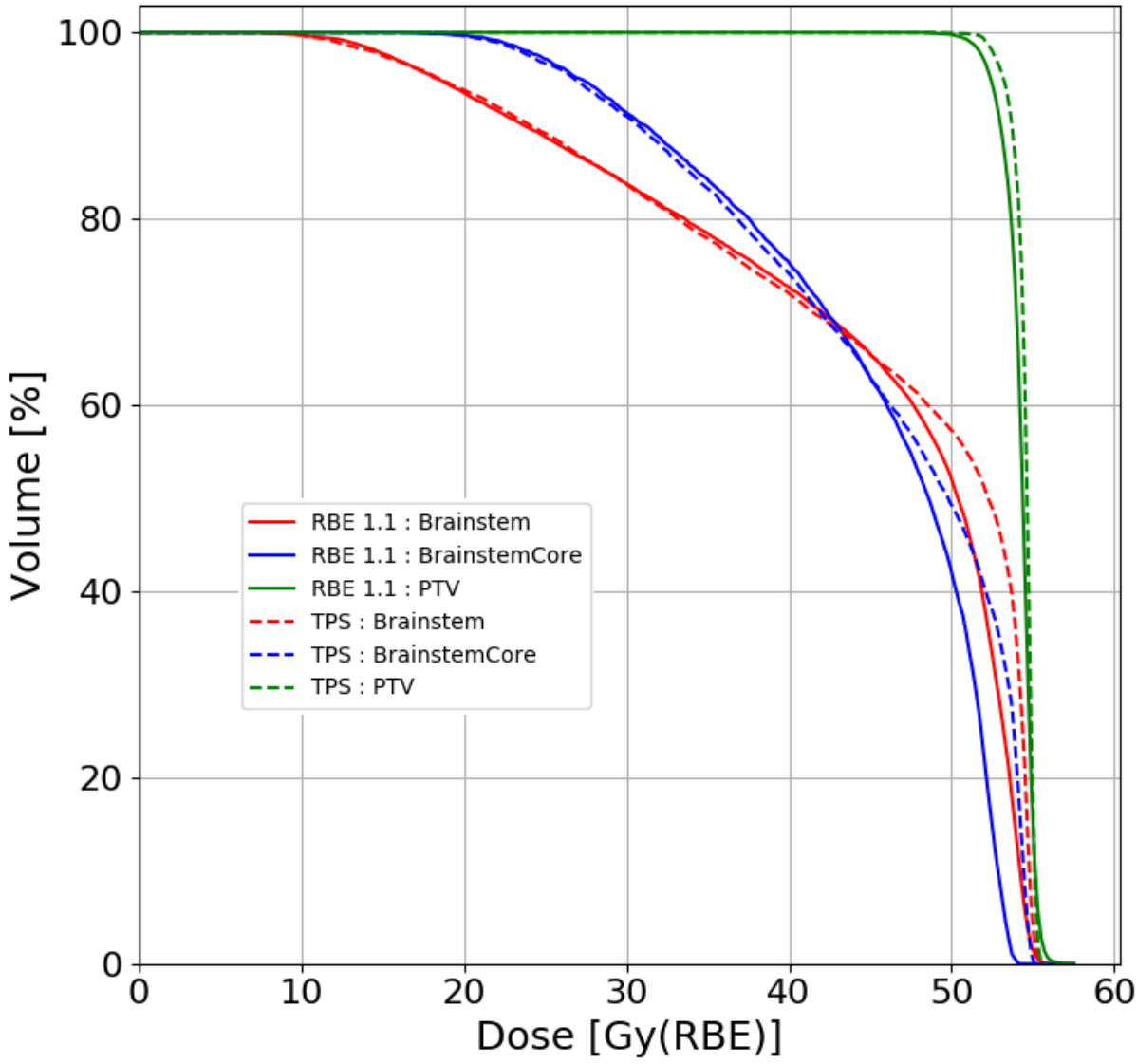

Figure 5.5: Comparison of the PBS doses received by the different structures in patient 2 as calculated by the Eclipse TPS (dashed lines) and RBE1.1 (solid lines).

As the figure shows, the dose coverage of all structures is quite similar for the two techniques. The TPS curve which describes the PTV is slightly greater than its FLUKA counterpart, mainly above doses received by 80% of the volume, below which the curves start to converge.

The curves which describe the OARs, on the other hand, are very similar down to the doses received by 60% of the volume, at which point the TPS curves overtake the FLUKA curves. The resulting divergence is not great, however, and the curves do start to approach their counterparts as the volume percentage decreases, even converging in the case of the brainstem. The mean and maximum doses delivered to all structures of all patients by PBS are shown in Figure 5.6.

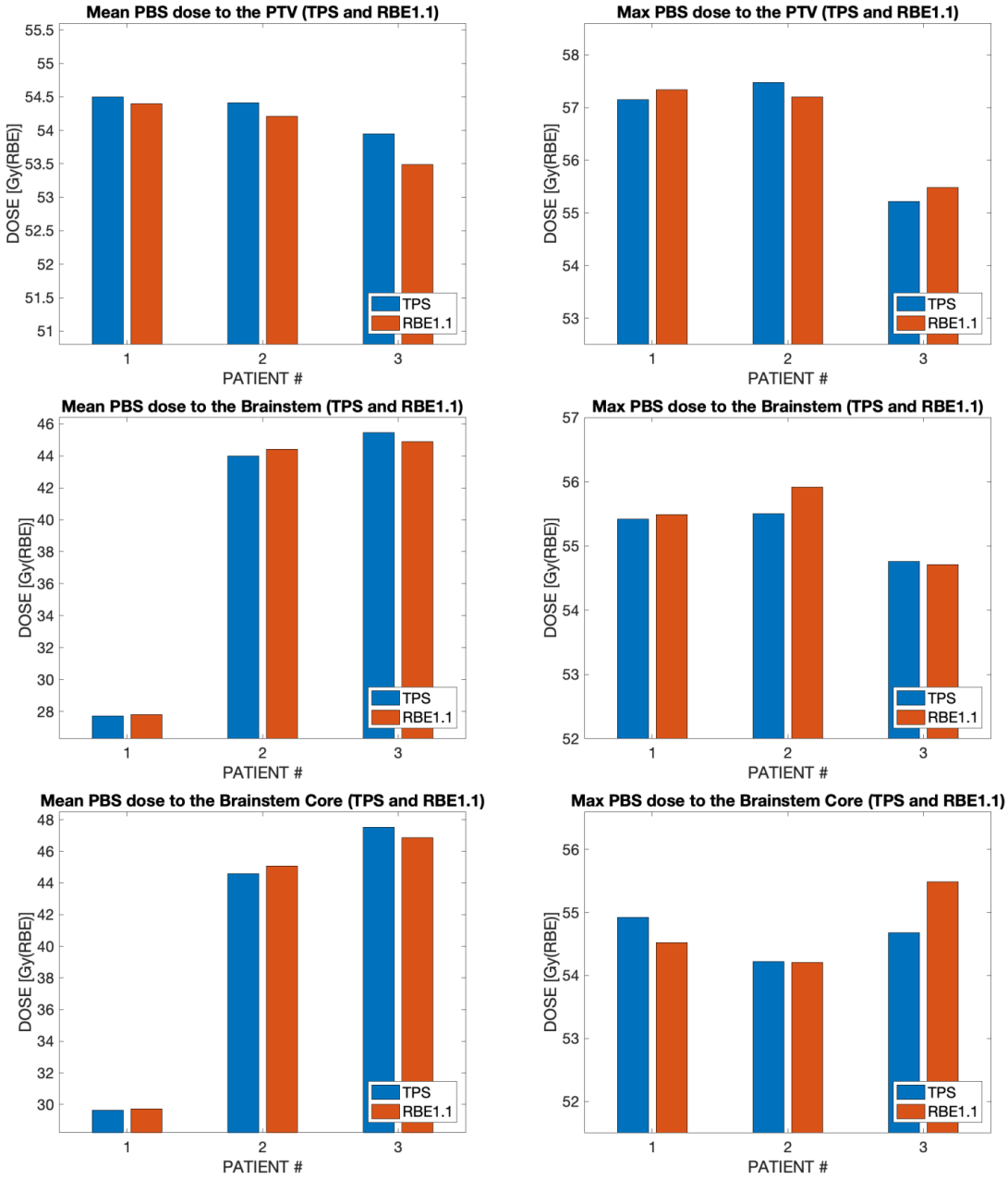

Figure 5.6: The mean and maximum PBS doses delivered to the different ROIs calculated using TPS and RBE1.1.

Both the mean and maximum doses delivered to the ROIs are very similar for the two techniques, with neither showing any significant divergence from the other. However, the TPS calculated mean doses delivered to the PTV are slightly greater than those calculated by FLUKA, which is to be expected from Figure 5.5. All dose deviations between the two techniques are below 1 Gy.

5.2 Comparison of the FLUKA Dose Estimates

5.2.1 Passive Scattering

Figure 5.7 shows the FLUKA dose distributions delivered by PS to patient 2. The McNamara calculated doses are on the left and the fixed RBE1.1 calculated doses are in the middle. The dose difference distributions are shown in the right-hand panel.

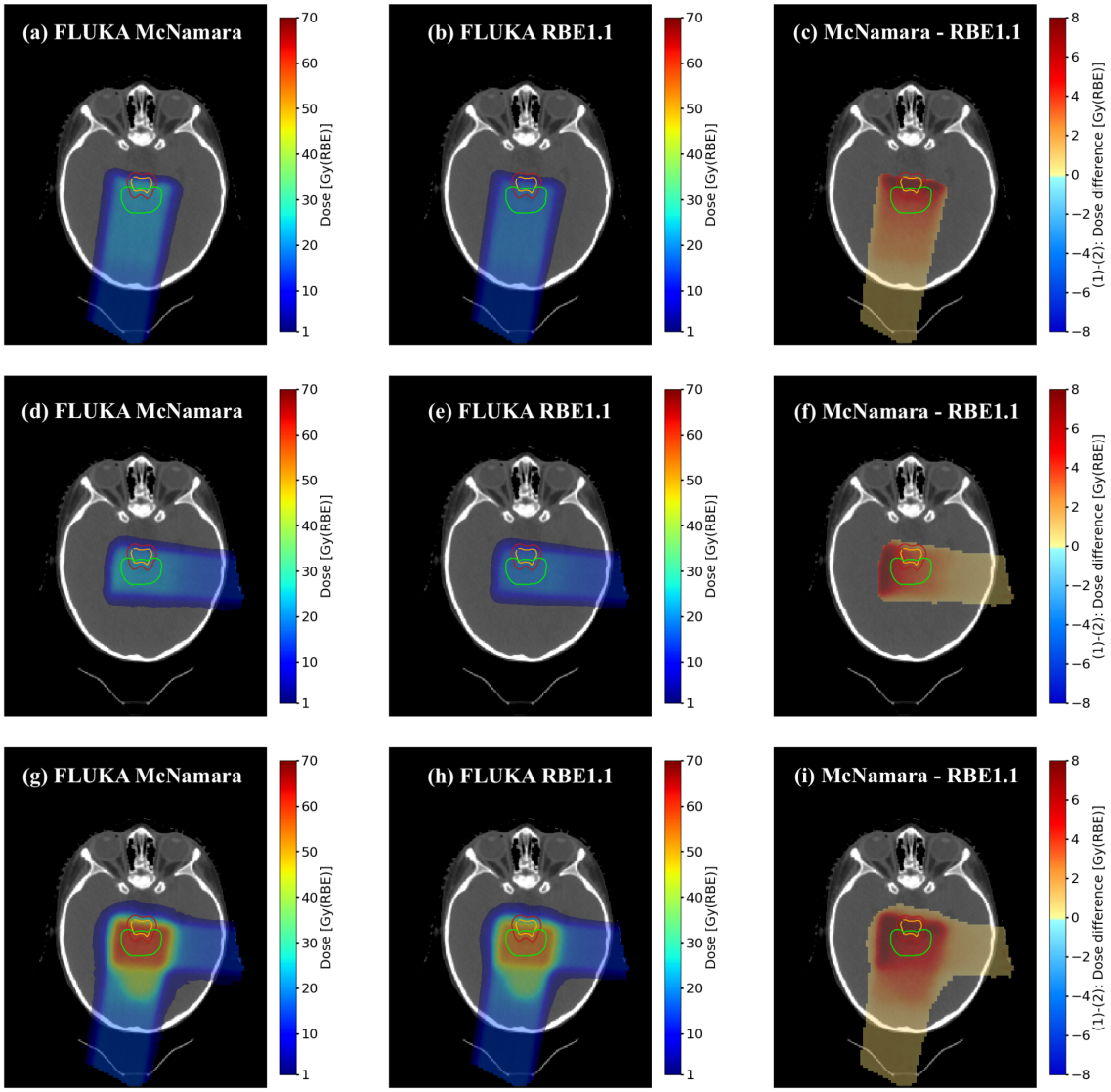

Figure 5.7: PS dose distributions calculated using McNamara (left) and RBE1.1 (middle) for two single fields, as well as the combined distributions of all three treatment fields. The difference distributions are shown on the right. The PTV is marked with green, the brainstem with red and the brainstem core with orange.

As the difference plots show, the doses calculated using McNamara are in all cases greater than those found using a fixed RBE of 1.1. While there is a proximal buildup of increased dose from McNamara, the greatest dose difference is at the distal sides of the target volume. The region of largest dose deposition contains within it both of the OARs. The McNamara and RBE1.1 calculated PS doses received by the different structures in patient 2 are shown in the DVH in Figure 5.8.

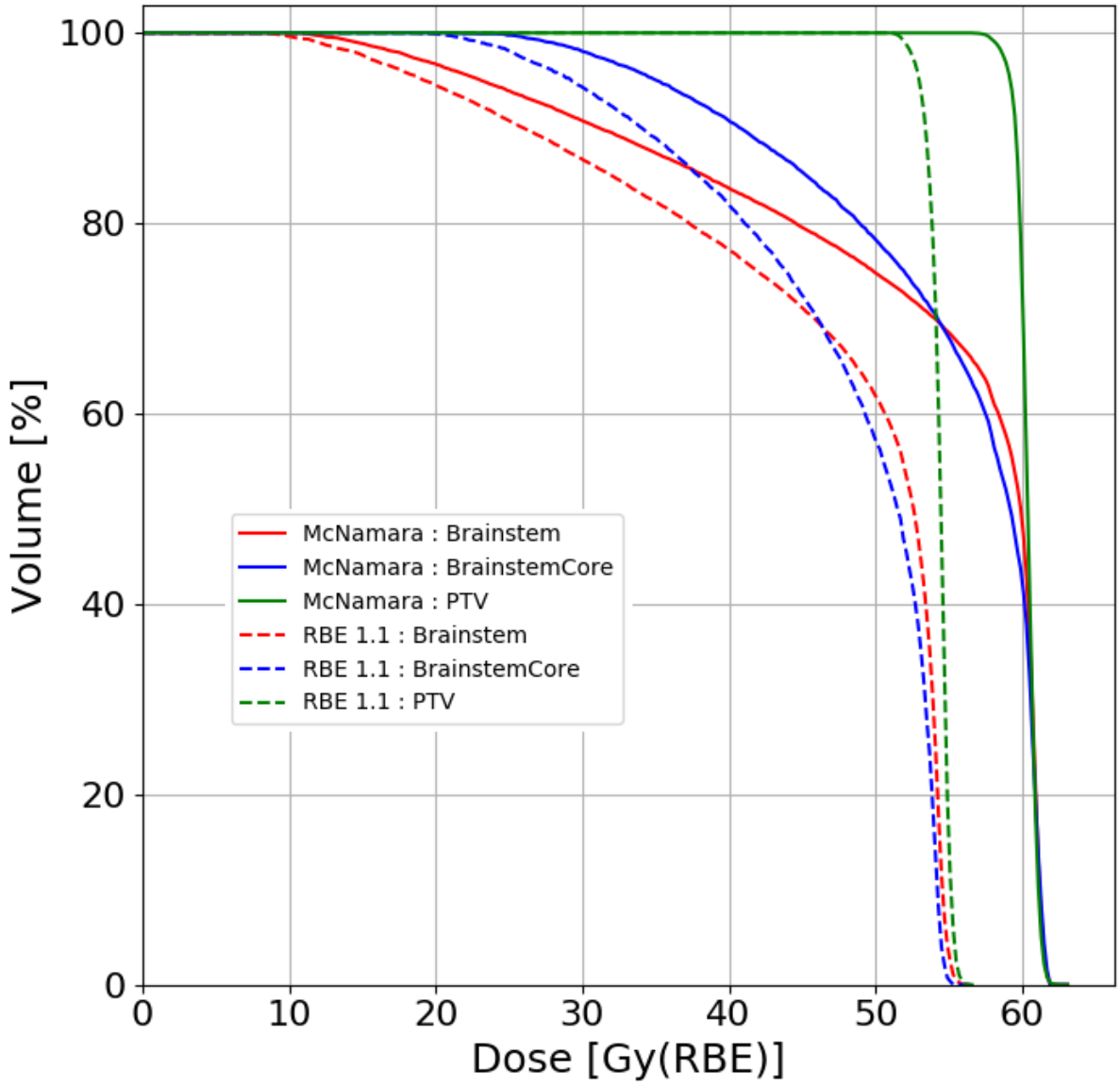

Figure 5.8: Comparison of the PS doses received by the different structures in patient 2 calculated by RBE1.1 (dashed lines) and McNamara (solid lines).

As the figure shows, there is a significant deviation between the two dose calculation techniques. While the curves describing a given structure are quite similar in appearance, the McNamara curves are in all cases greater than those associated with RBE1.1. The McNamara PTV curve appears to deviate in a scaled-up fashion from the RBE1.1 curve and the distance between them is quite constant across the PTV volume. The curves which describe the OARs deviate slightly more. While these curves approach the PTV curve in both cases, the

McNamara curves have a more gradual slope and they completely converge with the PTV curve for doses received by less than 40% of the volume. This indicates a greater relative dose being deposited to the OARs in the McNamara calculation. The mean and maximum FLUKA calculated PS doses are shown in Figure 5.9.

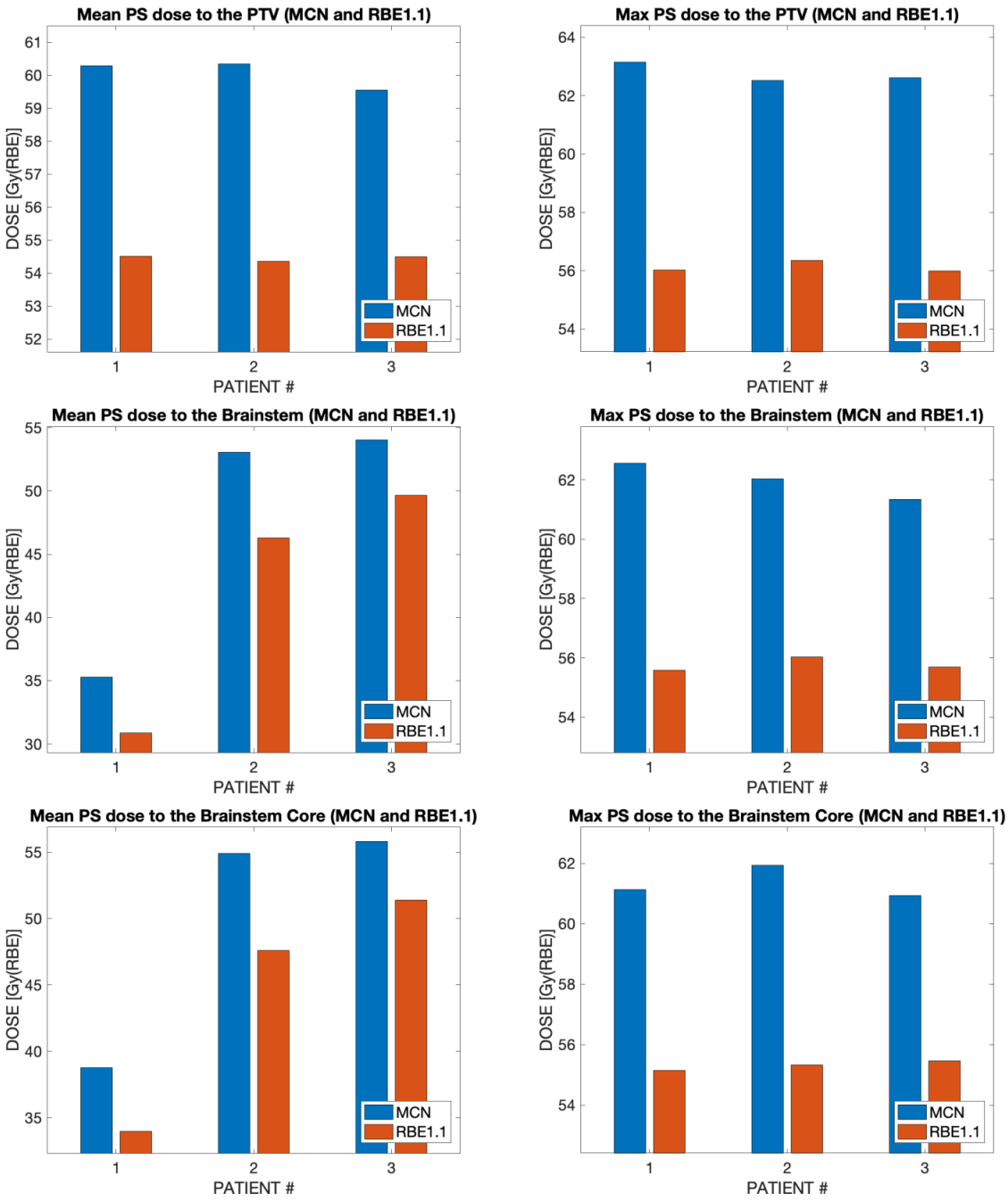

Figure 5.9: The mean and maximum PS doses delivered to the different ROIs calculated using RBE1.1 and McNamara (MCN).

For all patients, the McNamara calculated doses exceed the RBE1.1 calculated doses. This is the case for both the mean and the maximum doses delivered to all structures of interest, which would indicate that the McNamara RBE values are greater than the fixed value of 1.1 within all of these. The deviation of the dose values is around 5-7 Gy for all structures and patients.

5.2.2 Pencil Beam Scanning

Figure 5.10 shows the FLUKA dose distributions delivered by PBS to patient 2. The McNamara calculated doses are on the left and the fixed RBE1.1 calculated doses are in the middle. The dose difference distributions are shown in the right-hand panel.

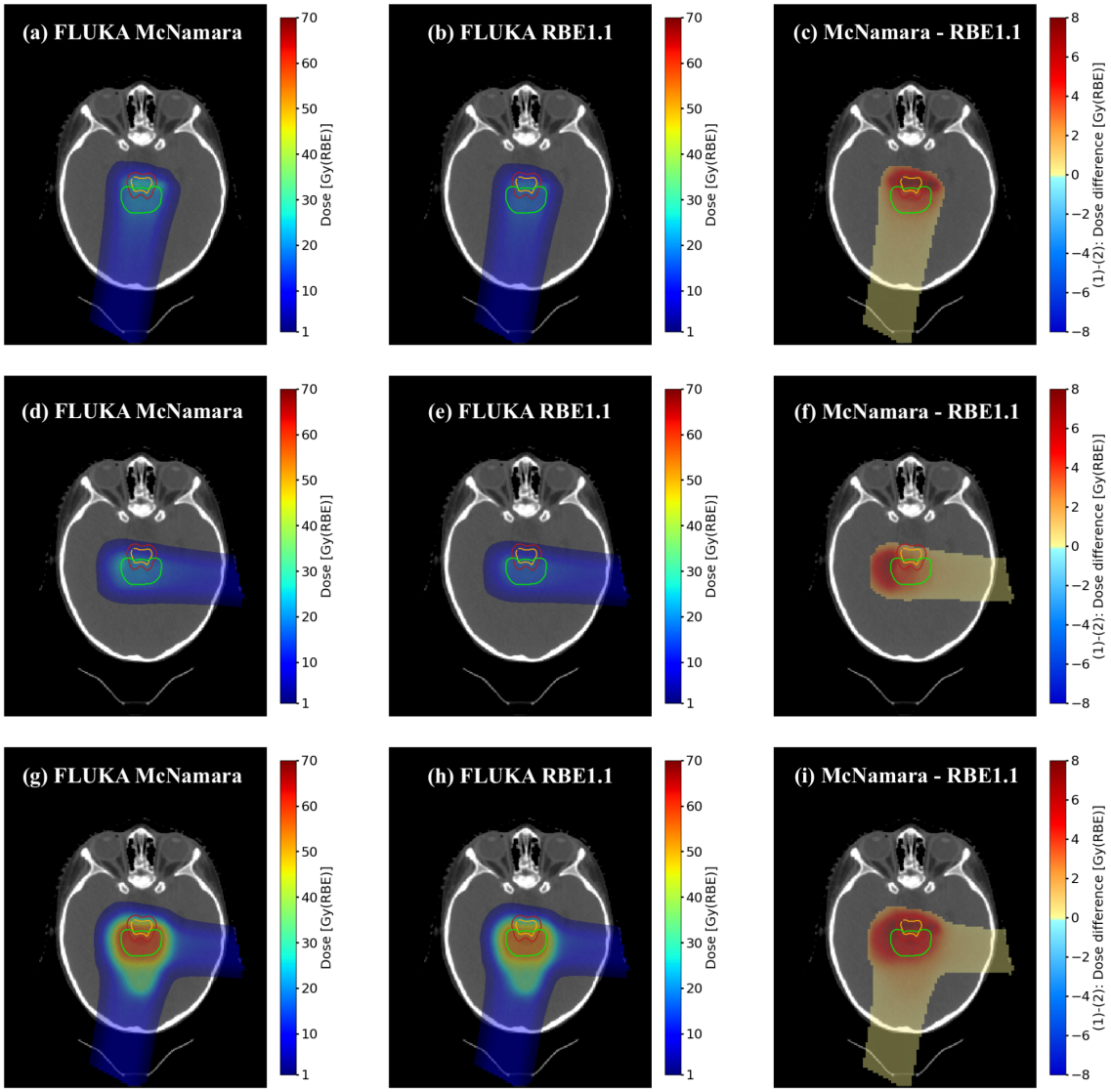

Figure 5.10: PBS dose distributions calculated using McNamara (left) and RBE1.1 (middle) for two single fields, as well as the combined distributions of all three treatment fields. The difference distributions are shown on the right. The PTV is marked with green, the brainstem with red and the brainstem core with orange.

While there is an increased dose conformity compared to PS, the same tendencies are apparent in Figure 5.10 as those present in Figure 5.7. A greater dose deposition is once again found both within and at the distal ends of the target volume, leading to an increase in the dose delivered to the PTV as well as to the OARs. Additionally, the difference plots demonstrate a slight proximal buildup, although less significant than for PS. The McNamara and RBE1.1

calculated PBS doses received by the different structures in patient 2 are shown in the DVH in Figure 5.11.

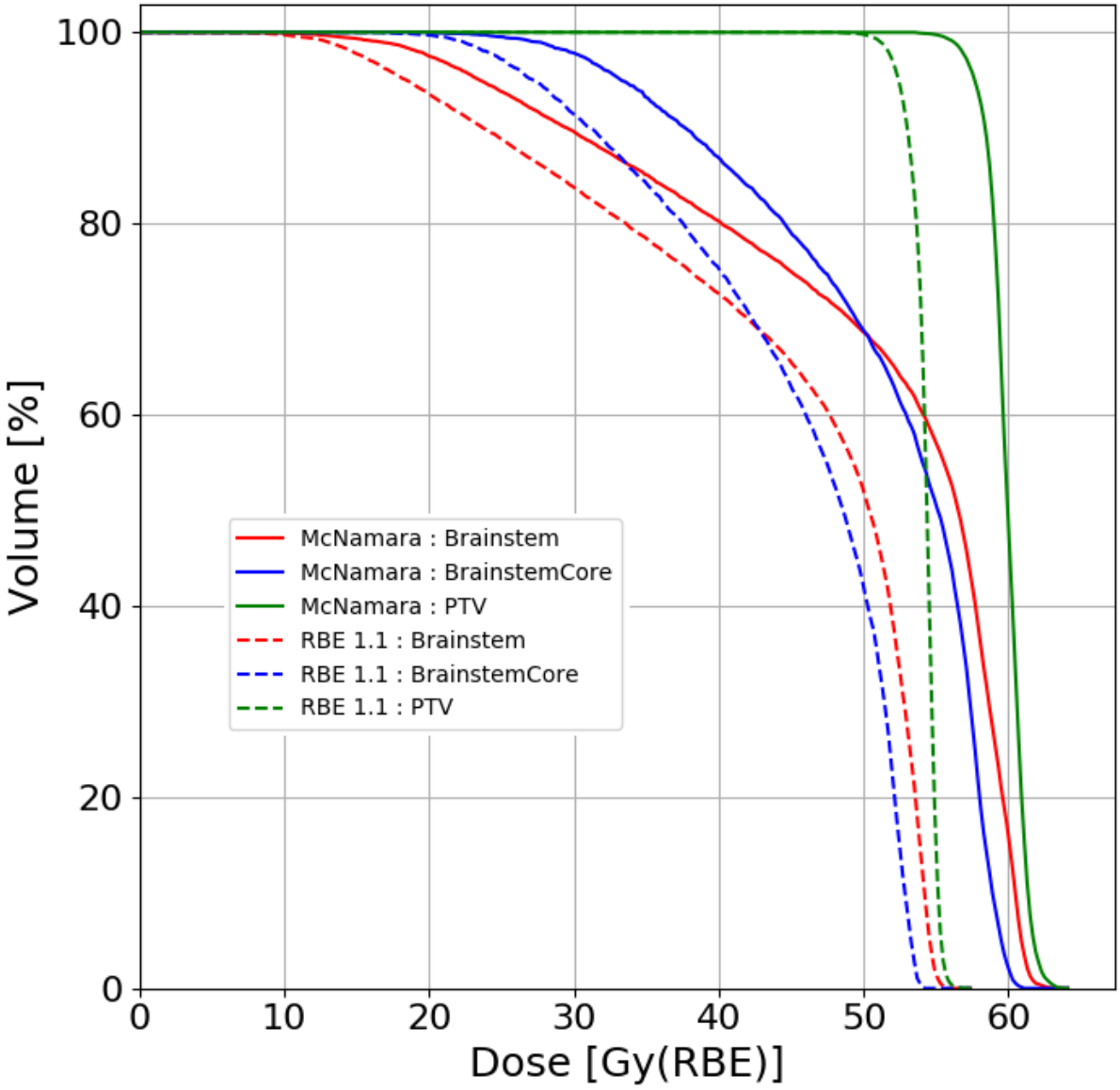

Figure 5.11: Comparison of the PBS doses received by the different structures in patient 2 as calculated by RBE1.1 (dashed lines) and McNamara (solid lines).

As was the case in Figure 5.8, a significant deviation between the two dose calculation techniques is apparent in Figure 5.11. The curves which describe the doses calculated by McNamara are for all structures greater than those found by RBE1.1. All of the McNamara curves appear to deviate a relatively fixed amount from their RBE1.1 counterparts, something

which was not the case for PS. The mean and maximum FLUKA calculated PBS doses are shown in Figure 5.12.

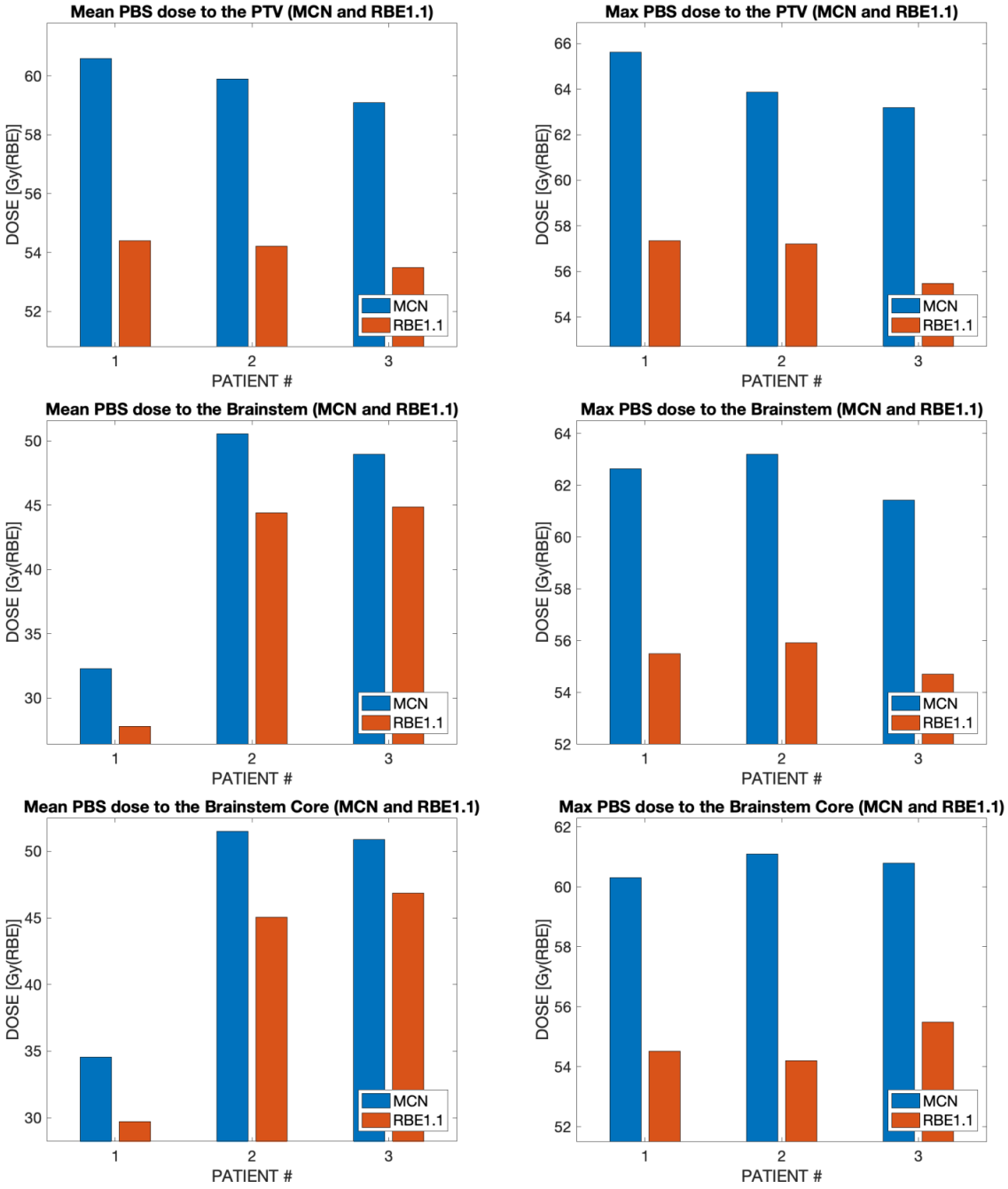

Figure 5.12: The mean and maximum PBS doses delivered to the different ROIs calculated using RBE1.1 and McNamara (MCN).

As is to be expected from Figures 5.10 and 5.11, the McNamara calculated doses exceed the RBE1.1 calculated doses to all structures. This is the case for both the mean and the maximum

doses, which was the case for PS as well. The deviation between the two dose calculation techniques is around 5-7 for this modality as well.

5.3 Comparison of PBS and PS Dose Estimates

5.3.1 Doses Calculated with RBE1.1

Figure 5.13 shows the RBE1.1 dose distributions delivered by PBS and PS to patient 2. The PBS doses are on the left and the PS calculated doses is in the middle. The dose difference distribution is shown in the right-hand panel.

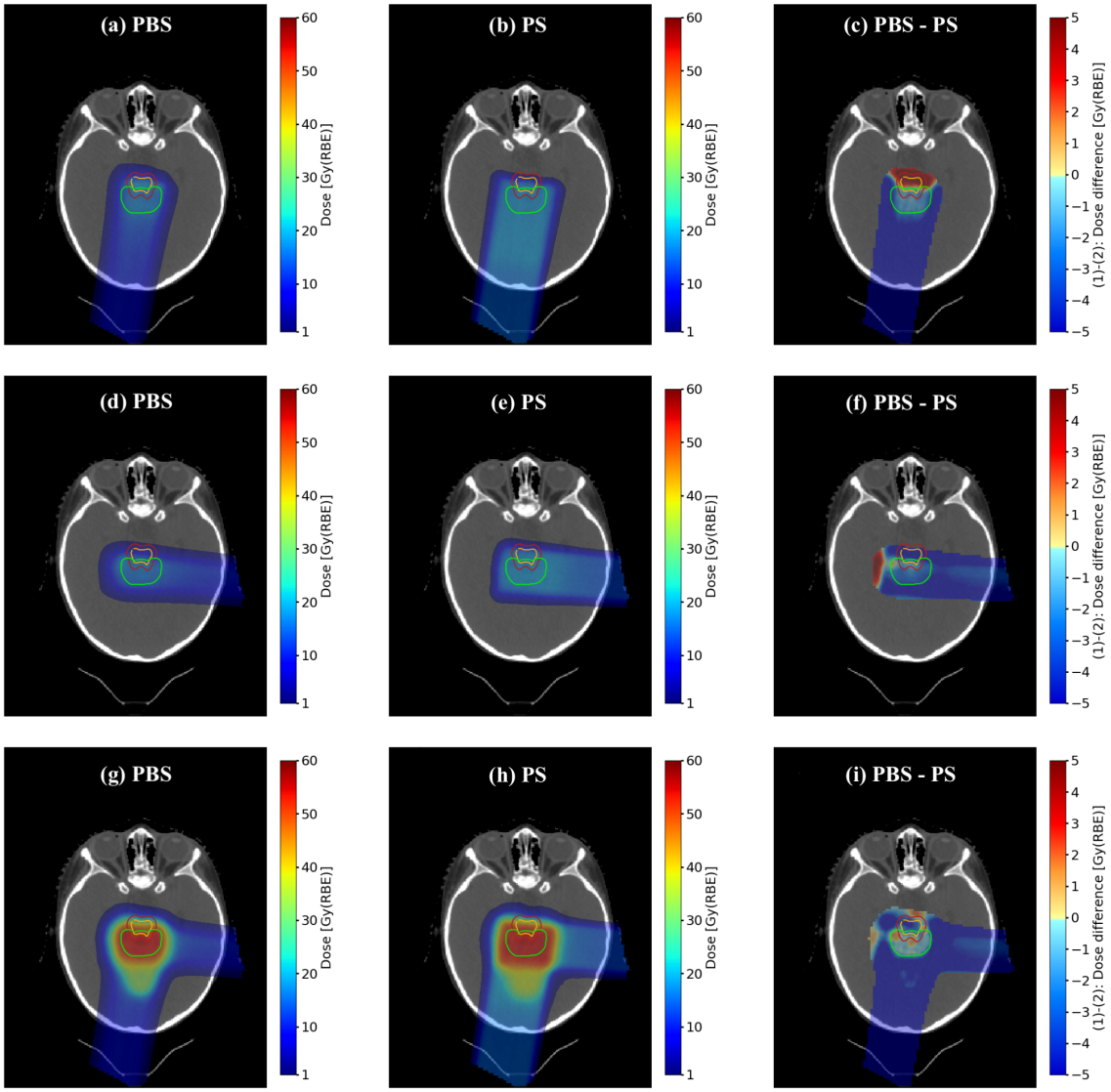

Figure 5.13: PBS (left) and PS (middle) dose distributions calculated using RBE1.1 for two single fields, as well as the combined distributions of all three treatment fields. The difference distributions are shown on the right. The PTV is marked with green, the brainstem with red and the brainstem core with orange.

The PBS exhibits a greater dose conformity than PS, as expected from theory and the previously presented results. The difference distributions show that the PS modality deposits a generally larger dose proximally than PBS does. However, this is also the case for the region immediately surrounding the target volume, a region in which both OARs are located. Although the difference plots show a greater distal dose deposition for the PBS modality, the dose deposited to the OARs by PS appear to be slightly greater than the dose deposited by

PBS. The doses deposited to the PTV is similar for the two modalities. The RBE1.1 doses received by the different structures in patient 2 are shown for both treatment modalities in the DVH in Figure 5.14.

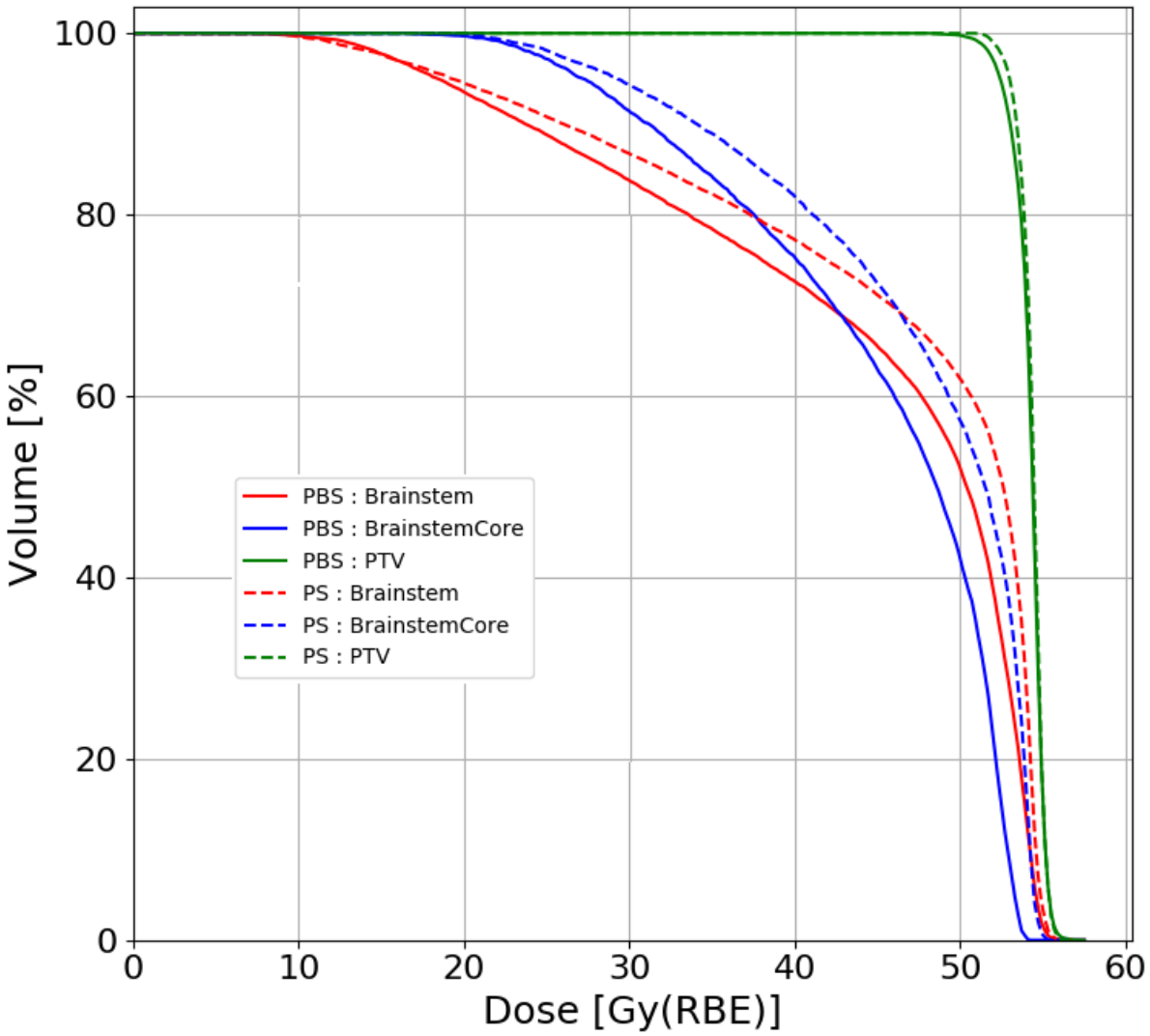

Figure 5.14: Comparison of the PS (dashed lines) and PBS (solid lines) doses received by the different structures in patient 2 calculated with RBE1.1.

As the figure shows, PS is expected to deliver a greater dose to all structures. While the PTV curves are very similar, the deviation between the two modalities is most apparent when considering the curves which describe the OARs. For these structures, the PBS curves have a steeper slope, indicative of a smaller dose delivered to these structures. Although the brainstem curves eventually converge, this is not the case for the brainstem core. Based on Figure 5.14,

PBS demonstrates a similar target coverage as PS, but with a greater sparing of the OARs. The mean and maximum RBE1.1 calculated doses delivered by PS and PBS are presented in Figure 5.15.

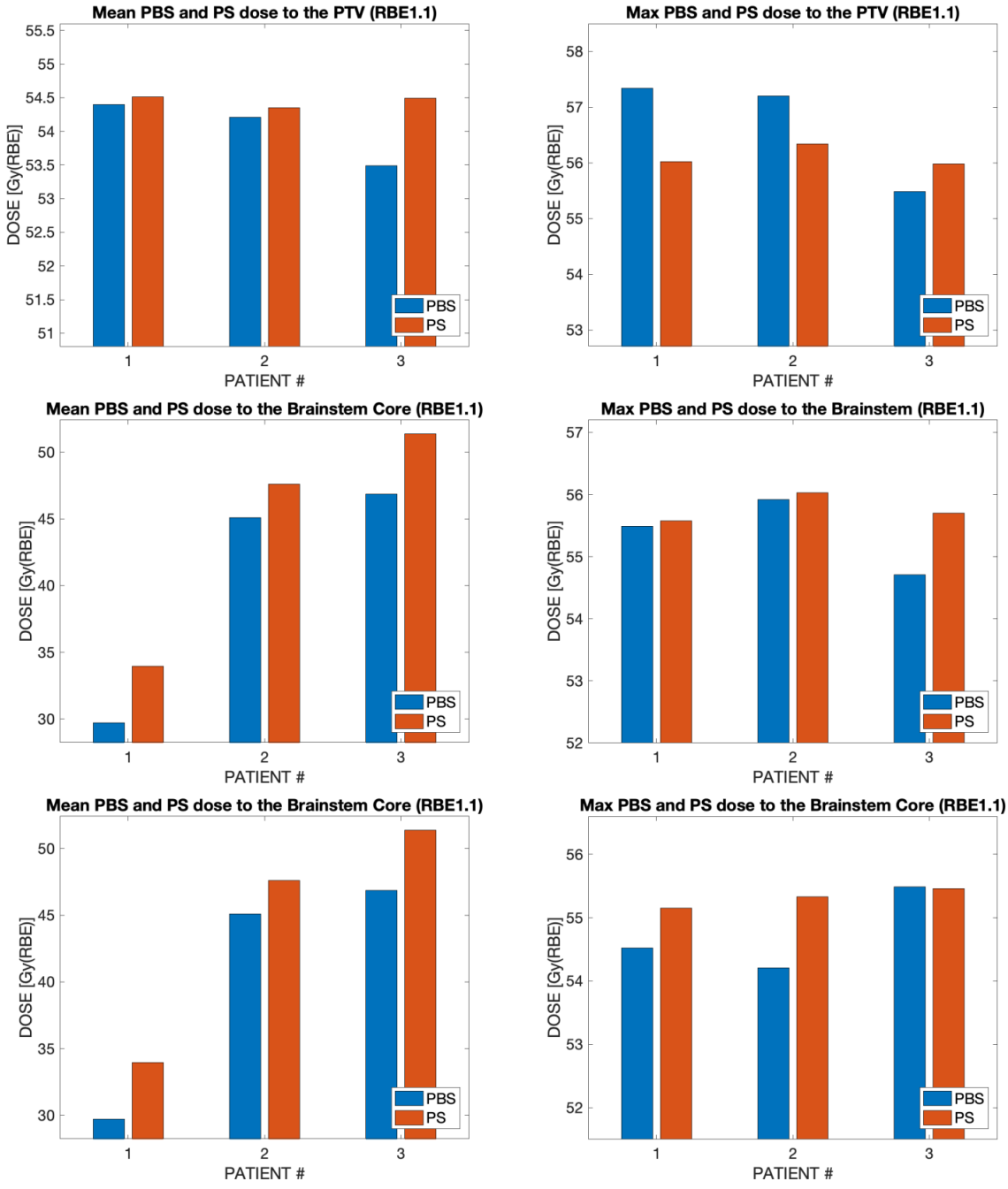

Figure 5.15: The mean and maximum PS and PBS doses delivered to the different ROIs calculated using RBE1.1.

The mean dose delivered to the PTV is quite similar for the two modalities, as is to be expected from Figure 5.14, with the PS doses being slightly greater than the PBS doses. The opposite is mainly true when considering the maximum doses to the PTV, with patient 3 being the exception. The mean doses delivered to the OARs are in all cases greater for the PS modality, which is also consistent with the results presented in Figures 5.13 and 5.14. The maximum values received by these structures are, however, comparable between the two modalities, although the PS maximums tend to be slightly greater.

5.3.2 Doses Calculated with McNamara

Figure 5.16 shows the McNamara dose distributions delivered by PBS and PS to patient 2. The PBS doses are on the left and the PS calculated doses is in the middle. The dose difference distribution is shown in the right-hand panel.

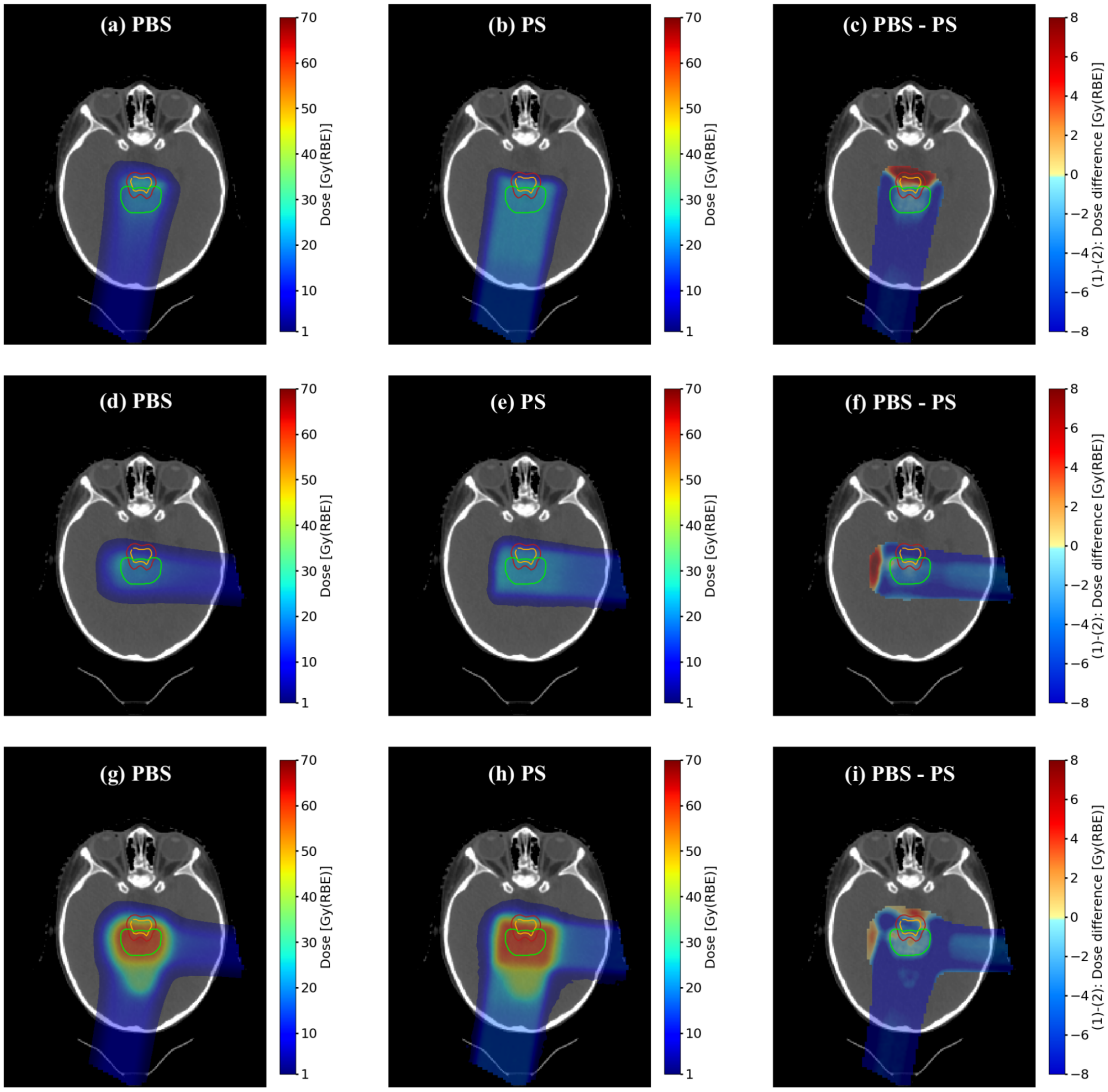

Figure 5.16: PBS (left) and PS (middle) dose distributions calculated using McNamara for two single fields, as well as the combined distributions of all three treatment fields. The difference distributions are shown on the right. The PTV is marked with green, the brainstem with red and the brainstem core with orange.

Figure 5.16 exhibits the same tendencies present in Figure 5.13, with the PBS distribution demonstrating a superior dose conformity. With the exception of the distal ends of the fields, the difference plots show a greater dose being deposited by PS both proximally and immediately surrounding the target volume. Although the increased distal dose deposited by PBS partly affects the brainstem, the total dose delivered to the OARs appear to be generally higher for the PS modality. The dose deposited within the PTV appears to be generally greater

for PS. The McNamara doses received by the different structures in patient 2 are shown for both treatment modalities in the DVH in Figure 5.17.

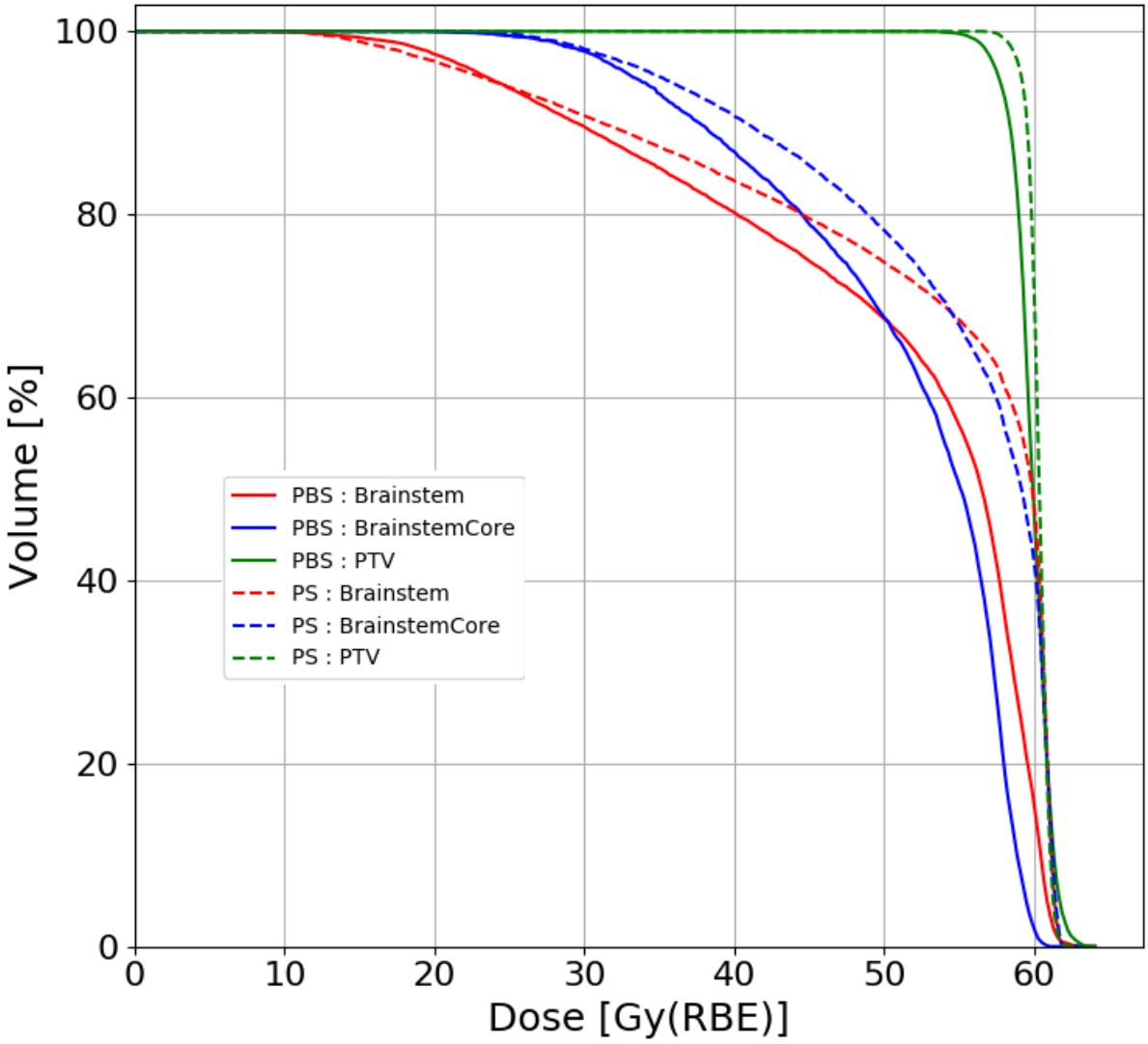

Figure 5.17: Comparison of the PS (dashed lines) and PBS (solid lines) doses received by the different structures in patient 2 calculated with McNamara.

Although all the PS curves converge with the PBS PTV curve for doses received by 40% of the volume and below, the curves associated with the former modality predict a larger total dose delivered to all structures. The curves which describe a given structure in one modality deviate more from their counterparts than was the case in Figure 5.14, where a fixed RBE was considered. This indicates differences in the LET_d of the two modalities, as this would lead to deviations in the delivered dose. Figure 5.17 predicts a greater mean dose deposited to the

PTV by PS than by PBS, although the latter demonstrates an increased sparing of the OARs. The mean and maximum McNamara doses delivered by both proton modalities are presented in Figure 5.18.

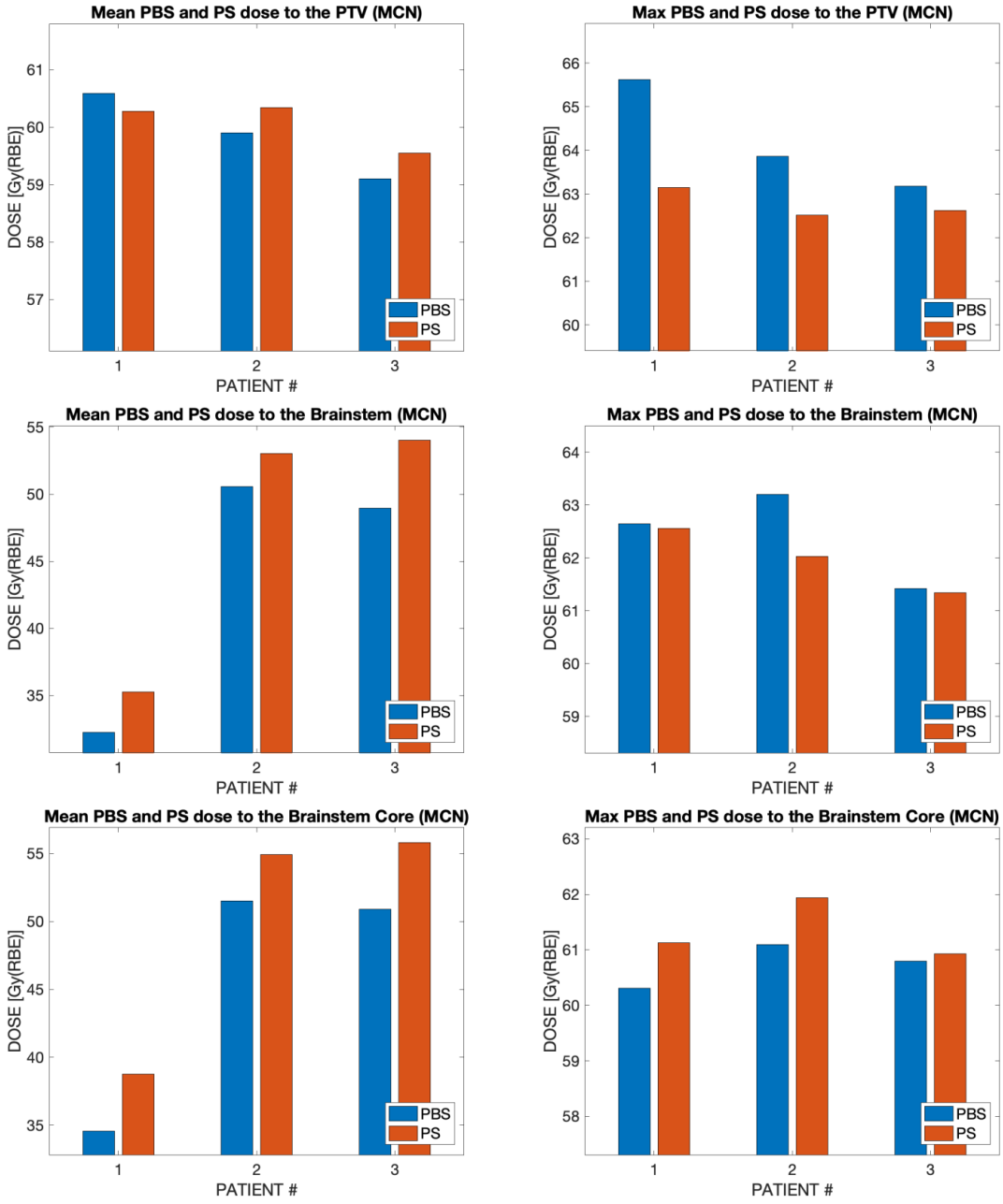

Figure 5.18: The mean and maximum PS and PBS doses delivered to the different ROIs calculated using McNamara.

As Figure 5.18 shows, PBS is expected to deliver a lower mean dose than PS to both of the OARs, which is consistent with Figure 5.16 and 5.17. The maximum doses delivered to the

brainstem cores are slightly greater for the PS modality, while the opposite is true for the brainstems. This is in good agreement with Figure 5.16. While the mean doses delivered to the PTVs are similar for similar for the two modalities, PBS is expected to deliver a greater maximum dose to this structure.

5.3.3 Comparison of the PTV Dose Conformity

Figure 5.19 shows a comparison of the D05-D95 values for both proton modalities for RBE1.1 (left) and McNamara (right).

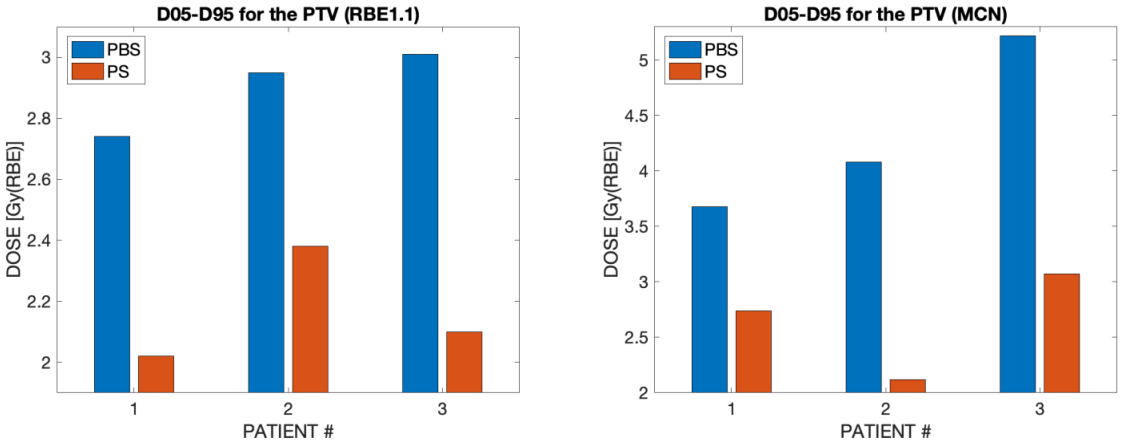

Figure 5.19: D05-D95 values for PS and PBS calculated with RBE1.1 (left) and McNamara (right)

As Figure 5.19 shows, the D05-D95 values of the PBS modality are in all cases greater than those of PS. This indicates a greater dose conformity for the former modality, which is consistent with Figures 5.13 and 5.16. While there is an increase for all patients when considering the PBS modality, this is not the case for PS, with the value even becoming lower in the case of patient 2. Additionally, the increase is more dramatic for PBS than for PS when comparing RBE1.1 and McNamara.

5.3.4 Comparison of the Dose Constraints to the OARs

A comparison of the D50 values of the brainstem calculated for both modalities using both FLUKA dose calculation techniques are shown in Figure 5.20.

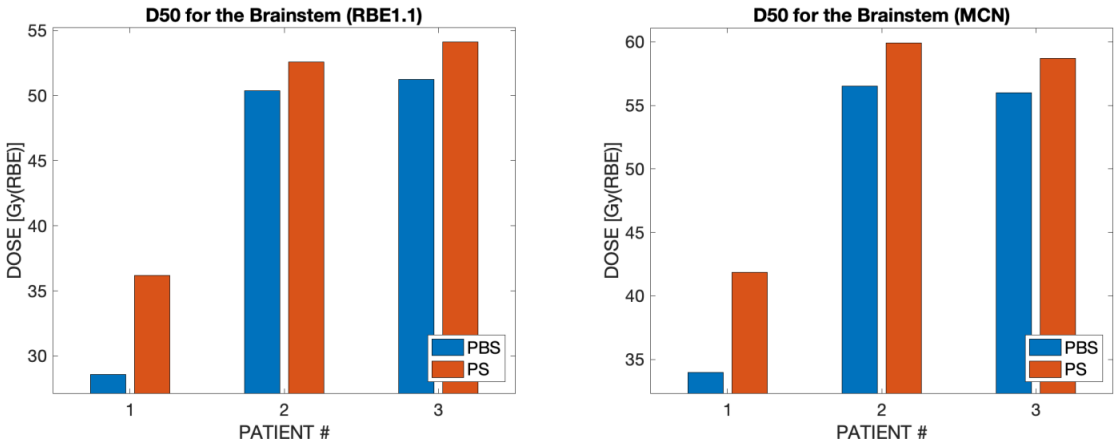

Figure 5.20: Comparison of the PS and PBS D50 dose values of the brainstem, calculated with RBE1.1 (left) and McNamara (right)

As the figure shows, the PS D50 values are in all cases greater than the PBS value. The differences between the two modalities is similar for both dose calculation techniques, although the McNamara values are greater than the RBE1.1 values. The McNamara values for patient 2 and 3 exceed the constraint of $D_{50} < 54$ Gy. The D1CC values of the brainstem core calculated for both modalities using both FLUKA dose calculation techniques are shown in Figure 5.21.

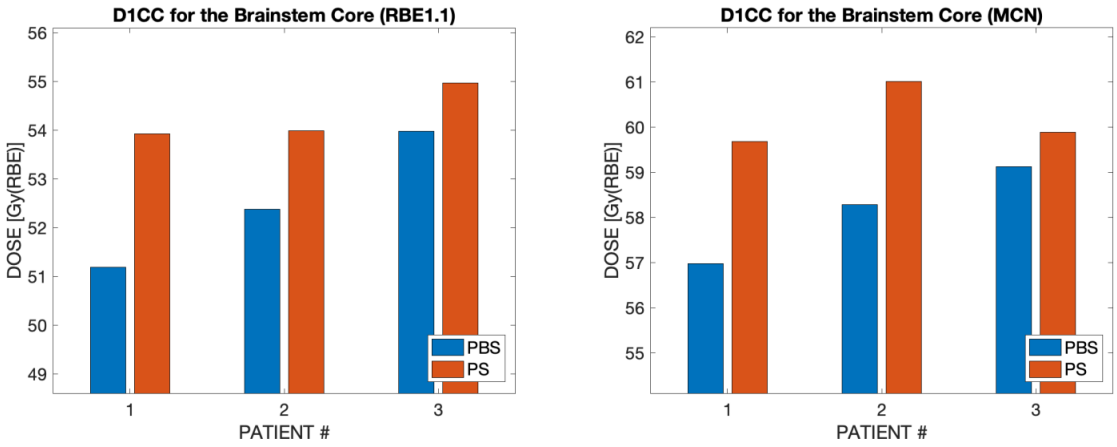

Figure 5.21: Comparison of the PS and PBS D1CC dose values of the brainstem core, calculated with RBE1.1 (left) and McNamara (right)

As was the case for the D50 values, the PS D1CC values exceed the PBS values for both dose calculation techniques. While all RBE1.1 values are below the constraint of D1CC < 56.1 Gy, the opposite is true for the McNamara dose values.

5.4 Comparisons of LET_d and RBE

5.4.1 Comparison of the LET_d Distributions

Figure 5.22 shows the LET_d distributions of PBS (left) and PS (middle) delivered to patient 2. The difference between the distributions are shown in the right-hand panel.

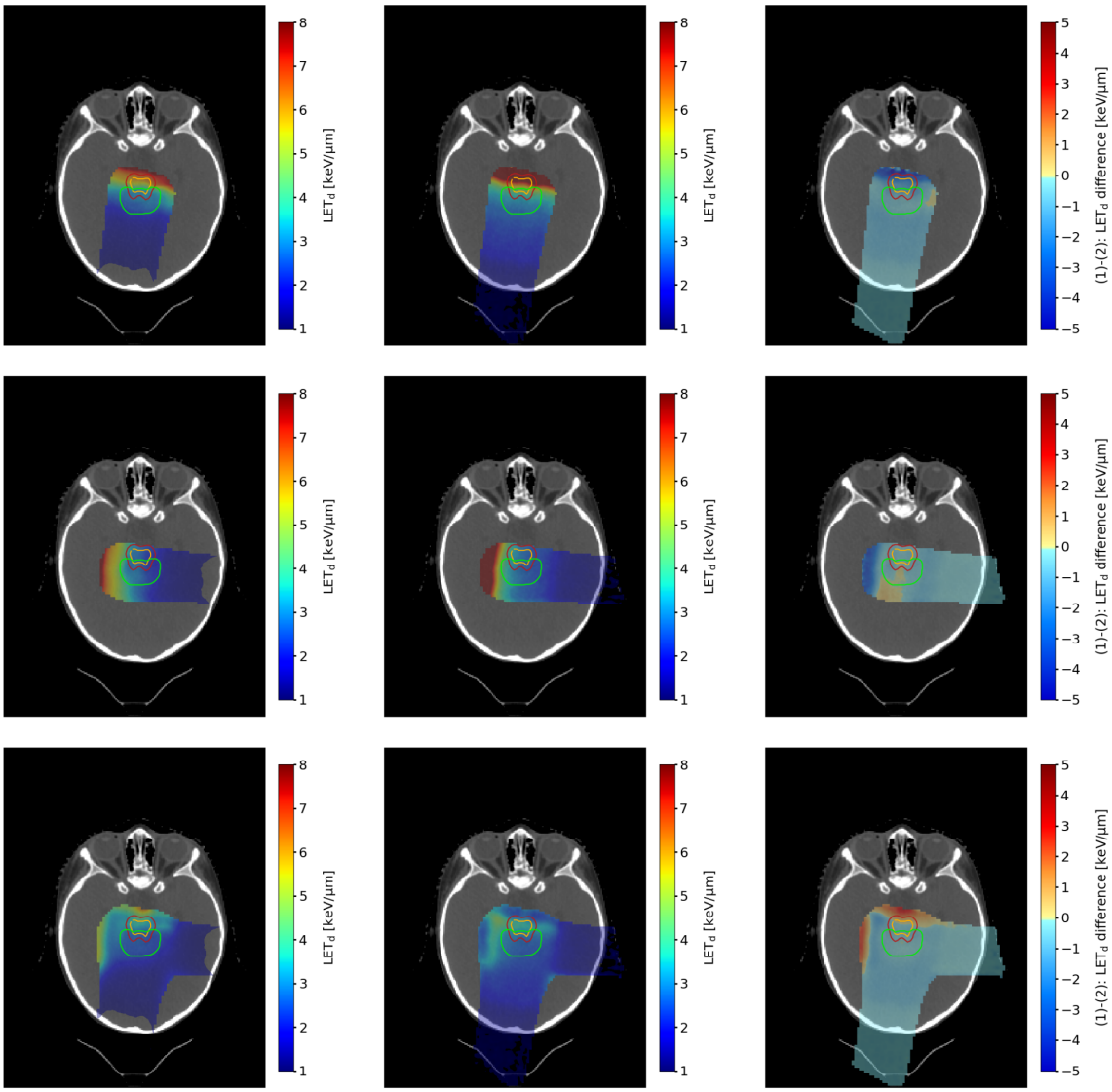

Figure 5.22: PBS (left) and PS (middle) LET_d distributions for two single fields, as well as the combined distributions of all three treatment fields. The difference distributions are shown on the right. The PTV is marked with green, the brainstem with red and the brainstem core with orange.

As is expected from the increased distal doses in the difference plots in section 5.2, both modalities exhibit an increase in the LET_d values at the distal ends of their respective fields. As the difference distribution in Figure 5.22i shows, the values are similar proximal to the target volume, as well as within the PTV. While PBS exhibits a greater LET_d at the most distal parts of its fields in Figure 5.22i, Figure 5.22b indicates that PS has a greater LET_d within the OARs. The LET_d received by the different structures are for both modalities presented in the LET_d volume histogram (LVH) in Figure 5.23.

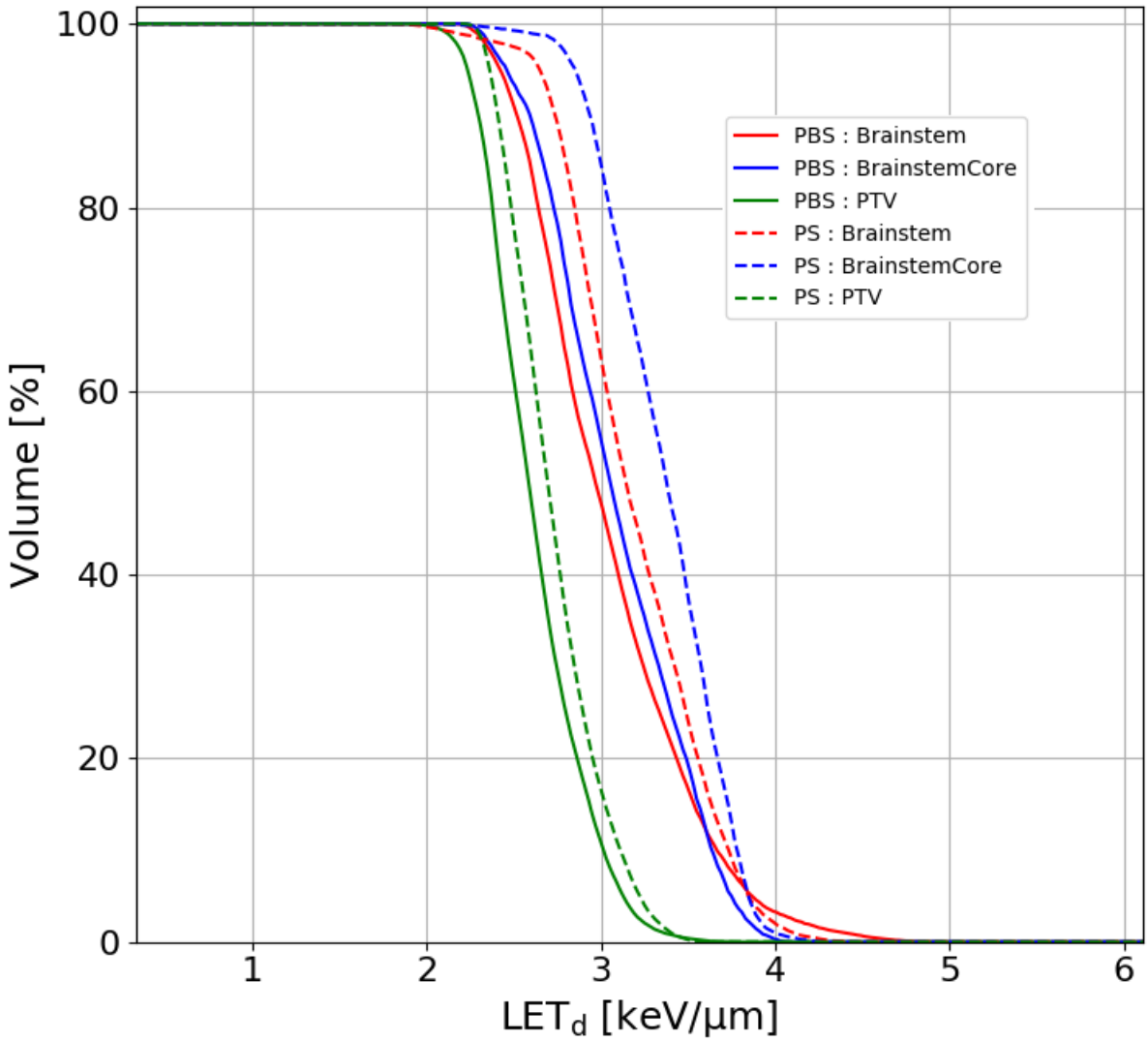

Figure 5.23: Comparison of the PS (dashed lines) and PBS (solid lines) LET_d received by the different structures in patient 2.

The curves present in Figure 5.23 have very similar slopes when comparing the structures across the modalities. The PS curves are generally greater than the PBS curves for all structures, with the exception being the PBS brainstem curve. This curve, which has the longest tail of all the curves, overtakes its PS counterpart for LET_d values inside 5% of the volume and below. The LET_d within the target volume is lower than the LET_d within the OARs for both modalities, which is consistent with the results presented in section 5.2. The mean and maximum LET_d within each of the ROIs are presented in Figure 5.24 for both PS and PBS.

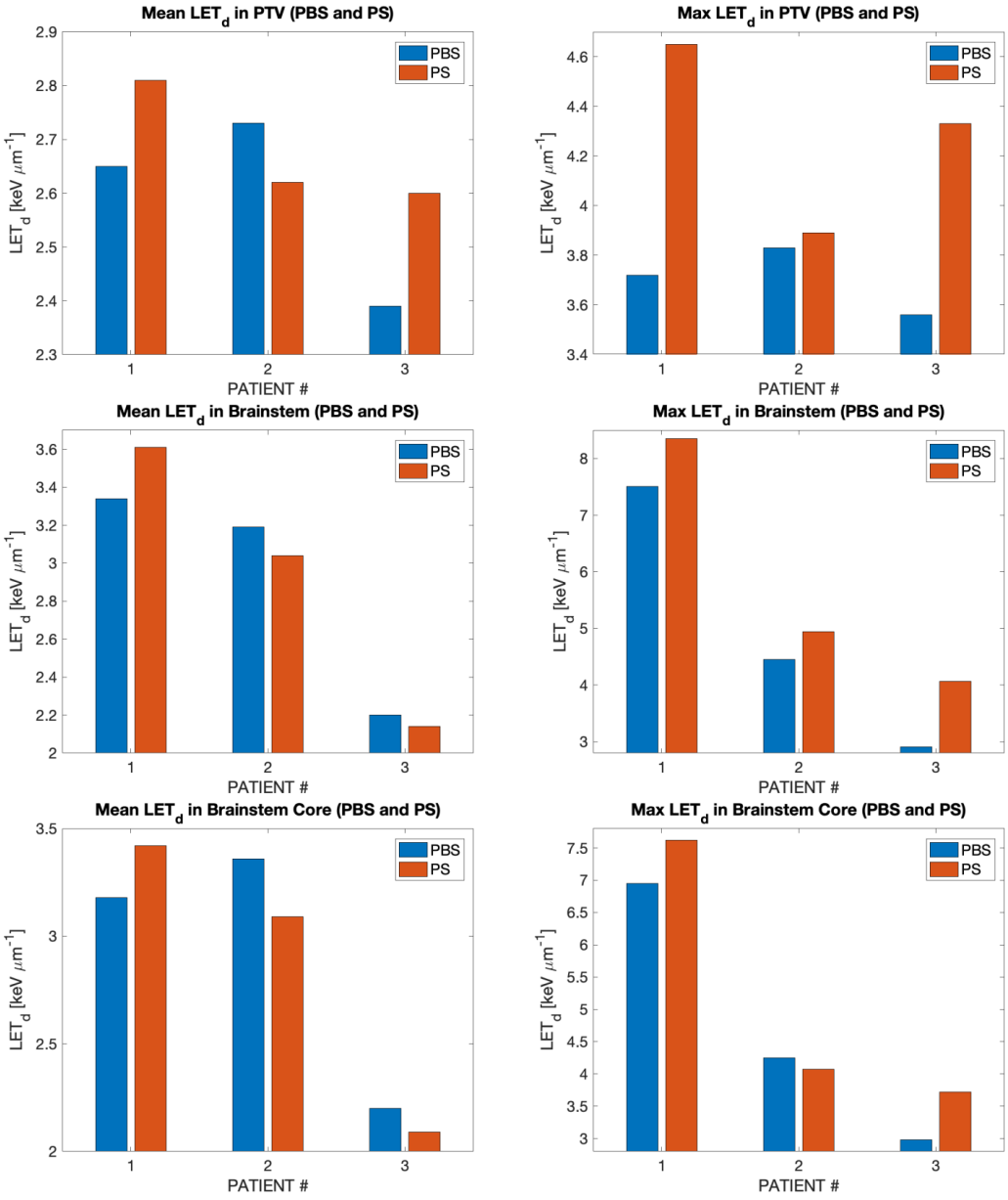

Figure 5.24 The mean and maximum PS and PBS LET_d values delivered to the different ROIs.

As Figure 5.24 shows, the mean LET_d associated with each patient is similar for each structure when comparing the two modalities. While the PS mean LET_d to the PTV exceeds that of PBS for patients 1 and 3, the opposite is true for the OARs and patient 2 and 3. Regardless, the deviations between the two modalities are small. When considering the maximum LET_d, on the other hand, the PS values are generally greater than its PBS counterparts. The one exception is the max LET_d delivered to the brainstem core of patient 2, although these are comparable in value.

5.4.2 Comparison of the RBE Distributions

Figure 5.25 shows the McNamara RBE distributions of PBS (left) and PS (middle) for patient 2. The difference between the distributions are shown in the right-hand panel.

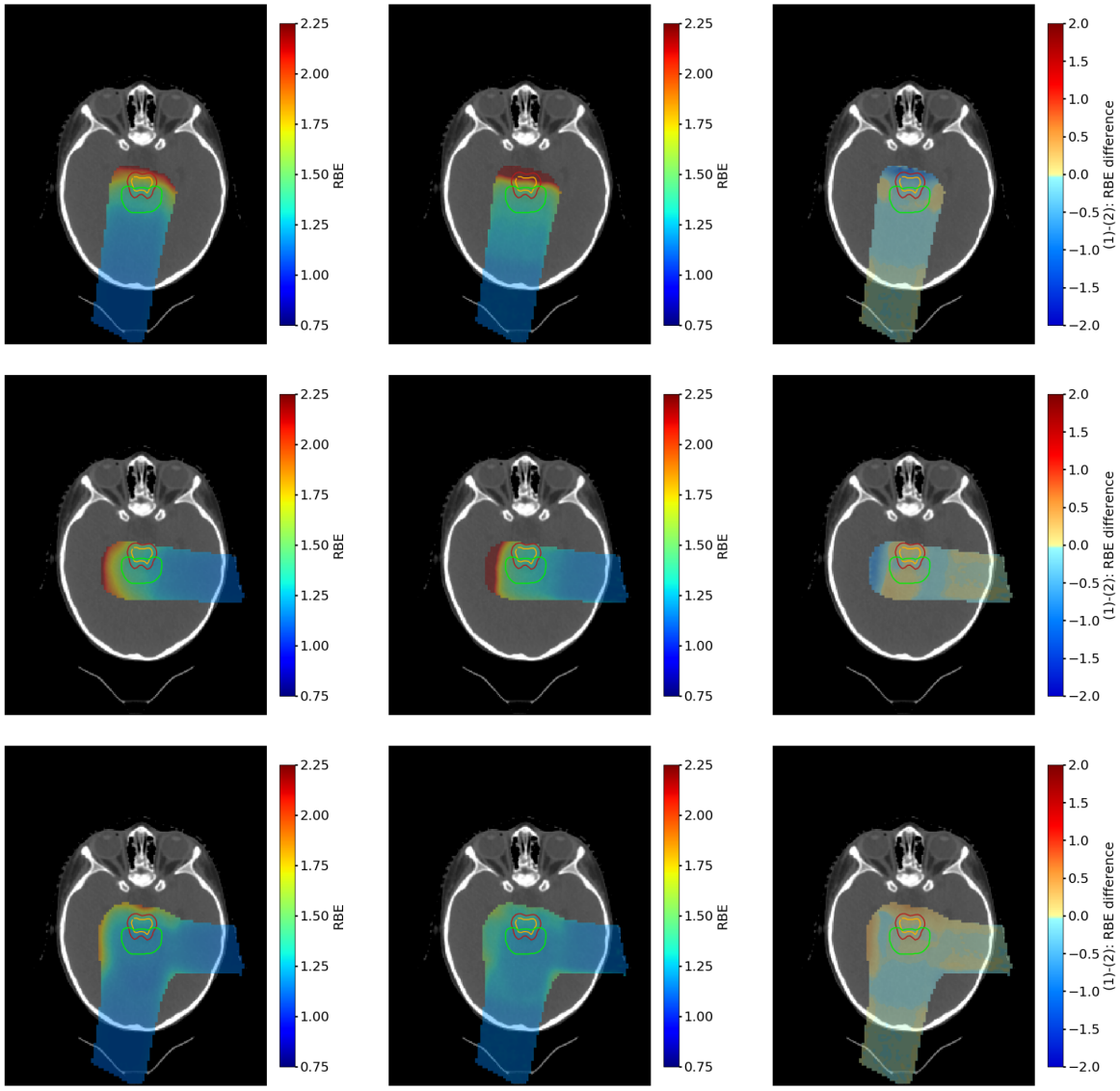

Figure 5.25: PBS (left) and PS (middle) RBE distributions for two single fields, as well as the combined distributions of all three treatment fields. The difference distributions are shown on the right. The PTV is marked with green, the brainstem with red and the brainstem core with orange.

The McNamara RBE distributions presented in Figure 5.25 are very similar to the LET_d distributions in Figure 5.22. Both treatment modalities exhibit an increase in RBE at the ends of their respective fields, an increase which appears comparable when considering the difference plots in Figure 5.25. While the values are mostly comparable proximal to the target volume, PBS exhibits a greater value both within the target volume and at the distal ends of the fields. The RBE within the different structures for both treatment modalities are presented in the RBE volume histogram (RVH) in Figure 5.26.

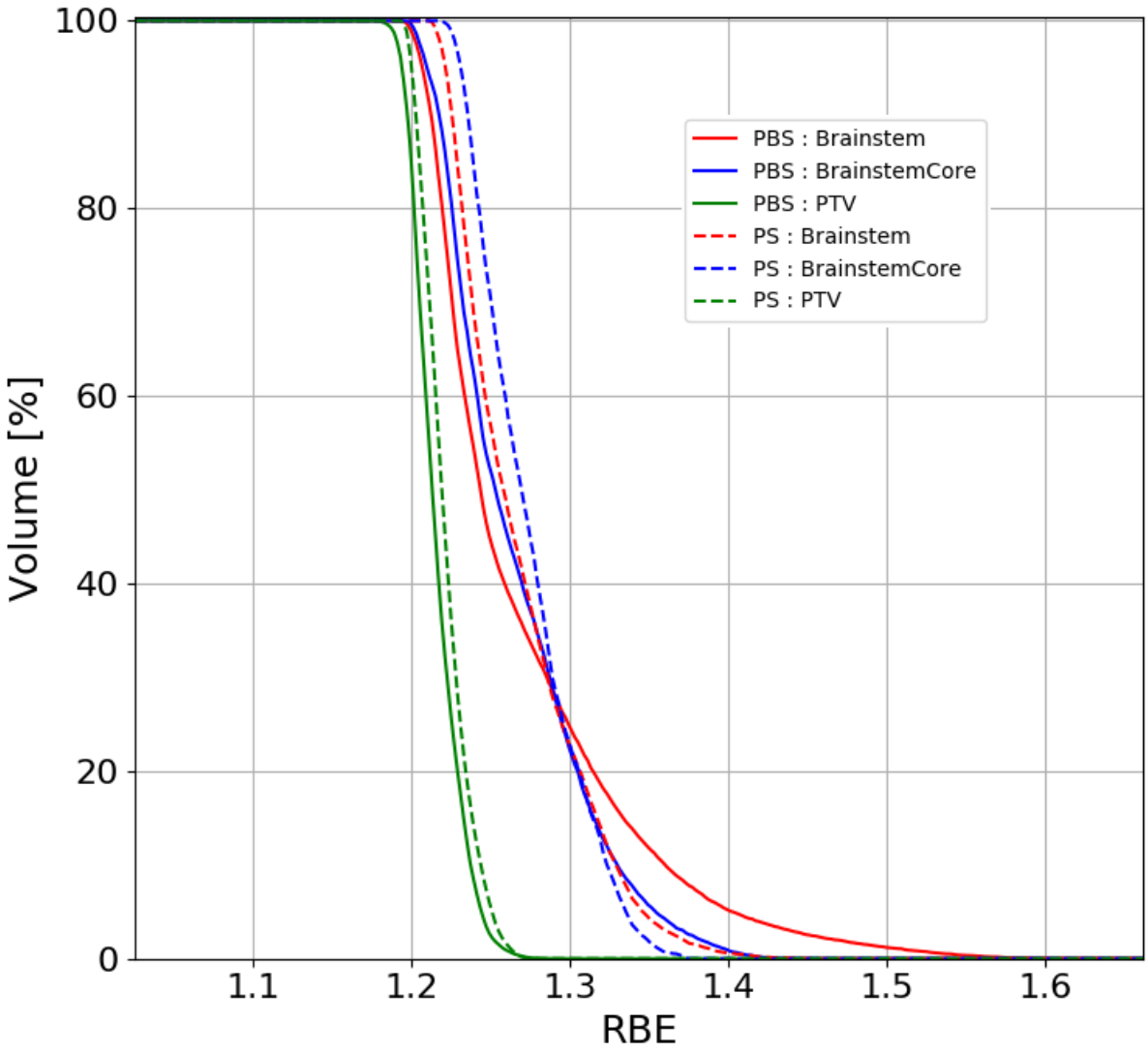

Figure 5.26: Comparison of the PS (dashed lines) and PBS (solid lines) RBE within the different structures in patient 2.

As is to be expected from theory, Figure 5.26 is quite similar to the LVH presented in Figure 5.23. Although the curves are generally closer together in Figure 5.26, the same tendencies occur in both. The curves which describe the OARs are greater than those describing the PTV, while the PS curves are generally greater than their PBS counterparts. However, while only the PBS brainstem curve overtook the PS curve in Figure 5.23, both PBS OAR curves overtake the PS OAR curves. The PBS curve which describes the brainstem core overtakes its PS counterpart for RBE values within 15% of the volume. Beyond this point the former curve has a more gradual slope, which leads to a slight tail. The PBS brainstem curve overtakes the corresponding PS curve for RBE values within 30% of the volume, beyond which point the

slope of the PBS curve flattens out, leading to a large tail. The mean and maximum RBE values within each structure is presented in Figure 5.27 for both PS and PBS.

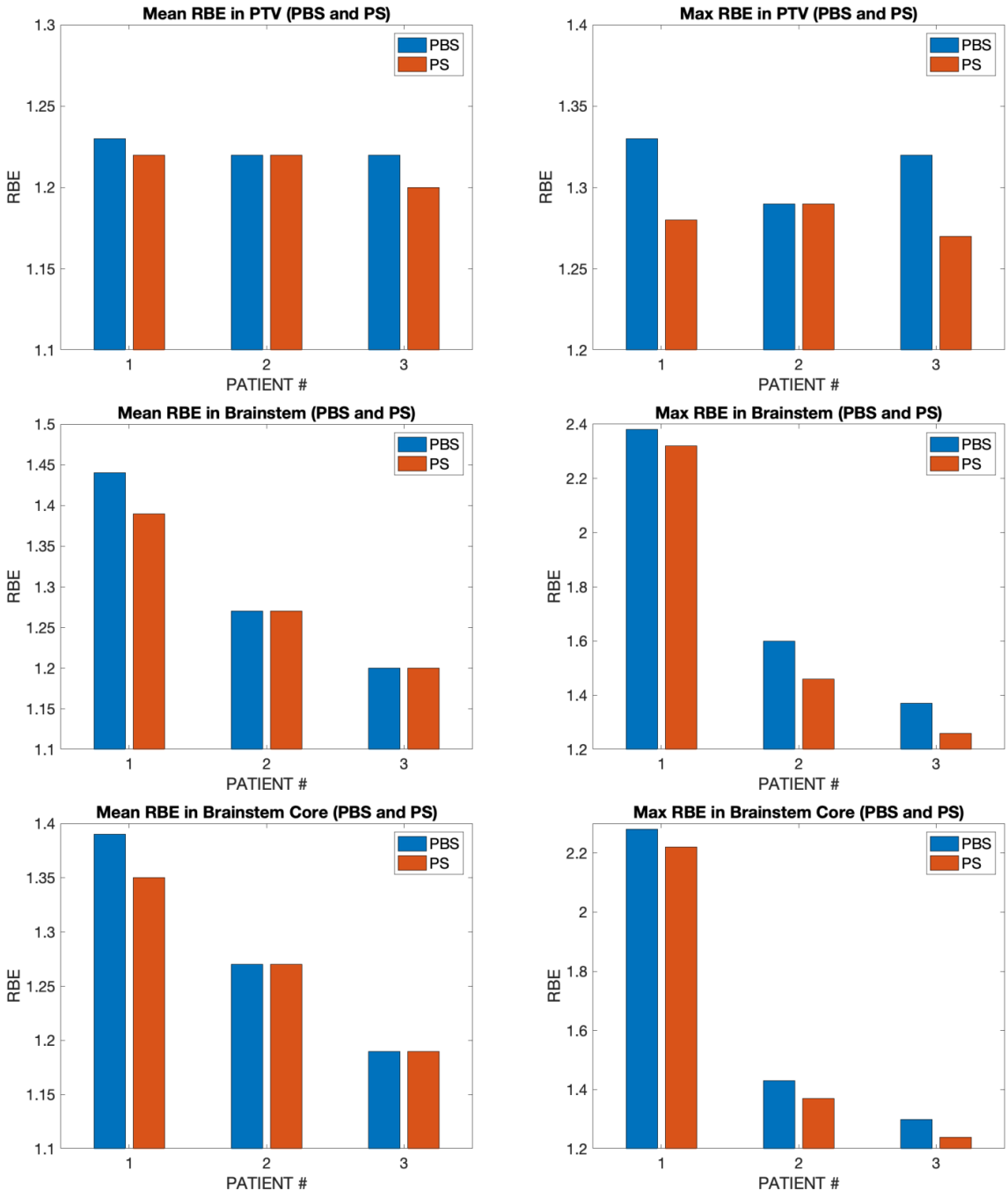

Figure 5.27: The mean and maximum PS and PBS RBE values delivered to the different ROIs.

As Figure 5.27 shows, the mean RBE values within all structures are either comparable or greater for the PBS modality. The deviations between the two modalities are, however, quite small, indicating a comparable mean value delivered by both treatment modalities. The mean RBE within the OARs are either similar or greater than the mean RBE within the PTV for all patients, which is true for the maximum RBE values as well. The maximum values within the RBE are mainly greater for PBS than PS, with the exception being the RBE within the PTV of patient 2. Here, the RBE appears to be equal for the two modalities. The PBS maximums to the OARs exceed the PS maximums in all cases, most significantly so in the case of patient 1. It is worth noting that all RBE values in Figure 5.27 exceed the clinically used RBE of 1.1.

6. Discussion

Using treatment information stored in various DICOM files, a PS proton therapy simulation could be defined with the required nozzle configuration. This made it possible to compare MC calculated dose distributions for the PS modality to the PBS modality. These could also be compared to their TPS calculated distributions.

As was presented in the results (Figure 5.1 and 5.4) the dose distributions calculated with the TPS and RBE1.1 showed good agreement. For both proton treatment modalities, the FLUKA calculated dose distributions exhibited a similar dose conformity as those of the TPS. An increase in the distal dose deposition was observed in the FLUKA distributions of both modalities, although this was most significant for PS. This indicates the presence of heterogeneous tissue along the field path, which would cause discrepancies in the range calculations between the two dose calculation methods as this is not taken into account by the pencil-beam algorithms of the TPS. This agrees well with the findings made by Paganetti *et al*. [11]. A consequence of this would be the presence of a slightly greater TPS calculated dose more proximally within the fields, which is indeed what is observed in the both dose distributions. While the dose deposition within the PTV is similar for the two techniques, the increased distal dose deposition found by the RBE1.1 calculations would suggest an increased dose received by the OARs, in particular for the PS modality. The DVHs in Figure 5.2 and 5.4 show that the two methods of dose calculation expect a similar dose to be received by the PTV for both treatment modalities. When considering the OARs, however, PS and PBS differ. While the FLUKA calculation for the latter modality estimates a slightly lower dose deposition within the OARs than the TPS does, the opposite is true for PS, which is consistent with their respective dose distributions. The mean doses delivered to the PTV are very similar for both techniques in either treatment modality, with all of them being within 2% of the prescribed dose of 54 Gy to this volume. For the PBS modality, the mean doses estimated by the TPS are in all cases slightly greater than their FLUKA counterparts, while no such tendency is apparent for PS. The opposite is true, however, when considering the mean doses delivered to the OARs. Although the mean PS doses are once again very similar, all the FLUKA estimates exceed the corresponding TPS doses, which is to be expected from the increased distal dose deposition observed in Figure 5.1. Such a tendency is not observed for the PBS modality. The maximum doses delivered to all structures are very similar for both techniques and both

modalities, although the PS RBE1.1 doses exceed the corresponding TPS doses for all patients. No such pattern occurs for PBS. The doses calculated with RBE1.1 and TPS are in all cases within 1 Gy of each other, i.e. below 2% of the prescription dose, which suggests that the distributions obtained from the two techniques are comparable.

Comparisons between the FLUKA McNamara and FLUKA RBE1.1 dose distributions exhibit a significant difference between them for each treatment modality. While the McNamara doses exceed those of RBE1.1 everywhere, this is most noticeable within and on the distal sides of the target volume, where a region of increased dose deposition is apparent. This region, in which both OARs are contained, extends further for the PS modality compared to PBS. The regions of increased dose deposition in both figures correspond to the regions of increased LET_d and RBE, which is consistent with the findings of Fjæra *et al.* [50] and Yepes *et al.* [23].

The DVHs which compare the target coverages calculated by FLUKA McNamara and FLUKA RBE1.1 for both treatment modalities are consistent with their corresponding dose distributions. The two PTV curves appear to deviate in a constant manner for both modalities, which is also the case for the PBS curves which describe the OARs. For PS, on the other hand, the McNamara OAR curves have a more gradual initial slope than the RBE1.1 curves, indicating a greater relative dose delivered to these structures when a variable RBE is considered. The mean and maximum PS and PBS doses estimated by the two techniques deviate significantly for all patients. The level of deviation is similar for the two modalities, with all McNamara doses being 5-7 Gy greater than their corresponding RBE1.1 doses. This corresponds to an increase of up to 12% for all PTV doses and an increase of up to 17% for the mean OAR doses, while the maximum OAR doses deviate by about 13%. The size of the deviations suggests that the ROIs receive a non-trivial amount of excess dose when a variable RBE is considered, which is consistent with the findings of Giantsoudi *et al.* [25].

The dose distributions in chapter 5.3 indicate that PBS provides a better dose conformity than PS, regardless of the dose calculation technique considered. The D05-D95 values show that this is indeed the case, with the differences between the two modalities being greater for the McNamara calculated doses. The dose distributions further indicate that PS delivers a greater proximal dose than PBS, while PBS deposits a greater distal dose at the very ends of the treatment fields. The PS doses immediately surrounding the PTV, however, are greater than

the PBS doses. The OARs are located at the intersection between the large distal doses deposited by both modalities, with PS appearing to deposit a greater dose than PBS to the brainstem core and vice versa for the brainstem. While the McNamara doses are greater than the RBE1.1 doses, the difference distributions are similar for both dose calculation techniques. The DVH which compares RBE1.1 estimated PS and PBS doses received by the different structures expects similar doses to be delivered to the PTV by both modalities. The curves which describe the OARs deviate more, with PS being expected to deliver a generally greater dose than PBS. The deviations are relatively small, however, and start to converge as the volume percentage decreases. The same tendencies are mostly present in the DVH which compares the McNamara RBE doses, although the PS curves which describe the OARs show a greater relative increase than PBS does. The mean doses received by the PTV is comparable for the two modalities, with their difference being below 2% for all patients. The mean doses received by the OARs are greater for PS than PBS, with an average difference of around 8-10% between the two. The maximum doses received by the PTVs deviate by less than 3% on average, with the PBS doses being generally greater than the corresponding PS doses. The same is true for the maximum doses delivered to the different OARs, where the deviation between the modalities on average are below 2%.

The D50 values for the brainstem are for all patients greater for PS than for PBS, independent of the dose calculation technique considered. The differences are below 6% for patient 2 and 3, while the modalities differ by about 25% for patient 1, whose D50 values are 15-20 Gy less than for the other patients. This deviation could be attributed to differences in the location of the target volume in relation to the brainstem. The McNamara D50 values of patient 2 and 3 all exceed the prescribed dose constraint of 54 Gy, while the D50 values of patient 1 are beneath. Figure 5.21 shows that the PS D1CC values exceed the PBS values for all patients and both dose calculation techniques, with an average deviation of around 3.5%. While the RBE1.1 values are all beneath the constraint of 56.1 Gy, all McNamara values exceed this limit, most significantly so for the PS modality.

7. Conclusion

The TPS and FLUKA RBE1.1 calculated dose estimates were similar for both treatment modalities, with comparable target coverage achieved by the two dose calculation techniques. The same was true for the doses deposited to the OARs by the PBS modality, while the corresponding PS doses exceeded the TPS doses slightly. This indicates that the FLUKA implementation of the PS beamline is correct, and that FLUKA further can be used to explore effects from treatment beyond the capability of the TPS, such as LET and RBE based dose estimates. While the FLUKA RBE1.1 dose estimates were within 2% of the TPS calculated doses for all patients, this was not the case for the McNamara RBE dose estimates: Although PBS still demonstrated an increased sparing of healthy tissue compared to PS, the doses received by the PTV as well as the OARs went up significantly for all patients when including a variable RBE, independent of treatment modality. The D1CC constraint assigned to the brainstem core were for all patients exceeded, with the same being true for 2 out of 3 patients when considering the D50 constraints. The regions of increased dose deposition agreed well with the LET_d and RBE distributions, with the mean RBE values within all ROIs exceeding 1.1. This indicates that the clinical use of an RBE of 1.1 could lead to overdosing of the OARs, which for posterior fossa tumors increases the risk of brainstem necrosis. Although the RBE values estimated for the PBS modality were either similar or greater than those estimated for PS, PBS still provides a better dose conformity. In conclusion, the obtained results indicate that PBS provides superior dosimetric benefits over PS for both a fixed and a variable RBE.

Bibliography

1. National Cancer Institute. *What Is Cancer?* 2015 [cited 2020 May 15]; Available from: https://www.cancer.gov/about-cancer/understanding/what-is-cancer.
2. World Health Organization. *Cancer*. 2018 [cited 2020 May 15]; Available from: https://www.who.int/news-room/fact-sheets/detail/cancer.
3. Burnet, N.G., et al., *Defining the tumour and target volumes for radiotherapy.* Cancer Imaging, 2004. **4**(2): p. 153-61.
4. Gianfaldoni, S., et al., *An Overview on Radiotherapy: From Its History to Its Current Applications in Dermatology.* Open Access Macedonian Journal of Medical Sciences, 2017. **5**(4): p. 521-525.
5. Paganetti, H., *Proton therapy physics*, in *Series in medical physics and biomedical engineering*, H. Paganetti, Editor. 2012, CRC Press: Boca Raton, FL. p. 1-18.
6. Tanabashi, M., et al., *Review of Particle Physics.* Physical Review D, 2018. **98**(3).
7. Hall, E.J. and A.J. Giaccia, *Radiobiology for the radiologist*. 2012, Philadelphia: Wolters Kluwer Health/Lippincott Williams & Wilkins.
8. Choi, W.H. and J. Cho, *Evolving Clinical Cancer Radiotherapy: Concerns Regarding Normal Tissue Protection and Quality Assurance.* Journal of Korean Medical Science, 2016. **31**(Suppl 1).
9. Hsiao-Ming Lu, J.F., *Proton therapy physics*, in *Series in medical physics and biomedical engineering*, H. Paganetti, Editor. 2012, CRC Press: Boca Raton, FL. p. 103-124.
10. Paganetti, H., *Proton therapy physics*, in *Series in medical physics and biomedical engineering*, H. Paganetti, Editor. 2012, CRC Press: Boca Raton, FL. p. 593-626.
11. Paganetti, H., et al., *Clinical implementation of full Monte Carlo dose calculation in proton beam therapy.* Phys Med Biol, 2008. **53**(17): p. 4825-53.
12. Paganetti, H., *Proton therapy physics*, in *Series in medical physics and biomedical engineering*, H. Paganetti, Editor. 2012, CRC Press: Boca Raton, FL. p. 265-304.
13. Benjamin Clasie, H.P., Hanne M. Kooy, *Proton therapy physics*, in *Series in medical physics and biomedical engineering*, H. Paganetti, Editor. 2012, CRC Press: Boca Raton, FL. p. 381-412.
14. Ferrari, A., et al., *FLUKA: A multi-particle transport code.* CERN-2005-10 (2005), INFN/TC_05/11, SLAC-R-773.
15. T.T. Böhlen, F.C., M.P.W. Chin, A. Fassò, A. Ferrari, P.G. Ortega, A. Mairani, P.R. Sala, G. Smirnov and V. Vlachoudis, *The FLUKA Code: Developments and Challenges for High Energy and Medical Applications.* Nuclear Data Sheets 120, 211-214 (2014).
16. Gottschalk, B., *Proton therapy physics*, in *Series in medical physics and biomedical engineering*, H. Paganetti, Editor. 2012, CRC Press: Boca Raton, FL. p. 19-60.
17. Ziegler, J.F., *Stopping of energetic light ions in elemental matter.* Journal of Applied Physics, 1999. **85**(3): p. 1249-1272.
18. Ytre-Hauge, K.S., *Measurements and Monte Carlo Simulations of Neutron Doses from Radiation Therapy with Photons, Protons and Carbon Ions*. 2013, University of Bergen.
19. Bortfeld, T. and W. Schlegel, *An analytical approximation of depth - dose distributions for therapeutic proton beams.* Physics in Medicine and Biology, 1996. **41**(8): p. 1331-1339.

20. ResearchGate, *Bragg peak of 62-MeV proton beam acquired in a water-tank with the Markus ionization chamber at CATANA facility.*
21. *The 2007 Recommendations of the International Commission on Radiological Protection. ICRP publication 103.* Ann ICRP, 2007. **37**(2-4): p. 1-332.
22. McMahon, S.J., *The linear quadratic model: usage, interpretation and challenges.* Phys Med Biol, 2018. **64**(1): p. 01TR01.
23. Yepes, P., et al., *Fixed- versus Variable-RBE Computations for Intensity Modulated Proton Therapy.* Adv Radiat Oncol, 2019. **4**(1): p. 156-167.
24. Guan, F., et al., *Analysis of the track- and dose-averaged LET and LET spectra in proton therapy using the geant4 Monte Carlo code.* Med Phys, 2015. **42**(11): p. 6234-47.
25. Giantsoudi, D., et al., *Can differences in linear energy transfer and thus relative biological effectiveness compromise the dosimetric advantage of intensity-modulated proton therapy as compared to passively scattered proton therapy?* Acta Oncol, 2018. **57**(9): p. 1259-1264.
26. McNamara, A.L., J. Schuemann, and H. Paganetti, *A phenomenological relative biological effectiveness (RBE) model for proton therapy based on all publishedin vitrocell survival data.* Physics in Medicine and Biology, 2015. **60**(21): p. 8399-8416.
27. Engelsman, M., *Proton therapy physics*, in *Series in medical physics and biomedical engineering*, H. Paganetti, Editor. 2012, CRC Press: Boca Raton, FL. p. 305-334.
28. Khan, F.M. and J.P. Gibbons, *Khan's the physics of radiation therapy*. Fifth edition. ed. 2014, Philadelphia, PA: Lippincott Williams & Wilkins/Wolters Kluwer. xi, 572 pages.
29. Zuofeng Li, R.S., Stella Flampouri, Daniel K. Yeung, *Proton therapy physics*, in *Series in medical physics and biomedical engineering*, H. Paganetti, Editor. 2012, CRC Press: Boca Raton, FL. p. 221-264.
30. Ainsley, C.G. and C.M. Yeager, *Practical considerations in the calibration of CT scanners for proton therapy.* J Appl Clin Med Phys, 2014. **15**(3): p. 4721.
31. Rath, A.K. and N. Sahoo, *Particle Radiotherapy*. 2016.
32. Lomax, A., *Proton therapy physics*, in *Series in medical physics and biomedical engineering*, H. Paganetti, Editor. 2012, CRC Press: Boca Raton, FL. p. 335-380.
33. Lee, S., Y.J. Cao, and C.Y. Kim, *Physical and Radiobiological Evaluation of Radiotherapy Treatment Plan*, in *Evolution of Ionizing Radiation Research*. 2015.
34. Schippers, M., *Proton therapy physics*, in *Series in medical physics and biomedical engineering*, H. Paganetti, Editor. 2012, CRC Press: Boca Raton, FL. p. 61-102.
35. Slopsema, R., *Proton therapy physics*, in *Series in medical physics and biomedical engineering*, H. Paganetti, Editor. 2012, CRC Press: Boca Raton, FL. p. 125-156.
36. Paganetti, H., et al., *Accurate Monte Carlo simulations for nozzle design, commissioning and quality assurance for a proton radiation therapy facility.* Med Phys, 2004. **31**(7): p. 2107-18.
37. Lu, H.M., et al., *Sensitivities in the production of spread-out Bragg peak dose distributions by passive scattering with beam current modulation.* Med Phys, 2007. **34**(10): p. 3844-53.
38. Flanz, J., *Proton therapy physics*, in *Series in medical physics and biomedical engineering*, H. Paganetti, Editor. 2012, CRC Press: Boca Raton, FL. p. 157-190.
39. National Electrical Manufacturers Association (NEMA), *Digital Imaging and Communications in Medicine (DICOM) Standard.* NEMA PS3 / ISO 12052.

40. Fjæra, L.F., *Development of a Monte Carlo Based Treatment Planning Verification Tool for Particle Therapy*. 2016, University of Bergen.
41. Agostinelli, S., et al., *Geant4—a simulation toolkit.* Nuclear Instruments and Methods in Physics Research Section A: Accelerators, Spectrometers, Detectors and Associated Equipment, 2003. **506**(3): p. 250-303.
42. Allison, J., et al., *Geant4 developments and applications.* IEEE Transactions on Nuclear Science, 2006. **53**(1): p. 270-278.
43. Perl, J., et al., *TOPAS: An innovative proton Monte Carlo platform for research and clinical applications.* Medical Physics, 2012. **39**(11): p. 6818-6837.
44. Vlachoudis, V., *FLAIR: A POWERFUL BUT USER FRIENDLY GRAPHICAL INTERFACE FOR FLUKA.* Proc. Int. Conf. on Mathematics, Computational Methods & Reactor Physics (M&C 2009), Saratoga Springs, New York, 2009.
45. Haas-Kogan, D., et al., *National Cancer Institute Workshop on Proton Therapy for Children: Considerations Regarding Brainstem Injury.* International Journal of Radiation Oncology*Biology*Physics, 2018. **101**(1): p. 152-168.
46. Kondziolka, D., et al., *The biology of radiosurgery and its clinical applications for brain tumors.* Neuro-Oncology, 2015. **17**(1): p. 29-44.
47. Fedorov, A., et al., *3D Slicer as an image computing platform for the Quantitative Imaging Network.* Magnetic Resonance Imaging, 2012. **30**(9): p. 1323-1341.
48. *3D Slicer*. Available from: http://www.slicer.org.
49. Kikinis, R., S.D. Pieper, and K.G. Vosburgh, *3D Slicer: A Platform for Subject-Specific Image Analysis, Visualization, and Clinical Support*, in *Intraoperative Imaging and Image-Guided Therapy*. 2014. p. 277-289.
50. Fjæra, L.F., et al., *Linear energy transfer distributions in the brainstem depending on tumour location in intensity-modulated proton therapy of paediatric cancer.* Acta Oncologica, 2017. **56**(6): p. 763-768.